Experimental and numerical investigations of shale gas permeability

By

Bao Jia

Submitted to the graduate degree program in Chemical & Petroleum Engineering and the Graduate Faculty of the University of Kansas in partial fulfillment of the requirements for the degree of Doctor of Philosophy

Chairperson: Reza Barati Ghahfarokhi

Jyun-Syung Tsau

G. Paul Willhite

Shapour Vossoughi

Xuemin Tu

Date Defended: November 29th, 2018

The dissertation committee for Bao Jia certifies that this is the approved
version of the following dissertation:

EXPERIMENTAL AND NUMERICAL INVESTIGATIONS OF SHALE GAS PERMEABILITY

Chairperson: Reza Barati Ghahfarokhi

Date Approved: November 29th, 2018

Abstract

Shale gas has become an essential source of energy supply in the United States and the world. It is important to analyze shale gas flow behavior and the associated production behavior from experimental and simulation perspectives. The specific objectives in this study are: (1) analyze shale gas flow behavior in the laboratory using pulse-decay experiments in both un-fractured and fractured cores, which will be accomplished in chapter 2 and chapter 3, respectively (2) propose a workflow to estimate shale gas permeability evolution taking into account multiple physics in the organic-rich matrix, which will be accomplished in chapter 4 (3) perform shale gas production simulations to justify the importance of these physics for shale gas production volume, which will be accomplished in chapter 5.

Pulse-decay experiments using adsorptive gas (nitrogen and carbon dioxide) and non-adsorptive gas relate complex relationships between gas apparent porosity and adsorption (in forms of Gibbs/excess and absolute), and gas apparent permeability and adsorption. Among the three types of gas, helium apparent permeability is the highest. The ratio between apparent porosity and intron porosity of tight porous media is the summation of unity and the density ratio between the adsorbed phase and the free gas phase. A coefficient different from the density ratio is involved in the flow governing equation of adsorptive gas, which is in accordance with the adsorption contribution to the gas apparent permeability. For nitrogen, the coefficient is positive; and for carbon dioxide, the coefficient can be positive or negative below and above the phase change pressure, respectively. Virtual experiment simulations by discrete-fracture modeling of the pulse-decay systems reveal that the effective permeability of the tight porous media with complex configurations during the transient flow process is different from that during the steady-state flow process. History matchings of pulse-decay experiments on one naturally fractured core under

different pore pressure and effective stress reveal that, matrix permeability is more sensitive to effective stress than matrix porosity, fracture porosity, and fracture permeability. It also implies that gas flow under a higher pressure is more likely in the homogeneous porous media as the matching errors show a decreasing trend with the pore pressure.

The workflow of estimating the shale gas permeability evolution curve reveals that, slip flow/pore diffusion and surface diffusion in shale matrix largely mitigate the permeability decrease by the effective stress during the gas depletion process. Shale gas production simulations considering dynamic properties of both the matrix and fractures indicates that, the natural fracture spacing is the most important to shale gas recovery. By contrast, slip flow and pore diffusion are less important. Surface diffusion might be essential to shale gas recovery depending on the surface diffusivity value: the 5-year forecast error of the gas recovery factor without considering surface diffusion is higher than 5% when the surface diffusivity is higher than 1E-6 m^2/s.

Acknowledgments

First of all, I would like to express my deepest gratitude to my advisors, Prof. Reza Barati and Dr. Jyun-Syung Tsau for their continuous and tremendous support during my Ph.D. years at Chemical & Petroleum Department of the University of Kansas (KU). Insightful discussions and valuable experimental help from them significantly helped me overcome many obstacles in my research. Their immense academic knowledge, critical reviews of technical papers, and daily kindness helped me walk through darkness and many pitfalls of my research.

I am very grateful to the financial support provided by Tertiary Oil Recovery Program (TORP), Chesapeake Energy Corporation, and Kansas Interdisciplinary Carbonates Consortium (KICC) during my Ph.D. years. I am also very grateful to the travel support to many technical conferences from TORP, Graduate Engineering Association (GEA), and Chemical & Petroleum Department. Special thank goes to our professional technician, Mr. Scott Ramskill, without his help our experiments could not have been finished successfully.

I would like to express my gratitude to Prof. G. Paul Willhite for being my committee member. I took Streamline Simulation course with him in Spring 2017. It is an honor for me to have taken one course from the National Academy of Engineering member. I am very grateful to his help offered to me that I will remember forever; besides, his daily humor attitude toward life influenced me a lot.

I would like to express my gratitude to Prof. Shapour Vossoughi for being my committee member. I took the excellent Enhanced Oil Recovery (EOR) course with him in Fall 2014. It is with great pleasure that I learned the basics of various kinds of EOR at KU renowned for tertiary oil recovery from Prof. Vossoughi with tremendous knowledge of EOR.

I would like to express my gratitude to Prof. Xuemin Tu from the Mathematics Department of KU for being my committee member. I took the excellent course of Applied Numerical Methods for Partial Differential Equations with her in Spring 2015. It is with great pleasure that I learned the foundation and programming of numerical methods that paved the way for my research from Prof. Xuemin Tu.

I would also like express my gratitude to Dr. Peltier, Mr. Mark Ballard, Ms. Mayumi Crider, and Dr. Stan McCool at TORP for offering me a lot of help during the past years. Last but not least, I enjoyed many moments with friends, classmates, colleagues, and professors on and outside of campus that I will cherish forever.

DEDICATED TO

My parents Fengliang Jia and Yueyun Yang

Table of Contents

List of Figures

List of Tables

Chapter 1: Introduction

1.1 Review of pulse-decay experiments

The pulse-decay experiment, or the transient gas transmission experiment, is a powerful method to measure low-permeability and ultra-low permeability in the laboratory. The pulse-decay experiment is unsteady-state, which is different from the conventional steady-state method. For the steady-state method, permeability is estimated based on Darcy's law after achieving pressure drop across the core sample. It fails to some extent for low-permeability scenarios because of several reasons (1) time to achieve pressure equilibrium is extremely long across the core sample because of the low flow rate (2) full scale of the pressure gauge of measuring pressure drop might be exceeded because of the low-permeability. The pulse-decay set-up is comprised of three major components: upstream reservoir, core sample, and downstream. The methodology of the pulse-decay experiment is to use pressure curves to interpret petrophysical properties. After providing a pressure pulse at the upstream stream, pressure declines at the upstream and builds up at the downstream. By applying simple Boyle's law, the porosity of the tested sample can be estimated after pressure equilibrium. Either analytical or numerical approach can estimate permeability of the sample.

Brace et al.[1] applied the pulse-decay experiment for the first time to measure granite permeability and came up with the first-version approximate analytical solution.

Governing equation of tight gas is expressed as:

$$\frac{\partial^2 p}{\partial l^2} = \frac{\mu c_g}{k}[(\frac{c_b - c_m}{c_g} + \phi(1 - \frac{c_m}{c_g})]\frac{\partial p}{\partial t} \tag{1-1}$$

where p is pressure l is the core direction, μ is gas viscosity, c_g is gas compressibility, k is permeability, c_b is bulk compressibility, c_m is mineral compressibility, ϕ is porosity, and t is time. If gas compressive storage is ignored, Eq. (1-1) becomes:

$$\frac{\partial^2 p}{\partial l^2} = 0 \tag{1-2}$$

The pressure at the upstream as a function of time is expressed as:

$$p_u(t) - p_f = [p_u(0) - p_d(0)]e^{-\sigma_1 t} \frac{v_d}{v_d + v_u} \tag{1-3}$$

where p_u is the upstream pressure, p_f is the equilibrium pressure, p_d is the downstream pressure, v_d is the volume of the downstream reservoir, v_u is the volume of the upstream reservoir. The coefficient $б_1$ is expressed as:

$$\sigma_1 = \frac{kA}{\mu c_g L}(\frac{1}{v_d} + \frac{1}{v_u}) \tag{1-4}$$

where A is the area of the cross-section, L is the core length.

Sutherland and Cave applied a different configuration of the pulse-decay experiment by making the downstream volume two orders' smaller than the upstream volume.[2] The approximate analytical solution they provided is:

$$p_u(t) - p_d(t) = [p_u(0) - p_d(0)]e^{-\sigma_2 t} \tag{1-5}$$

$б_2$ is expressed as:

$$\sigma_2 = \frac{kA}{\mu c L}\frac{1}{v_u} \tag{1-6}$$

Lin set up the numerical setting for the pulse-decay experiment. The initial pressure is $p_d(0)$ at the core and downstream, and $p_u(0)$ at the upstream.[3] The boundary conditions are: the mass flux leaves the upstream equals that enters the core sample, and the mass flux leaves the core sample equals that enters the downstream. The analytical solution by Lin is:

$$p_u(t) = [p_u(0) - p_d(0)]\exp(\frac{Ak\beta}{v_u c\mu} l + \frac{A^2k^2\beta}{v_u^2 c^2 \mu^2} t) erfc(\frac{\sqrt{\beta} l}{2\sqrt{t}} + \frac{Ak\sqrt{\beta} t}{v_u c\mu}) + p_d(0) \tag{1-7}$$

β is defined as:

$$\beta = \frac{\mu c_g}{k}[(\frac{c_b - c_m}{c_g} + \phi(1 - \frac{c_m}{c_g})] \tag{1-8}$$

Hsieh et al. used the concept of hydraulic head in the analytical solution:[4]

$$\frac{h(l,t)}{H} = \frac{1}{1+\kappa+\lambda} + 2\sum_{m=1}^{\infty} \frac{\exp(-\eta\chi_m^2)[\cos\chi_m\xi - (\lambda\chi_m/\kappa)\sin\chi_m\xi]}{(1+\kappa+\lambda-\lambda\chi_m^2/\kappa)\cos\chi_m - \chi_m(1+\lambda+2\lambda/\kappa)\sin\chi_m} \tag{1-9}$$

where $\kappa = S_s AL/S_u$, $\lambda = S_d/S_u$, $\eta = Kt/L^2 S_s$, $\xi = l/L$, $h(l,t)$ is the hydraulic head at core length of l and time t, and H is the increased pulse size at the upstream; S_d, S_u, and S_d are compressive storage for the downstream, upstream, and core sample, respectively. χ_m is the mth root of the transcendental equation:

$$\chi = \frac{(\chi+1)\chi}{\lambda\chi^2/\kappa - \kappa} \tag{1-10}$$

The analytical solution by Hsieh et al. is comprehensive, but it is difficult for engineering application because it involves an infinite number of roots of χ_m. Dicker and Smits applied dimensionless time to express dimensionless pressure in their analytical solution:[5]

$$t_D = \frac{kt}{c\mu\phi L^2} \tag{1-11}$$

$$\Delta p_D = \frac{p_u(t) - p_d(t)}{p_0(0) - p_0(0)} \tag{1-12}$$

$$\Delta p_D = 2\sum_{m=1}^{\infty} \exp(-t_D\theta_m^2) \frac{a(b^2+\theta_m^2) - (-1)^m b\sqrt{[(a^2+\theta_m^2)(b^2+\theta_m^2)}}{\theta_m^4 + \theta_m^2(a+a^2+b+b^2) + ab(a+b+ab)} \tag{1-13}$$

where a and b are volume ratios between pore volume and upstream reservoir, downstream reservoir, respectively.

$$a = \frac{v_b \phi}{v_a} \tag{1-14}$$

$$b = \frac{v_b \phi}{v_d} \tag{1-15}$$

where v_b is the bulk volume of the core sample.

θ_m is a series of roots for the transcendental equation:

$$\tan \theta_m = \frac{(a+b)\theta_m}{\theta_m^2 - ab} \tag{1-16}$$

Dicker and Smits provided an approximate analytical solution to simplify the comprehensive analytical solution:[5]

$$k = \frac{c_g \mu \phi L^2 \, | s |}{f(a,b)} \tag{1-17}$$

Eq. (1-17) is valid with high accuracy when *a* and *b* range from zero to unity. *f*(*a*,*b*) is a polynomial in terms of *a* and *b*:

$$f(a,b) = \theta_1^2 = (a+b+ab) - \frac{1}{3}(a+b+0.4132ab)^2 + 0.074(a+b+0.0578ab)^3 \tag{1-18}$$

Based on the analytical solution by Dicker and Smits, Cui et al. extended the solution for adsorptive gas. The governing equation for adsorptive gas is:[6]

$$\frac{\partial}{\partial l}\left(\frac{\rho_g k_a \partial p}{\mu \partial l}\right) = \frac{\partial(\phi_a \rho_g)}{\partial t} \tag{1-19}$$

where ρ_g is gas density, k_a is apparent permeability, ϕ_a is apparent porosity depending on both intrinsic porosity and adsorption:

$$\phi_a = \phi_{void} + (1-\phi_{void})\frac{\rho_{ad}}{\rho_g} \tag{1-20}$$

where ϕ_{void} is intrinsic porosity, ρ_{ad} is defined as the mass of adsorbed gas per unit volume of the rock.

If we take derivative of the right hand side of Eq. (1-19) with Eq. (1-20), Eq.(1-21) will be generated.

$$\frac{\partial(\phi_a\rho_g)}{\partial t}=\phi_a\frac{\partial\rho_g}{\partial t}+\rho_g\frac{\partial\phi_a}{\partial t}=\phi_a\frac{\partial\rho_g}{\partial t}+\rho_g(1-\phi_{void})\frac{\partial(\frac{\rho_{ad}}{\rho_g})}{\partial t} \tag{1-21}$$

Eq. (1-22) is derived by taking a further derivative of the right hand side of Eq. (1-21):

$$\begin{aligned}
&\phi_a\frac{\partial\rho_g}{\partial t}+\rho_g(1-\phi_{void})\frac{\partial(\frac{\rho_{ad}}{\rho_g})}{\partial t}\\
&=\phi_a\frac{\partial\rho_g}{\partial t}+\rho_g(1-\phi_{void})(\frac{\rho_g\frac{\partial\rho_{ad}}{\partial t}-\rho_{ad}\frac{\partial\rho_g}{\partial t}}{\rho_g^2})\\
&=[\phi_{void}+(1-\phi_{void})\frac{\rho_{ad}}{\rho_g}]\frac{\partial\rho_g}{\partial t}+(1-\phi_{void})(\frac{\partial\rho_{ad}}{\partial t}-\frac{\rho_{ad}}{\rho_g}\frac{\partial\rho_g}{\partial t})\\
&=\phi_{void}\frac{\partial\rho_g}{\partial t}+\frac{\partial\rho_{ad}}{\partial t}-\phi_{void}\frac{\partial\rho_{ad}}{\partial t}\\
&=\phi_{void}\frac{\partial\rho_g}{\partial t}+(1-\phi_{void})\frac{\partial\rho_{ad}}{\partial\rho_g}\frac{\partial\rho_g}{\partial t}\\
&=[\phi_{void}+(1-\phi_{void})\frac{\partial\rho_{ad}}{\partial\rho_g}]\frac{\partial\rho_g}{\partial t}
\end{aligned} \tag{1-22}$$

Eq. (1-22) is further expanded using the concept of gas compressibility:

$$\frac{\partial}{\partial l}\left(\frac{\rho_g k_a\partial p}{\mu\partial l}\right)=[\phi_{void}+(1-\phi_{void})\frac{\partial\rho_{ad}}{\partial\rho_g}]c_g\rho_g\frac{\partial p}{\partial t} \tag{1-23}$$

Based on Eq. (1-23), another concept of porosity, ϕ_{app}, is put forward:

$$\phi_{app}=\phi_{void}+(1-\phi_{void})\frac{\partial\rho_{ad}}{\partial\rho_g} \tag{1-24}$$

Therefore, to apply the permeability formula by Dicker and Smits, ϕ_{app} needs to be used and the associated *a* and *b* need to be modified:

$$k = \frac{c_g \mu \phi_{app} L^2 \, | s |}{f(a_{app}, b_{app})} \tag{1-25}$$

$$a_{app} = \frac{v_b \phi_{app}}{v_a} \tag{1-26}$$

$$b_{app} = \frac{v_b \phi_{app}}{v_d} \tag{1-27}$$

1.2 Regimes of shale gas flow behavior

Flow regimes in shales are defined based on the magnitude of *Kn*. Knudsen number is the ratio between gas mean free path and pore size:

$$Kn = \frac{l_m}{d} \tag{1-28}$$

where d is pore size, l_m is gas flow mean free path, which is defined as the distance traveled by the molecule during sequential collisions. l_m is estimated by:

$$l_m = \frac{k_B T}{\sqrt{2} Z \pi d_{mol}^2 p} \tag{1-29}$$

where Z is gas compressibility factor depending on gas type, temperature, and pressure; T is temperature; d_{mol} is molecule size; and k_B is the Boltzmann's constant.

It can be observed evidently from Eq. (1-28) and Eq. (1-29) that *Kn* number increases as pressure decreases and pore size decreases.

Flow with *Kn* smaller than 1E-3 is defined as continuum flow. In this regime, mean free path of gas molecules is negligible compared with the pore size.[7] The Hagen-Poiseuille and Darcy equations are valid because they are both developed based on the assumption of non-slip boundary condition, which means that molecule velocity at the pore wall equals zero.

Flow with *Kn* between 1E-3 and 1E-1 is defined as slip flow.[7] In this regime, non-slip boundary condition begins to fail because gas molecules begin to collide frequently with the pore wall, contributing to the total flow flux as slip flow. Mason and Malinauska applied the Dusty Gas Model to characterize slip flow. A first-order relationship is proposed for the ratio of k_a/k_∞.[8]

Flow with Kn between 1E-1 and 10 is defined as transition flow.[7] Karniadakis et al. applied Monte Carlo simulations to characterize the complex transition flow.[9] An empirical relationship is proposed for the relationship between the mass flux and Knudsen number, gas density and pressure gradient, which includes the inverse circular trigonometric function. Sakhaee-Pour and Bryant simplified the relationship that they expressed the ratio between gas permeability and intrinsic permeability as a second-order function of Knudsen number.[10]

Flow with Kn larger than 10 is defined as free molecular flow.[7] In this regime, mass flux equals to the multiplication between Knudsen diffusivity and density gradient.

Jia et al. investigated flow regimes in shale reservoirs with a wide range of temperature, pore size, and temperature, concluding that gas flow in most shale reservoirs lie in the regimes of slip flow and transition flow.[11]

1.3 Review of different models of shale gas flow

Klinkenberg measured gas permeability in the porous media and found that gas permeability is a function of pressure, indicating that permeability is not an inherent property of the porous media that it depends on flow conditions.[12] Therefore the apparent permeability, k_a, should be distinguished from the inherent permeability, k_∞. The inherent permeability is equivalent to the liquid permeability or gas permeability under infinite high pressure. Klinkenberg came up with the first-order relationship between the k_a and k_∞ as follows:[12]

$$k_a = k_\infty (1 + \frac{b_{slip}}{p}) \tag{1-30}$$

where b_{slip} is slippage factor.

Heid et al. expressed the slippage factor as a function of intrinsic permeability by collecting experimental data from 175 core samples:[13]

$$b_{slip} = 11.419(k_\infty)^{-0.39} \tag{1-31}$$

Jones and Owens performed experiments in low-permeability sands, achieving a similar formula as Heid et al. but with different coefficeints:[14]

$$b_{slip} = 12.639(k_\infty)^{-0.33} \tag{1-32}$$

Sampath and Keighin included porosity in the gas slippage factor as:[15]

$$b_{slip} = 13.851(\frac{k_\infty}{\phi})^{-0.53} \tag{1-33}$$

After Sampath and Keighin, Florence et al. included another parameter depending on gas type in the equation:[16]

$$b_{slip} = \beta_1(\frac{k_\infty}{\phi})^{-0.5} \tag{1-34}$$

Civan expressed b_{slip} after including more pareamters using data of Florence et al.:[17]

$$b_{slip} = \frac{2.79\times10^3\mu}{\sqrt{M}} k_\infty^{-0.5}\phi^{0.5} \tag{1-35}$$

where M is molecular weight, for nitrogen, b_{slip} is:

$$b_{slip} = 0.0094(\frac{k_\infty}{\phi})^{-0.5} \tag{1-36}$$

In addition to the flow models based on the Klinkerberg equation, many researchers have come up with analytical equations to characterize gas apparent permeability in shales.

Beskok and Karniadakis developed a model for micro and nanochannels incorporating all the flow regimes,[18] which is validated against molecular dynamics simulations and experiments. The model is described as follows:

$$Q=-\frac{\pi h^4}{8\mu}\frac{dp}{dl}(1+\alpha Kn)(1+\frac{4Kn}{1-cKn}) \tag{1-37}$$

where Q is volume flux, h is channel height, μ is gas viscosity. c is a fitting parameter that should be determined from experimental data, (1+ αKn) is termed as rarefaction factor that is zero for continuum flow and slip flow and reaches an asymptotic value for free molecular flow as molecular interactions diminish.

Florence et al. proposed a microflow model by expressing the ratio between gas permeability and intrinsic permeability as a function of Kn:[16]

$$\frac{k_a}{k_\infty}=[(1+\gamma(Kn)Kn][1+\frac{4Kn}{1+Kn}] \tag{1-38}$$

where $\gamma(Kn)$ is expressed as:

$$\gamma(Kn)=\frac{128}{15\pi^2}\tan^{-1}(4Kn^{0.4}) \tag{1-39}$$

Civan simplified $\gamma(Kn)$ using a simplified power-law relationship as below:[17]

$$\frac{64}{15\pi\gamma(Kn)}-1=\frac{A_1}{Kn^{B_1}} \tag{1-40}$$

Based on the data of Loyalka and Hamoodi,[19] A_1 and B_1 are estimated as 0.1780 and 0.4348, respectively; based on the data of Tison and Tilford,[20] A_1 and B_1 are estimated as 0.199 and 0.365, respectively.

Javadpour expressed the total mass flux in the nanopore as follows:[21]

$$J=J_a+J_D \tag{1-41}$$

where J_a is advective flow component and J_D is Knudsen diffusion component.

J_a is expressed as:

$$J_a=-\frac{r^2}{8\mu}\frac{\rho}{L}\Delta p \tag{1-42}$$

where r is pore radius, L is length, ρ is gas density which is an average between the inlet and outlet density.

Knudsen diffusion component is expressed as:[22]

$$J_D = \frac{MD_K}{10^3 RT} \nabla p \tag{1-43}$$

where R is universal gas constant.

The ratio between gas apparent permeability and intrinsic permeability is expressed as:

$$\frac{k_a}{k_\infty} = \frac{2\mu M}{3\times 10^3 RT\rho^2} \left(\frac{8RT}{\pi M}\right)^{0.5} \frac{8}{r} + \left[1 + \left(\frac{8RT}{\pi M}\right)^{0.5} \frac{\mu}{pr} \left(\frac{2}{\alpha} - 1\right)\right] \frac{1}{\rho} \tag{1-44}$$

A correction factor, F, based on Eq. (1-42), is defined to correct for the slip boundary condition on the pore wall:

$$F = 1 + \left(\frac{8\pi RT}{M}\right)^{0.5} \frac{\mu}{pr} \left(\frac{2}{\alpha} - 1\right) \tag{1-45}$$

Surface diffusion is also a possible flow mechanism in organic-rich shale. Adsorbed gas molecules move along the pore surface as a “hopping” mechanism. A number of studies have believed surface diffusion is important.[23-29] However, surface diffusivity in shales have seldom been reported by solid experimental studies. To the best of our knowledge, till now, only one study by Akkutlu and Fathi reported experiment based surface diffusivity values.[30] They applied a non-linear regression algorithm to history match upstream pressures in pulse-decay experiments. Several parameters are set to be tuned in the algorithm, including permeability, organic matter volume ratio, free gas diffusivity, adsorption kinetic parameters, and surface diffusivity. Three core samples were tested by history matching ten pressure curves. Ranges of surface diffusivity they estimated are 5.1E-8 m^2/s to 1.0E-7 m^2/s, 1.1E-6 m^2/s to 8.8E-4 m^2/s, and 1.1E-7 m^2/s to 4.6E-7 m^2/s for Sample 1, Sample 2, and Sample 3, respectively.

1.4 Objectives and structure of the dissertation

Though there are many studies regarding pulse-decay experiments, a comprehensive experiment data pool is relatively scarce in the literature. Besides, most studies separately focus on adsorption or flow behavior in shales, how to relate them in the experiments remain poorly understood. Therefore, the first objective is as follows that will be accomplished in chapter 2.

Perform pulse-decay experiments for different types of gas from low pressure to high pressure. Explore the complex relationships among adsorption, porosity, and permeability behaviors in shales.

Investigations of petrophysical properties in the fractured cores using the transient method are still scarce, and fluid behavior has not been studied thoroughly over a wide range of pressure and effective stress. Therefore, the second objective is listed as follows that will be accomplished in chapter 3.

Perform pulse-decay experiments on one fractured core. History match pressure curves at both the upstream and the downstream after constructing flow models for the system. Explore relationships between matrix and fracture properties as functions of pore pressure and effective stress.

There have been numerous studies trying to figure out flow behavior in organic-rich shales by various methods. However, limited studies are focusing on providing an apparent permeability curves taking into account all possible physics that will occur during the lifetime of a shale gas well. Therefore, the third objective is listed as follows that will be accomplished in chapter 4.

Collect experimental data in the literature required to obtain a permeability evolution curve in a specified shale play. Explore the permeability curve including multiple physics of the effective stress, slip flow and pore diffusion, adsorption/desorption, and surface diffusion.

Compared with digging into how fluids flow in shales, it is of more importance to evaluate how these flow behavior not present in conventional reservoirs affect production behavior in unconventional reservoirs by performing shale gas production simulations. Therefore, the fourth objective is listed as follows that will be accomplished in chapter 5.

Perform shale gas production simulations to justify the importance of multiple physics in the matrix. Both dynamic properties and the matrix and fractures will be included in the simulation, and fractures will be distinguished in forms of propped fractures in the stimulated reservoir volume (SRV) and unpropped fractures outside of SRV.

Note: All the formulas and equations in the introduction chapter are from previous publications and no detailed calculations are involved. For further applications of these formulas and equations in terms of units and conversion factors, please consult with the original publications.

1.5 Nomenclature

a	Volume ratio between pore volume and the upstream reservoir volume
A	Area of the cross-section of the core
A_1	Coefficient in Eq. (1-40)
a_{app}	Modified a in Eq. (1-26)
b	Volume ratio between pore volume and the downstream reservoir volume
B_1	Coefficient in Eq. (1-40)
b_{app}	Modified b in Eq. (1-27)
b_{slip}	Slip factor
c	Parameter in Eq. (1-37)

c_b	Bulk compressibility
c_g	Gas compressibility
c_m	Matrix compressibility
D	Downstream reservoir
d	Pore size
D_a	Density ratio between the adsorbate and free gas
D_K	Knudsen diffusivity
d_{mol}	Gas molecule size
h	Hydraulic head in Eq. 1-9
h	Channel height in Eq. 1-37
H	Hydraulic head increase at the upstream
J	Total mass flux
J_a	Advective mass flux
J_D	Darcy mass flux
k	Permeability
k_∞	Intrinsic permeability
k_a	Gas apparent permeability
K_a	Partitioning coefficient
Kn	Knudsen number
l	Flow direction
L	Core length
l_m	Gas mean free path
M	Molecular weight

p	Pressure
p_d	Downstream reservoir pressure
p_D	Dimensionless pressure
p_u	Upstream reservoir pressure, psi
Q	Volume flux
r	Pore radius
R	Universal gas constant
S_d	Compressive storage at the downstream
S_u	Compressive storage at the upstream
t	Time
T	Temperature
t_D	Dimensionless time
v_b	Bulk volume of the core
v_d	Downstream reservoir volume
v_u	First upstream reservoir volume
Z	Compressibility factor, dimensionless
α	Coefficient in Eq. (1-44)
β	Coefficient in Eq. (1-7)
β_1	Coefficient in Eq. (1-34)
η	Coefficient in Eq. (1-9)
θ	Root in Eq. (1-13)
κ	Coefficient in Eq. (1-9)
λ	Coefficient in Eq. (1-9)

μ	Viscosity
ξ	Coefficient in Eq. (1-9)
ρ	Density in Eq. (1-42)
ρ_{ad}	Mass of adsorbed gas per unit volume of the rock
ρ_g	Density of free gas
ϕ	Porosity
ϕa	Apparent porosity
ϕ_{app}	Apparent porosity in the transport governing equation
ϕ_{void}	Intrinsic porosity
χ	Root in Eq. (1-10)
$б_1$	Coefficient in Eq. (1-3)
$б_2$	Coefficient in Eq. (1-5)

Chapter 2: Pulse-decay experiment with three types of gas

This chapter is a copy of the published paper "Different flow behaviors of low-pressure and high-pressure carbon dioxide in shales" in *SPE Journal* (August 2018, 23 (4): 1452-1468). with format change after purchasing the copyright through Rightslink. SPE holds the copyright for this chapter. This chapter should be downloaded for only personal use, and further use of the materials in this chapter should purchase the copyright from SPE.

2.1 Summary

Understanding carbon dioxide storage capacity and flow behavior in shale reservoirs is important for both carbon dioxide related improved oil recovery (IOR)/enhanced gas recovery (EGR) performance and carbon sequestration. However, the literature lacks sufficient experimental data and a deep understanding of carbon dioxide permeability and storage capacity in shale reservoirs under a wide range of pressure. In this study, we aimed to fill this gap by investigating and comparing carbon dioxide transport mechanisms in shale reservoirs under low-pressure and high-pressure conditions. Nearly forty pressure pulse transmission tests were performed with carbon dioxide, helium and nitrogen for comparison. Tests were conducted under constant effective stress with multistage increased pore pressures (0~2,000 psi) and constant temperature. Gas (carbon dioxide and nitrogen) adsorption capacity was measured in terms of both Gibbs and absolute adsorption. Afterward, the gas apparent permeability was calculated incorporating various flow mechanisms before the adsorption-free permeability was estimated to evaluate the adsorption contribution to the gas transport efficiency. The results indicate that helium permeability is the highest among the three types of gas, and the characteristic of CO_2 petrophysical properties differs from the other two types of gas in shale reservoirs. CO_2 apparent porosity and apparent permeability both decline sharply across the phase change region. The

adsorbed phase significantly increases the apparent porosity which is directly measured from the pulse-decay experiment; it contributes positively to the low-pressure CO_2 permeability but negatively to the high-pressure CO_2 permeability.

2.2 Introduction

CO_2 injection has been suggested as a feasible method for IOR in tight oil or shale oil reservoirs by conventional flooding or huff-n-puff process.[31-34] CO_2 has stronger adsorption capacity than CH_4 in shale reservoirs, making it promising to recover CH_4 through competitive adsorption in shale gas reservoirs.[35, 36] In addition, injecting CO_2 into shales reduces greenhouse emissions.[37] Therefore, it is crucial to have a deep understanding of the relationship between CO_2 adsorption and its flow process in the porous media to accurately model IOR and EGR processes. Many researchers have explored the impact of adsorption on oil/gas storage capacity and flow behavior, separately.[38-40] However, simultaneous investigation of the relationship between the adsorbate and porosity/permeability with detailed experimental data over a wide range of pressure is relatively scarce in the literature; and we aimed to fill this gap by performing a series of gas pressure transient transmission (pulse-decay) tests for different types of gas from very low pressure to the pressure above the CO_2 critical pressure.

Pressure pulse decay experiments have frequently been used to investigate petrophysical properties of tight cores since Brace et al. firstly introduced this method to measure granite permeability.[1] Many scholars improved this approach theoretically and experimentally. For instance, Lin put forward the basic numerical model for the process of the pressure transmission test.[3] Hsieh et al. derived the complete and restrictive analytical solution for the numerical model. Dicker and Smits conducted parametric analysis for the variables involved in the experiment and approximated the complete analytical solution with a fast and simple permeability determination method with acceptable accuracy.[5] Jones provided valuable recommendations for the pulse-decay system design.[41] Cui et al. extended the flowing fluid from non-adsorptive gas to adsorptive gas, and provided a modified model for adsorptive gas permeability estimation,[6] which is adopted in this study to explore the fractional contribution of adsorption to gas permeability. Ghanizadeh et al. studied impacts of effective stress, anisotropy and moisture effect on fluid transport process and storage capacity by the pulse-decay method in comparison with other methods: the profile (probe) and crushed power (GRI) methods.[42-45] Jia et al. investigated effects of microcrack and core heterogeneity numerically and experimentally on the pressure responses in a typical pulse-decay experiment.[46]

However, the interactions between adsorption and the flow behavior of tight porous media is not clear to date because that (1) free gas and the adsorbed gas with different properties both exist in nanopores (<2nm) and mesopores (2 nm–50 nm) that they affect the apparent porosity and apparent permeability differently; (2) two concepts of adsorption: Gibbs (excess) and absolute adsorption are frequently applied for the measurement of the adsorbed phase, however, how to relate them with the complex flow behavior of the tight porous media from a macroscopic view is rarely discussed in the literature; (3) adsorption has complex impacts influencing gas permeability. The objectives of this study are: (1) obtain extensive experimental data for gas apparent porosity, adsorption and apparent permeability using three types of gas: helium, nitrogen and carbon dioxide; (2) relate the adsorbed phase to apparent porosity and apparent permeability for the adsorptive gas by an analytical approach from a macroscopic view.

2.3 Background

For clarity, it is stated here that three categories of permeability are covered in this work: intrinsic permeability of the porous media k_∞, gas apparent permeability k_a and gas apparent permeability without taking adsorption into account $k_{ads\text{-}free}$. Eq. (2-1) by Javadpour gives a clear illustration for the relationship between $k_{ads\text{-}free}$ and k_∞ assuming the flowing gas is non-adsorptive:[21]

$$\frac{k_{ads-free}}{k_\infty}=1+(\frac{2}{\alpha}-1)\frac{\mu}{p_{avg}r}(\frac{8\pi RT}{M})^{0.5}+\frac{16\mu}{3\times10^3 p_{avg}r}(\frac{8RT}{\pi M})^{0.5} \tag{2-1}$$

$$k_{ads-free}=k_\infty\times f(Kn) \tag{2-2}$$

where α refers to the gas type and pressure dependent tangential factor (dimensionless), which should be determined experimentally, p_{avg} is averaged pressure (Pa), r is pore size (m), R is the universal gas constant (8.314 J/mol·K), T is temperature (K), M is molecular weight (kg/mol) and μ is viscosity (Pa·s). On the right-hand side (RHS), the second term describes the contribution of slip flow to the permeability, and the third term describes the contribution of diffusion to the permeability. It is observed that the ratio of apparent permeability over intrinsic permeability $f(Kn)$ is greater than one. As the pore size and pressure increase, the ratio would be close to one, indicating that in conventional reservoirs (with large pore size) and under high pressure, the apparent permeability and intrinsic permeability will be close to each other. The direct measured permeability value from the laboratory, by either steady-state or unsteady-state approach is an apparent value that depends on flowing conditions. In contrast, the intrinsic permeability k_∞ is an inherent property of the porous media independent of flowing conditions. If the flowing fluid is adsorptive gas, the flow behavior becomes more complex because surface diffusion is involved. To date, many complicated flow models have been built attempted to incorporate slip flow, pore diffusion (Knudsen diffusion and Fickian diffusion) and surface diffusion all together in the analytical model.[47-48] Lattice Boltzmann (LB) method combined with Digital Rock Analysis (DCA) is frequently used to simulate gas flow process in different flow regimes including the physics mentioned above.[49-51] Differently, the modified apparent permeability estimation model for adsorptive gas put forward by Cui et al. is based on the pulse-decay set-up.[6] It can be conveniently applied to distinguish $k_{ads\text{-}free}$ and k_a from a macroscopic view, and therefore, the net contribution of adsorption to the gas flow capacity can be estimated as the ratio of $(k_a - k_{ads\text{-}free})/k_{ads\text{-}free}$.

2.4 Experimental apparatus and procedures

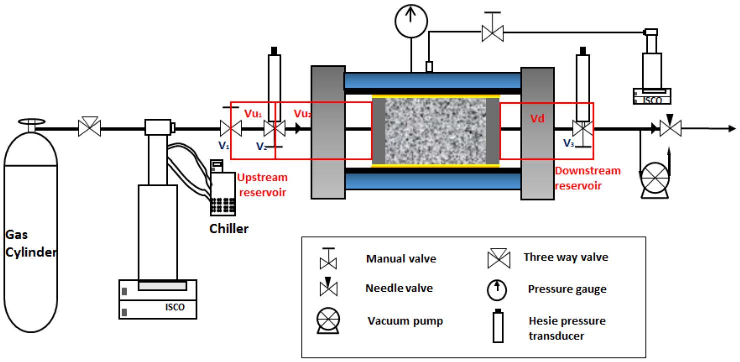

Figure 2-1 Schematic of the pulse-decay set-up.

Figure 2-1 describes the schematic of the pulse-decay apparatus. Upstream and downstream reservoirs are installed before the core inlet and after the core outlet, respectively. The upstream reservoir is composed of two parts: U_1 is the part between valves V_1 and V_2, and U_2 is the part between V_2 and the core inlet. Reservoirs are composed of the dead volumes in the tubing, valves and Heise pressure transducers. Prior to the core test, Boyle's law is applied to estimate the reservoir volume. Table 1-1 lists the measured reservoir volumes with deviations.

Table 2-1 Volumes of reservoirs with deviation from five measurements.

Reservoir	U_1 (first upstream reservoir)	U_2 (second upstream reservoir)	D (downstream reservoir)
Mean value, cm^3	3.147	0.611	3.964
Deviation, cm^3	0.066	0.005	0.025

Before each test, measures are taken to ensure gas purity in the system. The vacuum pump is used to evacuate air with V_3 open and V_1, V_2 closed. Pressure in the Heise pressure transducer at the upstream reaches the vacuuming pressure after several hours indicating the whole sample has been efficiently vacuumed. The vacuuming process continued for three days to further ensure the vacuum state of the pore space in the core. Measures are also taken to keep the purity of gas between the ISCO pump and V_1. Relatively low pressure (20-30 psi) gas is introduced from the gas cylinder to the ISCO pump and U_1 with V_1 open. Then the three-way valve is opened to release gas into the atmosphere. This practice repeats several times.

One should notice that it is difficult to prevent gas leaking in the pulse-decay system. The side surface of core plug is firstly coated with ten layers of Teflon tape, and then wrapped with heat shrink tube to prevent gas leakage into the confining fluid through the core sleeve. Nevertheless, based on our experience, the leaking problem can be relieved but cannot be completely avoided, especially for high-pressure test. Two possible leakage sources are suggested: one is from the side surface of the core to the confining fluid through the core holder sleeve, and the other is the gap between end surfaces of the core and the end caps. Perfect smooth and paralleled end surfaces of the core are able to fully eliminate the second leakage source, but even if the gap is of nanometer scale, gas still has a chance to flow out of the gap, considering the small pore size of shales. To obtain more accurate porosity values, measures adopted from Alnoaimi et al. are taken to compensate for the potential gas leakage and prior to that,[52] Teflon-made dummy core was applied in the place of the rock core to make sure no detectable gas leakage was observed. After gas equilibrium in each test, the decrease of pore pressure over time is recorded, and the decreasing rate is multiplied with the pressure pulse-decay time. The calculated result is added onto the final equilibrium pressure for the porosity calculation. If the pressure compensation is not applied, the estimated porosity will be slightly larger than the actual value because the equilibrium pressure is lower. In contrast, the estimated permeability is negligibly affected, the reason will be elaborated in the latter part of discussing permeability.

During the experiment, a pressure pulse needs to be introduced from the ISCO pump to U_1 with V_1 open and V_2 closed. The size of the pressure pulse is defined as the ratio between the added pressure and the original pore pressure. Then V_2 is opened to obtain the pressure decline curve in the upstream reservoir and pressure build-up curve in the downstream reservoir. Apparent porosity is estimated using Boyle's law; apparent permeability can be estimated by using either a numerical method or an analytical method. In this work, the analytical solution put forward by Dicker and Smits is applied and the modified solution for adsorptive gas by Cui et al. is applied.[5, 6]

The pore pressure of investigation in this study is increased continuously from very low pressure to near 2,000 psi at a constant effective stress of 2,000 psi to keep the bulk volume constant through the process. A large pressure pulse size and a small pressure pulse size (approximately 10%) are applied alternately during the process. Large pressure pulse is used to speedily increase the pore pressure especially during the low-pressure range. The difference between a large pulse size and small pulse size becomes less as the system pressure is elevated. Figure 1-2 shows pulse sizes for all the data points applied for the three types of gas through the process.

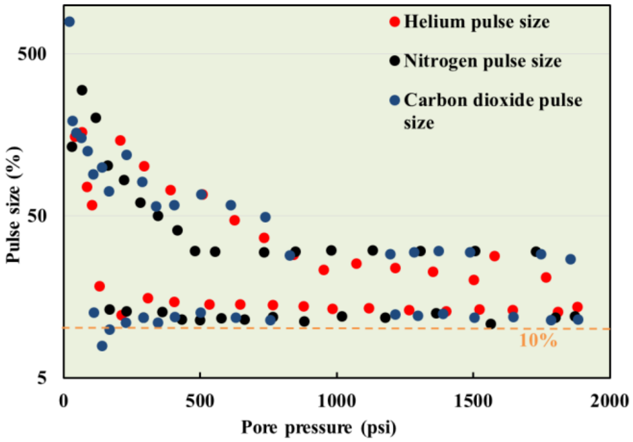

Figure 2-2 Pulse size (%) for the pulse-decay test of the three types of gas.

The CO_2 data points are discontinued in the pressure region of phase change. Pressure range of CO_2 investigated in this study is shown in the CO_2 phase envelope of Figure 2-3. In the process of increasing the pore pressure, it is found not possible to perform the pulse-decay process during the region of phase change. Figure 2-4 illustrates the pressure profiles at the upstream and downstream together with the CO_2 pressure-dependent density. CO_2 is injected from the upstream in the manner of constant pressure. Numerous hours are required for this process as the pressure stagnated near the critical pressure for a long time. Therefore, porosity and permeability data are not available in the phase change region.

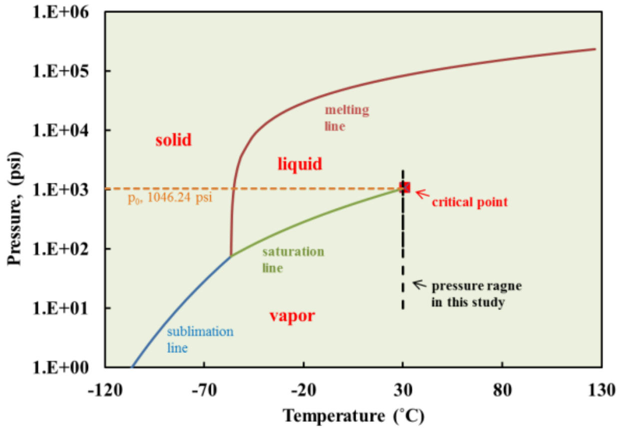

Figure 2-3 Pressure range of CO_2 investigated in this study (black dotted line).

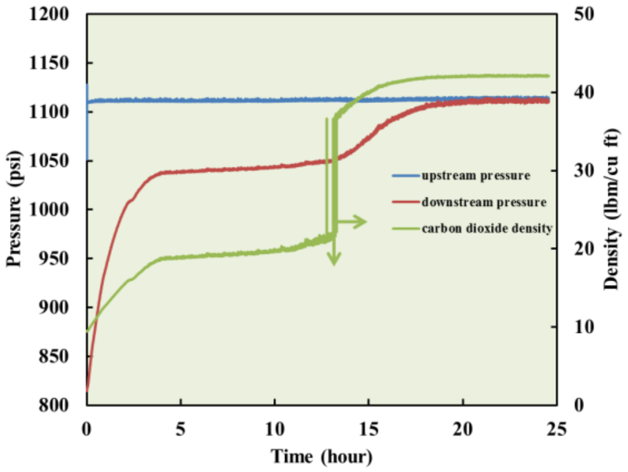

Figure 2-4 Pressure profiles of upstream and downstream during the period of increasing pore pressure across the phase change region.

2.5 Core properties

The shale core used in this study is from Garden Gulch member of Green River formation, Colorado. The details of the core are described in Table 2-2. The mineralogy information is provided in Figure 2-5. A 40-minute X-Ray Diffraction (XRD) scan was applied on the shale powder (experiment performed at New Mexico Bureau of Geology). Based on the scan result, this sample contains around 44% quartz, 27% illite that Muscovite is used as a proxy, 17% albite, variable amounts of chamosite & kaolinite (total 8%), and 3% dolomite. Although XRD is not an efficient way to determine TOC in a rock sample, an amorphous hump will form in the spectra if the amount of organic matter is high. The spectra produced from the sample shows no evidence of measurable amorphous material (Figure 2-5), therefore, TOC content in this sample is negligible. Generally speaking, the more the organic matter and the more mature the organic matter, a larger surface area is expected, which results in larger adsorption capacity.[51, 53]

Table 2-2 Basic information of the core sample.

Age	Eocene
Formation	Garden Gulch Member of Green River Formation

Thickness, ft	190-700
Diameter, inch	1.48
Length, inch	1.46
Color	Gray to brown

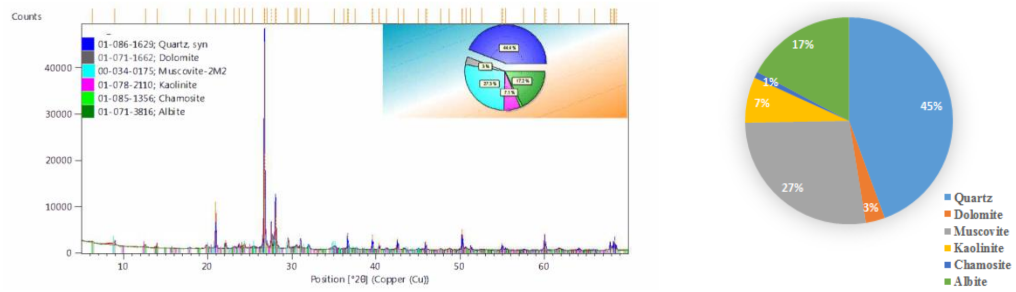

Figure 2-5 Result of the spectrum of the 40-minute XRD scan(left) and mineralogy (right) of the shale powder.

Figure 2-6 shows the pore size distribution (PSD) of the sample in the form of powder (small size) and grain (big size) interpreted from the adsorption and desorption profile of low-temperature nitrogen adsorption profile using Quantachrome®ASiQwin™ (experiment performed at Center for Environmentally Beneficial Catalysis (CEBC) at the University of Kansas). Small difference is observed between two distributions that the one in the form of grain should more represent the original core because the grain was not crushed as much as the powder. Pore size ranges from 3 nm and 242 nm with two humps peaking at 4 nm and 30 nm, respectively.

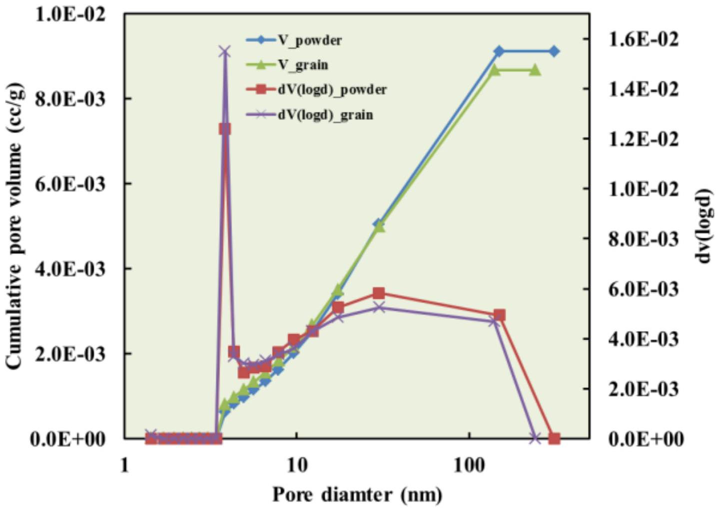

Figure 2-6 Pore size distribution of the sample in the form of powder and grain.

2.6 Apparent porosity

Eq. (2-3) and Eq. (2-4) are used to estimate gas apparent porosity based on three pressure values and the reservoir volumes.

$$\frac{p_u V_{u1}}{Z_u} + \frac{p_d (V_{u2} + V_d + V_a)}{Z_d} = \frac{p_e (V_{u1} + V_{u2} + V_d + V_a)}{Z_e} \tag{2-3}$$

$$\phi_a = \frac{V_a}{V_b} \tag{2-4}$$

where p_u, p_d and p_e are initial upstream pressure, initial downstream pressure and equilibrium pressure, respectively. V_{u1}, V_{u2} and V_d are volumes of U_1, U_2, and D, respectively. Z_u, Z_d and Z_e are compressibility factors under pressure of p_u, p_d and p_e, respectively. V_a is the estimated gas apparent pore volume, and V_b is the core bulk volume. Gas apparent porosity ϕ_a is defined as the ratio of gas apparent pore volume over the bulk volume of the core.

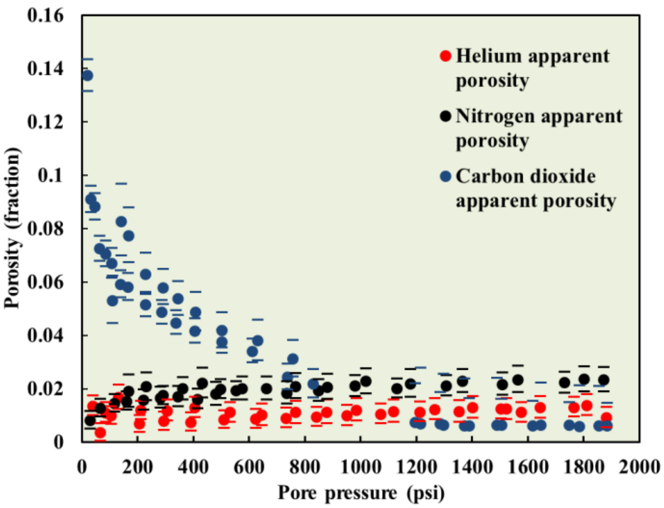

Figure 2-7 Helium, nitrogen and carbon dioxide apparent porosity as functions of pore pressure. The error bars are estimated based on the lower and upper bounds of the seven parameters involved in the porosity calculation formula Eq. (2-3).

Figure 2-7 shows the apparent porosity of helium, nitrogen and carbon dioxide. Because of the pressure fluctuation, temperature fluctuation, and reservoir volume uncertainty, it is necessary to assess the result uncertainty. Seven parameters are analyzed (Table 2-3) to obtain upper and lower bounds of the porosity as illustrated in Figure 2-7, 128 (2^7) calculations are performed using upper and lower bounds of the seven parameters. The minimum and maximum among the 128 results are estimated as the lower and upper bounds, respectively. CO_2 apparent porosity has larger deviation than the other two types of gas due to its larger pressure fluctuations, particularly for the high-pressure tests.

Subsequently, sensitivity analysis is performed to evaluate the significance of each parameter in the porosity calculation formula to the uncertainty of porosity. The Global Sensitivity Analysis Toolbox (GSAT) is applied in this study. Mean value and range of the parameters are used as the input for the test.[54] Compressibility factor which is gas type, pressure and temperature dependent is imported from the REFPROP program.[55] Three sensitivity indexes can be obtained from the output: S_{fast} is based on the Fourier Amplitude Sensitivity Test (FAST), and S and S_{tot} are based on Sobol'sensitivity. Sensitivity index ranges between 0 and 1, a large index indicates a large impact on the output.

Table 2-3 and Table 2-4 show the mean value, upper and lower bounds of the seven parameters for the porosity calculation under the equilibrium pressure of 627.77 psi for helium and 1,855.29 psi for carbon dioxide, respectively. Table 2-5 and Table 2-6 show the corresponding uncertainty analysis result. We can see the sensitivity index of V_{u1} is close to one and negligible of the other parameters, indicating that the accuracy of V_{u1} plays the most significant role in the porosity calculation formula. For the CO_2 test under the high pressure of 1,855.29 psi, the significance of V_d also increases, but is still one order magnitude smaller than that of V_{u1}. Fluctuation of the temperature is too small to affect to the porosity results. Even though larger pressure fluctuation is observed for high-pressure CO_2, the impact of it is still insignificant. The sensitivity analysis reveals that it is crucial to ensure the accuracy of the first upstream volume to obtain reliable porosity in our experiment. Therefore, if the deviation of the first upstream reservoir volume becomes smaller, it can be anticipated that the significance of V_{u1} in porosity estimation will be reduced and a more accurate result can be obtained. For different in-house pulse-decay systems, the sensitivity analysis result might be different; and it serves to evaluate proportions of different sources of uncertainty in the input and improve the output porosity accuracy.

Table 2-3 Mean, deviation and upper/lower bounds of seven parameters in the equation for porosity calculation (gas is helium and equilibrium pressure is 627.77 psi).

	Temperature, ˚C	Upstream pressure, psi	Downstream pressure, psi	Equilibrium pressure, psi	V_{u1}, cm^3	V_{u2}, cm^3	V_d, cm^3
Mean	30.25	779.97	530.22	627.77	3.14	0.62	3.96
Deviation	0.15	0.1	0.05	0.1	0.066	0.005	0.025
Upper bound	30.4	780.07	530.27	627.87	3.206	0.625	3.985
Lower bound	30.1	779.87	530.17	627.67	3.074	0.615	3.935

Table 2-4 Mean, deviation and upper/lower bounds of seven parameters in the equation for porosity calculation (gas is carbon dioxide and equilibrium pressure is 1,855.29 psi).

	Temperature, ˚C	Upstream pressure, psi	Downstream pressure, psi	Equilibrium pressure, psi	V_{u1}, cm^3	V_{u2}, cm^3	V_d, cm^3
Mean	30.2	1992.00	1,786.00	1,885.29	3.14	0.62	3.96
Deviation	0.15	2.8	2.0	2.0	0.066	0.005	0.025
Upper bound	30.35	1994.00	1,788.00	1,887.29	3.206	0.625	3.985
Lower bound	30.05	1989.20	1,784.00	1,883.29	3.074	0.615	3.935

Table 2-5 Sensitivity analysis result of parameters for porosity calculation (gas is helium and equilibrium pressure is 627.77 psi).

	Temperature	Upstream pressure	Downstream pressure	Equilibrium pressure	V_{u1}	V_{u2}	V_d
S_{fast}	2.00E-06	4.19E-04	2.99E-04	3.05E-03	9.67E-01	9.60E-04	2.41E-02
S	2.07E-06	4.31E-04	3.02E-04	2.90E-03	9.67E-01	9.85E-04	2.39E-02
S_{tot}	-2.00E-05	4.10E-04	2.82E-04	2.88E-03	9.67E-01	9.64E-04	2.39E-02

Table 2-6 Sensitivity analysis result of parameters for porosity calculation (gas is carbon dioxide and equilibrium pressure is 1855.29 psi).

	Temperature	Upstream pressure	Downstream pressure	Equilibrium pressure	V_{u1}	V_{u2}	V_d
S_{fast}	7.42E-06	6.79E-02	2.31E-01	4.40E-01	2.23E-01	3.59E-04	3.52E-02
S	-1.01E-04	6.75E-02	2.30E-01	4.41E-01	2.25E-01	2.55E-04	3.54E-02
S_{tot}	2.33E-05	6.76E-02	2.31E-01	4.42E-01	2.21E-01	3.56E-04	3.55E-02

Helium can be considered as a non-adsorptive gas in the low-pressure range, but it adsorbs when the pressure is elevated,[56] which is also proved by its slightly increasing apparent porosity in Figure 2-7. In fact, in the high-pressure range, helium porosity is larger than the CO_2 porosity because of the low adsorption of high-pressure CO_2 which will be discussed in detail in the adsorption section. No in-depth investigation of helium adsorption is covered in this work, as we focus on the comparison between low-pressure CO_2 and high-pressure CO_2. The mean value of helium porosity below 200 psi is 0.006, which is used as the intrinsic porosity of the core.

2.7 Gibbs adsorption and absolute adsorption

Adsorptive gas has higher apparent porosity due to the adsorbed phase being denser than the free gas phase. Adsorption can be discussed in terms of absolute and Gibbs/excess adsorption. Calculations of the two types of adsorption are different: the absolute adsorption takes into account of the volume occupied by the adsorption phase in the pore space; while the Gibbs adsorption assumes the adsorption phase does not occupy any volume in the pore space.[57] The following equations show the calculation procedures based on mass balance.

The total mass is expressed in terms of the apparent gas volume and the free gas density as follow:

$$m_{tot} = V_a \rho_g \tag{2-5}$$

The total mass equals the summation of the mass of adsorption and free gas as follow:

$$m_{tot} = m_{ads}^{G} + V_{void} \rho_g \tag{2-6}$$

$$m_{tot} = m_{ads}^{A} + (V_{void} - V_{ads}) \rho_g \tag{2-7}$$

where m_{ads}^{G} and m_{ads}^{A} are the mass of Gibbs and absolute adsorption, respectively. V_{void} is the volume of pore space which is determined as the helium porosity under low pressure. V_{ads} is the volume of the adsorbed phase.

By combining (6) and (7) the following equation relating Gibbs and absolute adsorption is obtained:

$$m_{ads}^{G} = m_{ads}^{A} - V_{ads}\rho_{g} \tag{2-8}$$

The mass of absolute phase is the multiplication of density and volume of adsorbed phase as follow:

$$m_{ads}^{A} = V_{ads}\rho_{ads} \tag{2-9}$$

By combing Eq. (2-8) and Eq. (2-9) the expression for the mass of the Gibbs adsorption phase is obtained:

$$m_{ads}^{G} = V_{ads}(\rho_{ads} - \rho_{g}) \tag{2-10}$$

Eq. (2-10) demonstrates the physical meaning of the Gibbs adsorption, which is the amount of "excess" if the volume of V_{ads} filled with free gas is replaced with adsorbed phase.

By combining Eq. (2-9) and Eq. (2-10) a more clear relationship between the Gibbs and absolute adsorption is obtained:

$$m_{ads}^{A} = \frac{m_{ads}^{G}\rho_{ads}}{\rho_{ads} - \rho_{g}} \tag{2-11}$$

It can be observed from Eq. (2-6) and Eq. (2-11) that density of the adsorbed phase is required for the calculation of absolute adsorption, but not for the calculation of Gibbs adsorption.

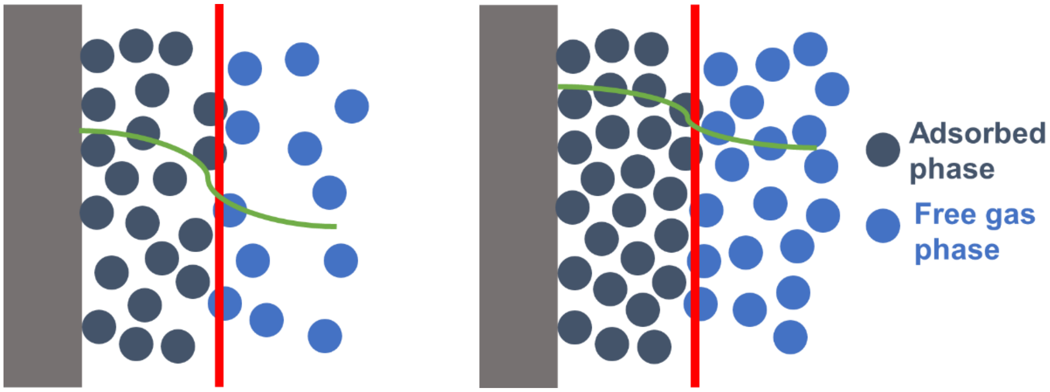

(a) (b)

Figure 2-8 Local density of adsorbed phase and free gas under (a) low pressure and (b) high pressure, based on Gasem et al.[58]

Figure 2-8 depicts the local density of the adsorbed phase and free gas phase away from the pore surface under low pressure and high pressure. Under low pressure the density of the adsorbed phase is much higher than the free gas phase; under high pressure the density of the adsorbed phase is closer to the free gas phase. It can be observed that the density of the adsorbed phase depends on both the location and pressure that it is not a constant. Density function theory has been frequently applied to model the detailed adsorption behavior, which is a computational modeling approach at the atom or the molecule level.[59-61] The Gibbs adsorption is the amount of "excess" using the density difference between the adsorbed phase and free gas phase. It can be seen that Gibbs adsorption is not the "actual" adsorbed amount (absolute adsorption), but the amount truly measured in the laboratory. To estimate the absolute adsorption directly from the Gibbs adsorption, the density of the adsorbed phase needs to be assumed. Under sufficiently high pressure, the Gibbs adsorption will become zero or even negative because the density of the free gas phase is equal to or larger than the adsorbed phase. A graphical method has been used to empirically obtain the adsorbed phase density by plotting the Gibbs adsorption amount as a function of bulk phase density at the point Gibbs adsorption equals zero.[62]

Only one data source for the nitrogen adsorption phase of 0.81 g/cm^3 is found in the literature and itis used to estimate the nitrogen absolute adsorption.[63,64] Pini applied the graphical method to estimate the CO_2 adsorbed phase density in clays and shales where the results vary significantly.[62] Based on the results on clays, the CO_2 adsorbed phase density ranges from 0.36 g/cm^3 to 0.94 g/cm^3; based on the results on shales, the value ranges from 0.83 g/cm^3 to 1.37 g/cm^3.[65-67] Considering the large variation of this value, a middle number of 0.85 g/cm^3 is selected in this study to estimate CO_2 absolute adsorption.

Gibbs (q_G) and absolute adsorption (q_A) are the volume gas adsorbed per unit mass of the rock, in the unit of scf/ton. They are expressed in Eq. (2-12) and Eq. (2-13), respectively.

$$q_G = \frac{2{,}000 m_G}{\rho_{std} m_r} \tag{2-12}$$

$$q_A = \frac{2{,}000 m_A}{\rho_{std} m_r} \tag{2-13}$$

where ρ_{std} is the density of gas under standard conditions, in the unit of lbm/ft^3. m_r is the mass of the matrix of the rock, in the unit of lbm. m_G and m_A are in the in the unit of lbm. q_G and q_A are in the unit of scf/ton. The 2,000 coefficient accounts for the unit conversion factor. The adsorption isotherms for nitrogen and CO_2 are plotted in Figure 2-8.

For CO_2, adsorption behaves differently in the low-pressure ranges compared to the high-pressure ranges. A crossover region is observed before and after the critical pressure point. Below the critical pressure, CO_2 adsorption increases monotonically as pore pressure increases. However, above the critical pressure, CO_2 adsorption drops sharply across the phase change region, and decreases as pore pressure continues to increase. The discontinuity of adsorption behavior of CO_2 has been evidenced by many researchers using active carbon and coal as adsorbents.[57, 68] The 2-D Peng-Robinson EOS model and Ono-Kondo model were frequently developed to characterize the adsorption behavior for the entire pressure range, in this study the above two models were not applied.[56, 69, 70]

The difference between Gibbs adsorption and absolute adsorption for low-pressure CO_2 is relatively small. Above the critical pressure, the difference increases phenomenally. This can be clearly explained by Eq. (2-14) based on Eq. (2-11): as the density of free CO_2 phase is getting closer to the density of the adsorbed phase, the denominator becomes smaller; thus, the absolute adsorption becomes much larger than the Gibbs adsorption. Therefore, larger fluctuation is observed for the CO_2 absolute adsorption result. It should be noted that the isotherms for the absolute adsorption are not unique because an accurate experimental estimation of the adsorbed phase density is not readily accessible. As a result, the Gibbs/excess adsorption is more of importance in this study.

$$q_A = \frac{q_G}{1 - \frac{\rho_g}{\rho_{ads}}} \qquad (2\text{-}14)$$

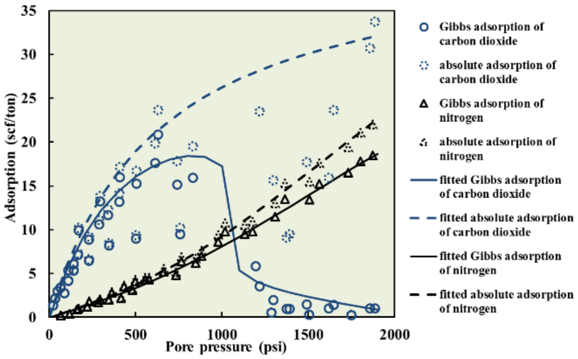

Figure 2-9 Gibbs and absolute adsorption as functions of pore pressure of nitrogen and carbon dioxide.

The multilayer BET model ((Eq. (2-15)) is chosen to fit the Gibbs and absolute adsorption isotherm of nitrogen.

$$q=\frac{q_m C\frac{p}{p_0}}{1-\frac{p}{p_0}}\left[\frac{1-(n+1)\frac{p}{p_0}+n\left(\frac{p}{p_0}\right)^{n+1}}{1+(C-1)\frac{p}{p_0}-C\left(\frac{p}{p_0}\right)^{n+1}}\right] \tag{2-15}$$

In Eq. (2-15), the saturation pressure p_0 is treated as the pseudosaturation pressure (p_s) for the supercritical-nitrogen adsorption.[71-73] The pseudosatruation pressure is estimated by Dubinin's empirical correlation for temperature above the critical temperature:[74]

$$p_s = p_c(\frac{T}{T_C})^2 \tag{2-16}$$

The Langmuir model ((Eq. (2-17)) is chosen to fit the absolute adsorption isotherm of carbon dioxide and a modified Langmuir model ((Eq. (2-18)) is used to fit the Gibbs adsorption isotherm:

$$q = q_m \frac{p}{p_L + p} \tag{2-17}$$

$$q = q_m \frac{p}{p_L + p}[1-\frac{\rho_g(P,T)}{\rho_{ads}}] \tag{2-18}$$

Table 2-7 Fitting parameters for N_2 and CO_2 adsorption isotherm.

	N_2 Gibbs/excess	N_2 absolute		CO_2 Gibbs/excess	CO_2 absolute
C, dimensionless	1.37	1.24	p_L, psi	629.42	628.06
n, dimensionless	4.54	4.75	q_m, scf/ton	39.71	42.70
q_m, scf/ton	9.61	11.50			

2.8 Porosity and its relationship with the adsorbate

Gas apparent porosity (ϕ_a) is defined as the ratio between gas apparent volume and the bulk volume of the core (Eq. (2-4)).

Based on mass balance, the following equation is established:

$$\rho_g \phi_a V_b = \phi_{void}\rho_g V_b + (1-\phi_{void})V_b \rho_a \tag{2-19}$$

where ρ_a is the mass of adsorbed gas per unit volume of the rock at standard condition (273.15 K, 14.7 psi) with the unit of lbm/ft^3. It is expressed as

$$\rho_a = \frac{\rho_{std}\rho_r q_G}{2{,}000} \tag{2-20}$$

where ρ_g is with the unit lbm/ft^3, and ρ_r is the rock density with the same unit. q_G is with the unit of scf/ton.

Eq. (2-19) can be simplified as

$$\phi_a = \phi_{void} + (1-\phi_{void})\frac{\rho_a}{\rho_g} \tag{2-21}$$

It should be noted that Eq. (2-21) is only valid with the assumption that the adsorbed phase does not occupy volume in the pore space which complies with the characteristic of Gibbs/excess adsorption. One important finding observed in Figure 2-7 is that CO_2 apparent porosity decreases as pressure increases, which is opposite with that of nitrogen and helium and contrary with the intuitive perception. This observation can be explained by the density ratio term (D_a):

$$D_a = (\frac{\rho_a}{\rho_g})_T \tag{2-22}$$

Figure 2-10a and Figure 2-9b plot ρ_a and ρ_g of CO_2 and nitrogen, respectively. The density of nitrogen increase linearly throughout the tested pressure; but the density of CO_2 increase rapidly before the phase change region then increases slowly after the phase change region. Figure 2-10c shows the density ratio plot of CO_2 and nitrogen. It can be observed that the changing trend of the density ratio directly reflects the changing trend of the apparent porosity, as compared with Figure 2-7. The amount of the free gas and the adsorbate can be evaluated by ϕ_{void} $(1-\phi_{void})$ and D_a, respectively (Figure 2-10d). It can be seen that the equivalent volume of the adsorbate continues to decrease for CO_2 and continues to increase for N_2. The amount of adsorbate is more than ten times of the free gas phase for CO_2 under low pressure. Figure 2-11 shows the sketch to more clearly demonstrate the relationship between the adsorbed phase, the free gas phase and the apparent pore volume for the low-pressure CO_2. Even though the adsorbate volume (black box) is increasing with pressure, the equivalent free gas volume (blue box) from the adsorbate does not necessarily increase because the density of free gas increases rapidly, leading to the decrease of total apparent volume, which is summation of the intrinsic pore volume and the equivalent free-gas volume from the adsorbate. After the phase change region, the adsorbate density decreases but the free gas density still increases, leading to the further decrease of both the density ratio and the apparent pore volume.

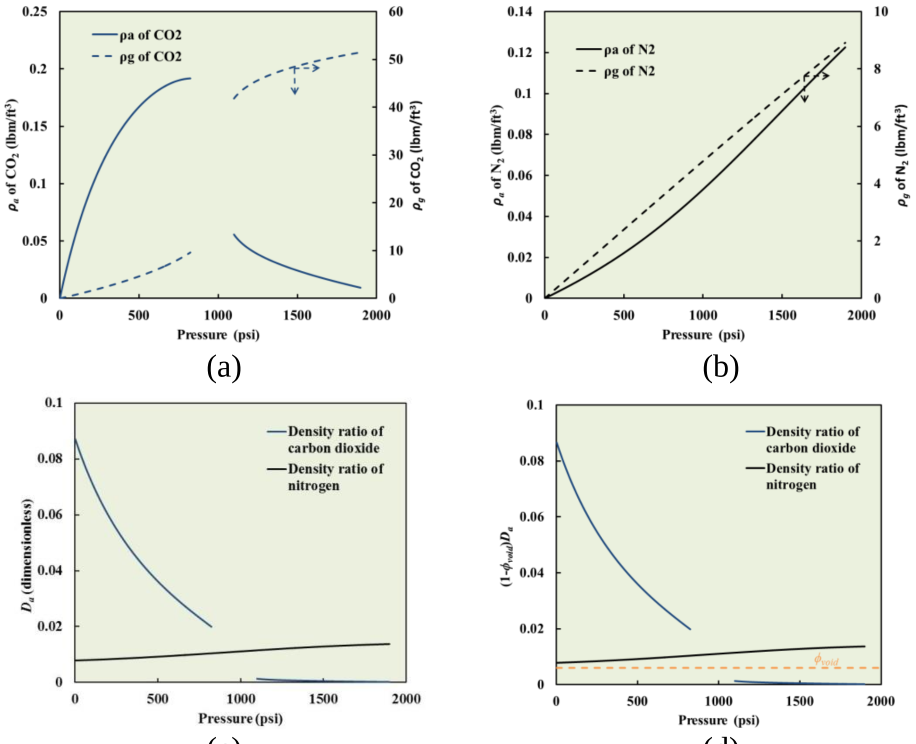

(a) (b)

(c) (d)

Figure 2-10 (a) ρ_a and ρ_g of CO_2; (b) ρ_a and ρ_g of N_2 (c) Density ratio (D_a) of CO_2 and N_2 (d) $(1-\phi_{void})D_a$ of CO_2 and N_2.

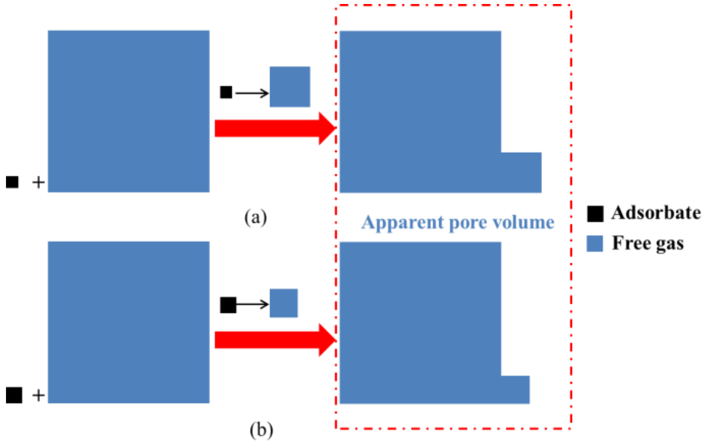

Figure 2-11 A sketch of the relationship between the adsorbed phase, free gas and apparent pore volume of CO_2 below the critical pressure (a) under low pressure (b) under higher pressure.

2.9 Permeability and its relationship with the adsorbate

The governing equation for adsorptive gas flow in porous media is expressed as:

$$\frac{\partial}{\partial l}\left(\frac{\rho_g k_a \partial p}{\mu_g \partial l}\right)=\frac{\partial(\phi_a \rho_g)}{\partial t} \tag{2-23}$$

By taking the partial derivative of the RHS of Eq. (2-23) and inserting Eq. (2-21):

$$\phi_a \frac{\partial \rho_g}{\partial t}+\rho_g \frac{\partial \phi_a}{\partial t}=\phi_a \frac{\partial \rho_g}{\partial t}+\rho_g(1-\phi_{void})\frac{\partial({}^{\rho_a}\!/\!{}_{\rho_g})}{\partial t} \tag{2-24}$$

By applying the rule of partial derivative for ρ_a/ρ_g at the RHS of Eq. (2-24) and applying chain rule, Eq. (2-25) is obtained:

$$\frac{\partial}{\partial l}\left(\frac{\rho_g k_a \partial p}{\mu_g \partial l}\right)=[\phi_{void}+(1-\phi_{void})\frac{\partial \rho_a}{\partial \rho_g}]\frac{\partial \rho_g}{\partial t} \tag{2-25}$$

Gas compressibility is expressed as:

$$c_g=\frac{1}{\rho_g}\left(\frac{\partial \rho_g}{\partial p}\right)_T \tag{2-26}$$

After applying Eq. (2-26) into the RHS of Eq. (2-25) with chain rule, the final form of the governing equation is obtained:

$$\frac{\partial}{\partial l}\left(\frac{\rho_g k_a \partial p}{\mu_g \partial l}\right) = [\phi_{void} + (1-\phi_{void})\frac{\partial \rho_a}{\partial \rho_g}]c_g \rho_g \frac{\partial p}{\partial t}. \tag{2-27}$$

Then we can observe ϕ_{app} is different from the apparent porosity ϕ_a:

$$\phi_{app} = \phi_{void} + (1-\phi_{void})K_a \tag{2-28}$$

The term of the partial derivative of ρ_a over ρ_g is defined as the differential partitioning coefficient:[6, 75]

$$K_a = \left(\frac{\partial \rho_a}{\partial \rho_g}\right)_T \tag{2-29}$$

K_a can be expressed as the ratio between ρ_a gradient and ρ_g gradient:

$$K_a = \left(\frac{\partial \rho_a}{\partial \rho_g}\right)_T = \left(\frac{\partial \rho_a}{\partial p}\right)_T \Big/ \left(\frac{\partial \rho_g}{\partial p}\right)_T \tag{2-30}$$

Figure 2-12 shows the gradient of ρ_a and ρ_g, and K_a as functions of pressure for CO_2 and N_2. Unlike nitrogen, the gradient of ρ_a of CO_2 slightly decreases as pressure increases; and its value becomes negative above the critical pressure. The gradient of ρ_g of CO_2 increases sharply below the critical pressure then decreases sharply above the critical pressure, leading to the unique characteristic of K_a for CO_2. K_a value depends on the competing changing rate of the adsorbate density and the free gas density. Yu et al. (2016) compared free gas and adsorption/desorption by comparing ϕ_{void} and (1- ϕ_{void})K_a. However, one should note that K_a does not have any physical meaning; and it is only formed during re-organization and manipulation of the governing equation. One should be very cautious to use it to evaluate the impact of adsorption/desorption on the apparent gas porosity, or the total gas in place (GIP), because it is strongly coupled within the governing transport equation. The contribution of adsorption on GIP should be evaluated by the density ratio D_a.

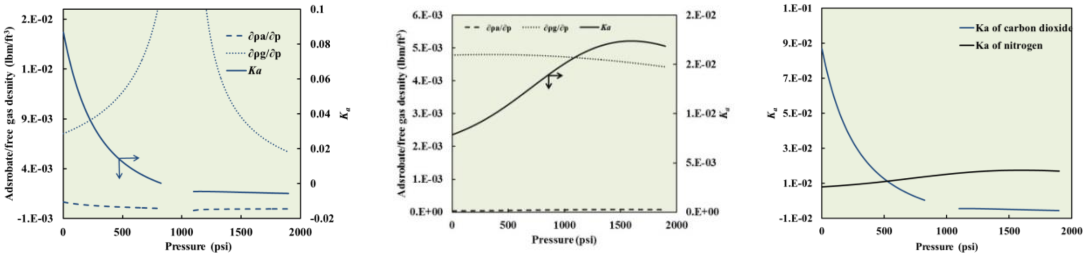

(a) (b) (c)

Figure 2-12 (a) $\partial\rho a/\partial p$ and $\partial\rho g/\partial p$ of CO_2; (b) $\partial\rho a/\partial p$ and $\partial\rho g/\partial p$ of N_2 (c) *Ka* of CO_2 and N_2.

The non-adsorptive gas apparent transport in the porous media is expressed by the governing equation Eq. (2-31).The gas apparent permeability can be obtained analytically based on the boundary condition and initial condition of the experiment.

$$\frac{\partial}{\partial l}\left(\frac{\rho_g k_{ads-free}\partial p}{\mu_g \partial l}\right)=\phi_{void}\frac{\partial \rho_g}{\partial t} \tag{2-31}$$

The initial conditions are:

$$p(0,0)=p_u(0) \tag{2-32}$$

$$p(l,0)=p_d(0) \tag{2-33}$$

The boundary conditions at the two ends of the core plug are:

$$p(0,t)=p_u(t) \tag{2-34}$$

$$p(l,t)=p_d(t) \tag{2-35}$$

$$\left.\frac{\partial p_u}{\partial l}\right|_{l=0}=-\frac{\mu_g c_g V_u}{k_{na}A}\frac{\partial p_u}{\partial t} \tag{2-36}$$

$$\left.\frac{\partial p_d}{\partial l}\right|_{l=L}=\frac{\mu_g c_g V_d}{k_{na}A}\frac{\partial p_d}{\partial t} \tag{2-37}$$

where *L* is the core length and *A* is the cross-section area.

The dimensionless pressure drop can be defined as:

$$\Delta p_D = \frac{p(l,t) - p(0,t)}{p(l,0) - p(0,0)} \tag{2-38}$$

A linear slope s will be obtained if the semi-log of Δp_D is plotted against time t (Figure 2-12).

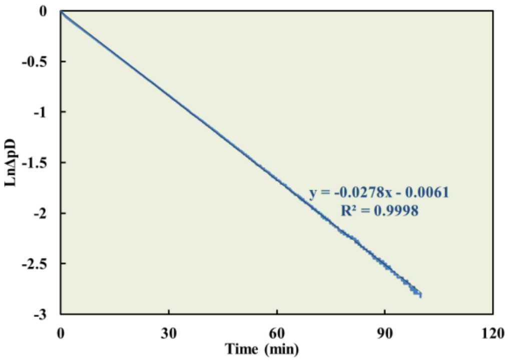

Figure 2-13 A typical plot of LnΔP_D as a function of time.

The apparent permeability $k_{ads\text{-}free}$ can be estimated by the analytical solution

$$k_{ads-free} = 1.689 \times 10^{15} \frac{c_g \mu_g \phi_{void} L^2 \,|\, s \,|}{f(a,b)} \tag{2-39}$$

where $k_{ads\text{-}free}$ is with the unit of nD, c_g is with the unit of Pa^{-1}, μ_g is in the unit of Pa·s, l is with the unit of cm, and s is with the unit of 1/min. 1.689 ×10^{15} accounts for the unit conversion factor. The Appendix A provides procedures to estimate c_g and μ_g based on the work of Abou-Kassem et al. and Sutton,[76, 77] respectively. *f(a,b)* is the square of the first solution of a series of θ in the transcendental equation:

$$tan\theta = \frac{(a+b)\theta}{\theta^2 - ab} \tag{2-40}$$

f(a,b) can be approximated by the polynomial:

$$f(a,b) = \theta_1^2 = (a+b+ab) - \frac{1}{3}(a+b+0.4132ab)^2 + 0.074(a+b+0.0578ab)^3 \tag{2-41}$$

a and b are the volume ratios between the pore volume and the reservoir volume:

$$a = \frac{V_b \phi_{void}}{V_{u1} + V_{u2}} \tag{2-42}$$

$$b = \frac{V_b \phi_{void}}{V_d} \tag{2-43}$$

The above procedures are repetition based on the work of Heish et al. and Dicker and Smits.[4, 5] The size of pulse should be kept below 10% for measurement accuracy according to Dicker and Smits because the gas properties can be assumed to be constant.[5] However, the analytical solution is still applied for the scenario with a large pulse size in this study. Indeed, small differences are observed between the adjacent data points with small pulse size and big pulse size (Figure 2-14a), but the accuracy is quite acceptable. Figure 2-14 shows the apparent permeability and Knudsen number for the three types of gas.

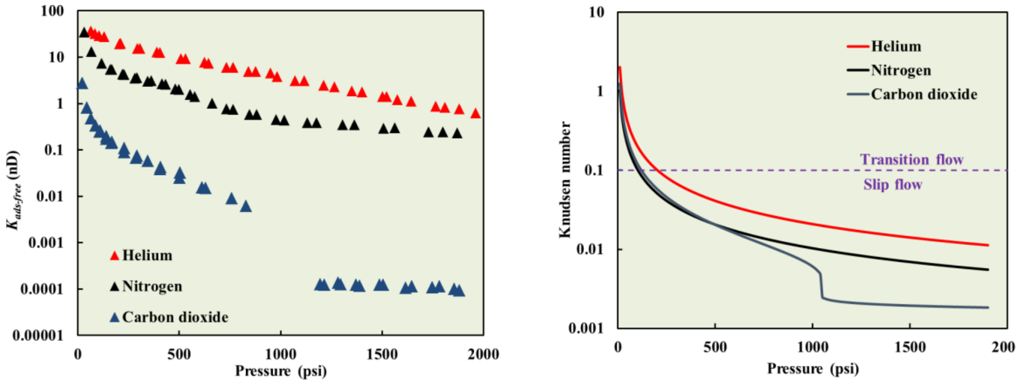

(a) (b)

Figure 2-14 (a) Apparent permeability and (b) *Kn* of helium, nitrogen and carbon dioxide as functions of pore pressure.

Knudsen number (Eq. (2-20)) is defined as the ratio between gas mean free path and the characteristic length of the pore. It is frequently used to define flow regimes in the tight porous media. Based on the PSD in Figure 2-6, the pore size used in the Knudsen number estimation is assumed to be 100 nm. It could be observed in Figure 2-14b that the flow regimes fall in the slip flow region and transition flow region. When the Knudsen number ranges from 0.001 to 0.1, the flow regime is slip flow when the gas molecule starts to slip on the pore surface. Pore diffusion (including both Fickian diffusion and Knudsen diffusion) occurs along with the slip flow in the transition flow regime when the Knudsen number ranges between 0.1 and 10. We can see the change of gas apparent permeability is in accordance with the change of K_n. Helium has the highest apparent permeability and its mean free path is the longest among the three types of gas. The difference between the permeability of nitrogen and CO_2 becomes more noticeable as pore pressure increases because the mean free path of CO_2 is reduced sharply when the pressure approaches its critical pressure. It could be reasonably expected that the permeability difference of different types of gas is lessened under higher temperature because the EOS for all types of gas become more and more close to the ideal gas law. These observations are in agreement with various models available in the literature attempted to describe the relationship between the intrinsic permeability and the apparent permeability with the correction factor *f(Kn)*,[16-18] which is positively related with the Knudsen number. In this study, we aim to provide a reliable database with detailed data of gas dependent petrophysical properties in tight porous media over a wide range of pressure, but did not estimate the applicability of various models describing the flow mechanisms.

$$K_n = \frac{k_B T}{\sqrt{2}\pi d_{mol}^2 p d} \tag{2-44}$$

$$f(Kn) \propto Kn \tag{2-45}$$

For the non-adsorptive gas, the "permeability" measured by the pulse-decay lumps together all the transport mechanisms (viscous flow, slip flow and pore diffusion) to be equivalent to the so-called "apparent permeability" $k_{ads\text{-}free}$ using the Darcy's equation. In addition, adsorption also has complex impacts on gas transport efficiency. On one hand, the adsorbed phase reduces the intrinsic permeability by reducing the effective pore size because it occupies some volume in the pore space. On the other hand, because *f(Kn)* is positively related with the Knudsen number, the effective pore size reduction leads to Kn increase which subsequently leads to $f(Kn)$ increase.[78] Besides, surface diffusion forms between the free gas phase and the adsorbed phase where gas molecules move along the matrix surface by a hopping mechanisms.[79] Gas apparent permeability is significantly enhanced because of surface diffusion especially in micropores with the pore radius less than 2 nm.[80] If ϕ_{app} is used instead of ϕ_{void} in the governing equation, then the estimated permeability by the analytical solution will be the permeability to be taken into account for the calculation of the adsorption effect (k_a). Therefore, the fractional contribution of the adsorption to the apparent permeability can be estimated macroscopically by the (k_a-$k_{ads\text{-}free}$)/ $k_{ads\text{-}free}$ ratio, as illustrated in Figure 2-15. It can be seen that the change of the fraction is consistent with the change of K_a. For nitrogen, the fraction increases then reaches a plateau at the end of the tested pressure range; and for CO_2, the fraction is high under low pressure and it can reach as high as 15% when the CO_2 apparent porosity is 14%. It continues to decrease and becomes negative when the pressure reaches above the critical pressure, indicating that the adsorption begins to be unfavorable for the gas transport efficiency. In addition, one can see When CO_2 apparent porosity is about three times than that of the intrinsic porosity (at about 750 psi in Figure 2-7), the permeability contribution fraction is very close to zero. It indicates that when the porosity becomes slightly higher if the "pressure compensation" practice is not applied, the estimated permeability will be negligibly affected because both the porosity in the numerator and $f(a,b)$ in the denominator increase, their net effect on the permeability determination will be very small.

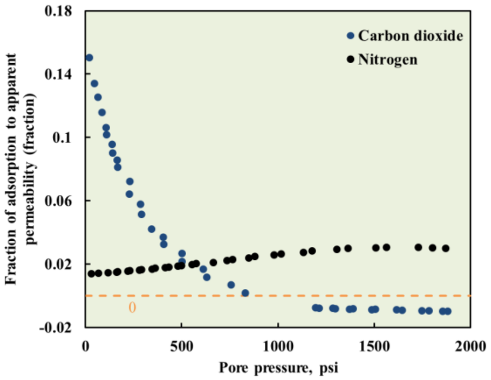

Figure 2-15 Fraction of adsorption contribution to the apparent permeability of CO_2 and N_2.

2.10 Conclusions

A comprehensive investigation of low-pressure and high-pressure CO_2 petrophysical properties in a shale core plug is covered in this work, in comparison with that of helium and nitrogen. The focus is to understand CO_2 flow behavior in a wide range of pressures which is closely related with the adsorption profile; further, different definitions of permeability and porosity are clarified. The following conclusions are drawn from this work:

The pulse decay method introduces uncertainties when measuring gas apparent porosity in tight porous media, especially for high-pressure tests. A routine sensitivity and uncertainty analysis proposed in this study help control the uncertainties and improve accuracy of measurement.

Apparent porosity is significantly increased because of the adsorption. The apparent porosity of adsorptive gas relates the intrinsic porosity with the density ratio (D_a) between the adsorbate density and free gas density. Apparent porosity and Gibbs/excess adsorption of CO_2 decrease continuously during the whole pressure range and declines sharply above the critical pressure, which is opposite to the change of nitrogen.

Three types of permeability are required to systematically study adsorptive gas flow behavior in the tight porous media. They are intrinsic permeability (k_∞), gas apparent permeability (k_a) and gas apparent permeability without the impact of adsorption ($k_{ads\text{-}free}$).

Helium has the highest apparent permeability among the three types of gas. The difference between the permeability of CO_2 and nitrogen becomes more significant as pressure increase. These trends are in accordance with the trend of mean free path and Knudsen number.

The differential partitioning coefficient (K_a) different from the density ratio (D_a) is involved in the adsorptive gas transport governing equation in the porous media. The change of K_a is consistent with the change of the fractional contribution of adsorption to the apparent permeability. The fraction adsorption contribution permeability is high under low pressure for CO_2 but is high under high pressure for nitrogen. This contribution becomes negative above the critical pressure; these phenomena can be explained by the unique characteristic of the K_a of CO_2.

2.11 Nomenclature

a	Volume ratio between pore volume and the upstream reservoir volume, dimensionless
b	Volume ratio between pore volume and the downstream reservoir volume, dimensionless
A	Area of the cross-section of the core, m^2
C	Constant in BET model, dimensionless, dimensionless
c_g	Gas compressibility, 1/psi or 1/Pa
D	Downstream reservoir
D_a	Density ratio between the adsorbate and free gas, dimensionless
k_a	Gas apparent permeability, nD or m^2
$k_{ads\text{-}free}$	Gas apparent permeability without the impact of adsorption, nD or m^2
K_a	Partitioning coefficient, dimensionless
n	Index in BET model, dimensionless

m_{ads}^{G}	Mass of Gibbs adsorption, g or lbm
m_{ads}^{A}	Mass of Gibbs adsorption, g or lbm
m_r	Rock mass, g or lbm
m_{tot}	Total gas mass including adsorption and free gas, g or lbm
p	Pressure, psi or Pa
p_0	Saturation pressure, psi or Pa
p_d	Downstream reservoir pressure, psi or Pa
p_e	Equilibrium pressure, psi or Pa
p_L	Langmuir pressure, psi or Pa
p_u	Upstream reservoir pressure, psi or Pa
q_A	Absolute adsorption, gas volume adsorbed per unit mass of the rock, scf/ton
q_G	Gibbs adsorption, gas volume adsorbed per unit mass of the rock, scf/ton
q_m	Maximum adsorption in BET and Langmuir model, scf/ton
R	Universal gas constant, 8.314 J/(mol·K)
S	Sensitivity index based on Sobol's index, dimensionless
S_{fast}	Sensitivity index based on Fast Fourier Transformation, dimensionless
S_{tot}	Sensitivity index based on Sobol's index, dimensionless, dimensionless
T	Temperature, K
U_1	First upstream reservoir
U_2	Second upstream reservoir
V_a	Apparent gas porosity, dimensionless
V_{ads}	Volume of adsorption phase, cm^3or ft^3
V_b	Bulk volume of the core, cm^3or ft^3

V_d	Downstream reservoir volume, cm^{3}or ft^3
V_{fg}	Volume of free gas phase, cm^{3}or ft^3
V_p	Total pore volume, cm^{3}or ft^3
V_u	First upstream reservoir volume, cm^{3}or ft^3
V_{u2}	Second upstream reservoir volume, cm^{3}or ft^3
Z	Compressibility factor, dimensionless
Z_d	Compressibility factor at downstream reservoir, dimensionless
Z_e	Compressibility factor at equilibrium state, dimensionless
Z_u	Compressibility factor at upstream reservoir, dimensionless
μ_g	Viscosity, Pa·s
ρ_a	Mass of adsorbed gas per unit volume of rock, g/cm^3 or lbm/ft^3
ρ_{ads}	Density of adsorption phase, g/cm^3 or lbm/ft^3
ρ_b	Rock density, g/cm^3 or lbm/ft^3
ρ_g	Density of free gas, g/cm^3 or lbm/ft^3
ρ_g	Gas density, g/cm^3 or lbm/ft^3
ϕ_{void}	Intrinsic porosity, dimensionless
ϕ_a	Apparent porosity, dimensionless
ϕ_{app}	Apparent porosity in the transport governing equation, dimensionless

Chapter 3 Pulse-decay experiments in the fractured core

This chapter is a copy of the published paper “Experimental and numerical investigations of permeability in heterogeneous fractured tight porous media” in *Journal of Natural Gas Science and Engineering* (October 2018, 58: 216-233) with format change after purchasing the copyright through Rightslink. Elsevier holds the copyright for this chapter. This chapter should be downloaded for only personal use, and further use of the materials in this chapter should purchase the copyright from Elsevier.

3.1 Summary

Analyzing gas flow behavior is important for production prediction in heterogeneous fractured shale reservoirs, which is complex due to the presences of nanopores and high-degree heterogeneity in these complex flow network. First, we applied the discrete fracture model to simulate gas pulse-decay experiments in core plugs with different configurations. The effective permeability ratio was proposed to evaluate the effects of heterogeneity, fracture, and vug on the flow behavior. Second, we performed pulse-decay experiments on one intact fractured shale core to examine the effects of pore pressure and effective stress on permeability variations. The measured pressure profiles were history matched by numerical methods to obtain the porosity and permeability of matrix and fracture. The matching degree is evaluated by the Global Matching Error (GME). Our results highlight the positive impact of dense fracture network to improve flow capacities in the tight reservoir: effective permeability of the fractured core with 8 pairs of 1.3-cm connected fractures increases 4.07 times that of the un-fractured core. Vugs might be important as well if they connect adjacent fracture networks, but their own contribution to flow capacity is negligible: effective permeability increases only 1.00 to 1.02 times when the number of vugs increase from 3 to 35. The GME ranges from 0.04% to 0.2% for history matching of the fractured

core. Core heterogeneity is exhibited more obviously when gas flows through under low pressure than under high pressure, which can be used to guide the design of pulse-decay experiment properly depending on the purpose. The main contributions of this study are that we constructed the finite-element based numerical model to simulate the pulse-decay experiment, proposed a methodology to upscale core permeability when fractures and vugs are present, and measured porosity and permeability for the matrix and fracture simultaneously in one fractured core over a wide range of pressure and effective stress.

3.2 Introduction

Shale gas is a major component of natural gas supply around the world. Shale gas production is projected to account for about two-thirds of the total natural gas production in the U.S. by 2040.[81] Fractures, both natural and hydraulic, are important for the development of unconventional shale gas and oil reservoirs, as they provide the fast flow path for fluids moving from the matrix to the wellbore because of their great transport capacity.[82, 83] Besides, shale reservoirs are highly heterogeneous with permeability from nanodarcy scale in micro-pores to microdarcy scale in macropores.[84, 85] Therefore, it is essential to quantify and upscale the flow capacity of the fractured shales in terms of the effective permeability. On the other hand, fracture and vugs are important features of some carbonate reservoirs that they present multiple types of fluid flow in the matrix, cavities and fractures.[86] Understanding transient flow behavior is important in such fractured and vuggy formations to analyze production behaviors of tight gas reservoirs during primary depletion process.

Pulse-decay method to estimate permeability of tight porous media is based on the transient fluid pressure transmission process.[87, 88] Properties of the tested core samples can be obtained by interpreting the pressure data. Based on the initial pressures and the equilibrium pressure, as well as the volume of reservoirs and core bulk volume, porosity can be estimated from the Boyle's law after accounting for the non-linear compressibility factor of the tested fluid. A lower equilibrium pressure indicates a large pore volume. The laboratory determined permeability is the apparent value depending on flow conditions. In tight porous media, slip flow, Knudsen diffusion, and surface diffusion all contribute to the apparent permeability.[89-91] In contrast, the inherent permeability only depends on the pore structure of the porous media.[87] The pulse-decay system mainly contains three components: the upstream reservoir, core, and downstream reservoirs. Pressure build-up and decline curves can be obtained at the downstream and upstream reservoirs, respectively, after the pulse-decay test.

Previous researchers have derived analytical solutions for the gas pressure pulse-decay process. Brace et al. first applied the transient pulse-decay experiment to measure the permeability of granite, and they provided one solution assuming no compressive storage in the porous media.[1] The main drawback of the solution by Brace et al. is that the pore volume of the core sample is assumed to be negligible. Therefore, the accuracy of their solution is compromised. Hsieh et al. provided a comprehensive analytical solution to describe the transient pressure transmission process by introducing the compressive storage effect.[4] Dicker and Smits further simplified the analytical solution with high accuracy for fast engineering application.[5] Cui et al. improved the solution taking into account of adsorption/desorption when the flowing fluid is adsorptive gas.[6] In addition to the analytical method, the flow process can be simulated numerically based on the initial and boundary conditions of the system.[3] Jia et al. presented a study of flow behaviors of multiple types of gas in shale core plugs.[88] In that study, the apparent permeability of the gases and adsorption profile in forms of Gibbs and absolute adsorption were measured over a wide range of pressure, and the complex relationships between adsorption and permeability were also investigated comprehensively.[57] Jia et al. conceptually modeled pressure behaviors in heterogeneous core plugs with and without the presence of a fracture, and experimentally explored the core heterogeneity effect on the flow behavior by flowing gas from one direction and the opposite direction.[46]

Exploration of the multiscale, double porosity feature of tight core plugs using gas as flowing fluid in the pulse-decay experiment was started by Ning et al.[92] Ning et al. provided analytical solutions for the gas pressure pulse transmission process in homogeneous and fractured cores with open and closed end.[92] They also developed an in-house finite difference simulator to simulate the flow process in ultra-low permeability core plugs. Almost at the same time, Kamath et al. demonstrated the applicability of estimating properties of matrix and fracture using water as the flowing fluid in conventional fractured core plugs.[93] In recent years, Cronin developed layered dual permeability model validated by experimental data performed on cement core plugs.[94] Fractures he studied in the simulation can be planar and orthogonal. Bhandari et al. characterized stress-dependent porosity and permeability of Barnett shale using core plugs with horizontal bedding and vertical bedding by the pulse-decay experiment.[95] They found that the horizontal-bedding core is more permeable than the vertical-bedding core. Preferential flow path was found by observing a double porosity region formed in the pressure curves before reaching final equilibrium, which is suggested to be attributed to the existence of multiscale permeability with more permeable organic-rich matter and less permeable siliceous matter. A problem of characterizing the fracture flow is the inertia effect associated with the turbulent flow, especially under high-pressure gradients. Turbulent flow, in nature, is extremely sensitive to disturbance in boundary and inlet conditions arose during the experimental operations.[96] This fact induces the uncertainty of fracture flow that can be hardly avoided that the transient process makes the flow phenomenon more unpredictable. However, the analytical and numerical solutions are deterministic and cannot predict the inherent uncertainty of fracture flow present in real laboratory experiments and the field.

Theoretically, both fracture permeability and porosity decrease as the effective stress increases,[97] corresponding to the fact that natural fracture tends to close as pore fluids are withdrawn from the reservoir. This phenomenon has been identified by several scholars using the conventional method where the fracture permeability is estimated based on the Darcy equation when fluid flows through the fracture with a constant flow rate under steady state. For instance, Jones showed through experiments that the cubic root of fracture permeability is linearly correlated with the confining pressure.[98] Gangi derived the function of fracture permeability with effective stress accounting for the distribution patterns of the asperity height.[99] To reduce the effect of turbulent flow in the fracture, the flow rate was always controlled to be very low meaning that the tested pressure gradient was very low. However, only measuring properties under low pressure lessened the significance of the original purpose because gas pressure in most reservoirs is usually thousands of psi especially in deep shale gas reservoirs. Alnoaimi applied pulse-decay on fractured Eagle Ford and Haynesville shales with the maximum effective stress of 2,000 psi and pore pressure of about 700 psi.[100] He collected three to four data points per series to investigate pressure and stress-dependent porosity and flow capacity for both the matrix and fracture, by the approach of history matching the upstream and downstream pressure curves. After reviewing his collected data points, it can be found that trends of these target properties as functions of pore pressure/stress are not very consistent. In the authors' opinion, three to four data points might be not enough to represent the whole pressure range especially when the range covers several hundred psi that the conclusions from the trend analysis might be questionable. We believe that a large set of experimental data pool are required to evaluate the feasibility of simultaneously estimating petrophysical properties of the matrix and fracture using the pulse-decay technique, which is the first objective of this study. The second objective is to use discrete fracture model (DFM) to characterize the transient flow process at the core-scale. DFM, representing fractures explicitly, has come to play an important part in fractured reservoir simulation. It has the advantage of better capturing the transfer phenomenon between the matrix and fractures and expressing fractures with various shapes.[101, 102] However, to the best of our knowledge, until now, no work has been presented in the open literature using DFM to simulate the transient pressure transmission process at the core-scale to interpret the effective permeability. Therefore, we aimed to fill this gap by comprehensively studying effects of multiscale features including heterogeneity, fracture, and vugs.

Our objectives of this study are to (1) construct a two-dimensional model to evaluate effective permeability ratio of complex tight porous media in the presence of fractures and vugs, based on the analytical solution describing the transient flow process, and compare the transient method with the steady-state method; (2) establish a large data pool by conducting pulse-decay experiments on fractured cores under different pore pressure and effective stress and estimate the matrix and fracture permeability, porosity and permeability dependency on the pore pressure and the effective stress by history matching the upstream and downstream pressure curves.

3.3 Numerical study based on DFM

In this section, we presented the construction of a 2D DFM to determine the ratio of effective permeability of complex core configurations over that of the matrix numerically. We included heterogeneous, fractured, vuggy, fractured and vuggy scenarios to evaluate the extent of permeability change due to the presence of heterogeneity, fracture, and vugs in the test core sample. Both the transient method and the steady-state method were applied to evaluate the effective permeability ratio.

Figure 3-1a shows three main components of the pulse-decay system: upstream reservoir (U), core and downstream reservoir (D). Figure B1 shows the schematic for the experimental set-up. The first, second, and third rectangular part represent the upstream reservoir, core, and downstream reservoir, respectively. The upstream reservoir is connected to the core, and its initial pressure is higher than the core pressure. The model is built in COMSOL Multiphysics 5.2a. No-flow boundary conditions are exerted on the outlines of the schematic. Lengths in the x-direction are 0.33 cm, 7.85 cm and 0.3 cm for upstream, core and downstream, respectively, and 3.38 cm in the y-direction, mimicking the real laboratory set-up in two dimensions. The matrix permeability and porosity are set to be 600 nD and 6%, respectively. There are 10 fractures (represented by lines) with the length of 1.3 cm and the width of 0.1 cm in Figure 3-1a. We first place vugs at intersection points and end points of the fractures, then place them outside of the fractures to investigate the effect of vugs' location on affecting the permeability. Figure 3-2b shows the discretization with triangles of the model. Maximum and minimum of the mesh size is set to be 0.568 cm and 2.54E-3 cm, respectively. The mesh size becomes smaller near the vug and is kept the same inside the vug (Figure 3-1c). We exert eight boundary layers at the interface between upstream/downstream reservoirs and the core surfaces, in order to improve the numerical convergence and capture the flow phenomenon closely during the rapid transient pressure change. Initially, core pressure and the downstream are under the same pressure, p_d, which is 500 psi, and the upstream is under pressure, p_u, 600 psi. As time elapses, the downstream pressure begins to build up and the upstream pressure begins to decline. Finally, equilibrium pressure is obtained in the whole system.

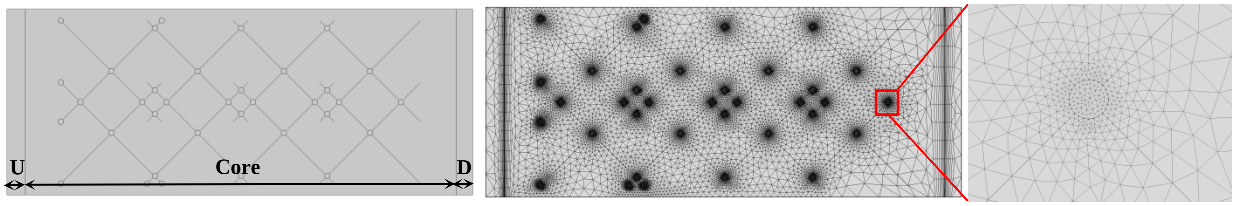

(a) (b) (c)

Figure 3-1 (a) Model with fractures (lines) and vugs (circles); (b) triangulation of the fractured and vuggy system; and (c) zoomed in picture of the squared area in (b) The vugs are distributed at the intersections and ending points of the fractures.

In this model, we express the fracture as inner boundaries between matrix blocks with setting the fracture width. The advantage of expressing fractures as boundaries instead of a specific geometry is that no numerous meshes are needed for the long and narrow fractures with high aspect ratios. However, the vugs have to be expressed with a certain geometry that the shape of circle is chosen in this work. Figure 3-1c shows mesh generations inside and outside of one vug. In the matrix, the time-dependent mass balance equation is described as:

$$\frac{\partial}{\partial t}(\phi\rho)+\nabla\cdot(-\rho\frac{k}{\mu}\nabla p)=Q_m \tag{3-1}$$

where ϕ is porosity, ρ is gas density, k is permeability, μ is viscosity, p is pressure, and Q_m is the accumulation term. The velocity in the matrix is then defined as

$$\overrightarrow{u_m}=-\frac{k}{\mu}\nabla p \tag{3-2}$$

where the subscript "*m*" indicates matrix. No flow boundary conditions are exerted on faces of the triangular mesh, which is realized by setting the vector product between the normal vector on the boundary and velocity vector to be zero

$$\vec{n}\cdot\overrightarrow{u_m}=0 \tag{3-3}$$

Fluid flow in vugs also follows Darcy's law except that porosity is set to be unity and permeability is set to be very high, 10 D, which is several orders magnitude larger than the matrix permeability. We performed a sensitivity analysis by changing 10 D to 1D and found the simulation result is not affected, validating that the assumption of this number is reasonable.

In the fractures the fluid flow follows the modified Darcy's law taking into account of the fracture's width:

$$w_f \frac{\partial}{\partial t}(\phi\rho) + \nabla_T \cdot (-w_f \rho \frac{k_f}{\mu} \nabla_T p) = w_f Q_m \tag{3-4}$$

where w_f is the fracture width. We included w_f in the flow equation to investigate the effect of its variation on the effective permeability by changing it from 0.001 cm to 0.1 cm in the model. The subscript "*T*" denotes the gradient is restricted to the tangential plane of the fracture. The velocity in the fracture is defined as

$$\overrightarrow{u_f} = -\frac{k_f}{\mu} \nabla_T p \tag{3-5}$$

Fluid flow in the system accounts for interactions between matrix themselves, between fractures/vugs themselves, and between matrix and fractures/vugs. Therefore we can simulate the pulse-decay experiment, which is the gas transient flow process in the complex tight flow media including fractures and vugs. For the transient flow process, it is valuable to obtain an effective permeability for the flow media for the upscaling purpose.

Dicker and Smits expressed the permeability from the pulse-decay experiment as:[5]

$$k_{eff} = \frac{c\mu\phi_{eff} L^2 |s_{eff}|}{f_{eff}(a,b)} \tag{3-6}$$

where c is gas compressibility, μ is gas viscosity, "*eff*" denotes the effective values in comparison with the base case only containing matrix, a and b are volume ratios between pore volume and reservoir volumes and $f(a,b)$ is a polynomial consisting of a and b:

$$a = \frac{V_p}{V_u} \tag{3-7}$$

$$b = \frac{V_p}{V_d} \tag{3-8}$$

$$f(a,b) = a + b + ab - \frac{1}{3}(a + b + 0.4132ab)^2 + 0.0744(a + b + 0.0578ab)^3 \tag{3-9}$$

s is the slope of the linear part of the natural logarithmic of dimensionless pressure, Δp_D, with time, which is defined as:

$$\Delta p_D = \frac{p_u(t) - p_d(t)}{p_u(0) - p_d(0)} \tag{3-10}$$

For pulse-decay experiments on different cores with the same length and same initial pressures, we propose to use the ratio in Eq. (2-11) to evaluate the effective permeability of the core plug in presences of fractures and vugs (k_{eff}) in comparison to the base case with the pure matrix (k_b). If the ratio is larger than 1, indicating that the flow process in the core plug is accelerated; on the contrary if the ratio is smaller than 1 indicating the flow process is hampered. It is worthy to note that c and μ are canceled out in this expression because the pressures in the upstream and downstream are the same; ϕ_{eff}, s_{eff} and $f_{eff}(a,b)$ influence one another that they should be studied altogether. ϕ_{eff} accounts for the variation of porosity and $f_{eff}(a,b)$ accounts for variations of upstream and downstream volumes. Therefore, the effective permeability ratio can be demonstrated as

$$\frac{k_{eff}}{k_b} = \frac{\phi_{eff} s_{eff}}{f_{eff}(a,b)} \frac{f_b(a,b)}{\phi_b s_b} \tag{3-11}$$

where $f_b(a,b)$ and ϕ_b are values in the base cases that only matrix is present in the core. This ratio is used throughout the study to investigate impacts of core heterogeneity, fractures and vugs on flow behavior in comparison with the base case. It can be used as a multiplier to upscale permeability from pore scale to core scale in reservoir simulations.

3.3.1 Effect of heterogeneity

We first investigated the impact of matrix heterogeneity without the presence of fractures or vugs on the effective permeability of the core sample using the finite-element based model. The principle of evaluation of the impact is based on the comparison with the base case that only matrix is present. The same arithmetic mean values of permeability of 600 nD and porosity of 0.06 are used in all the simulation scenarios. The core is divided into seven segments with a scaling factor varying from 0.25 to 1.75 in 0.25 increments. Figure 3-2a lists four kinds of bedding planes: (1) horizontal bedding with permeability monotonically decreasing from left to right and (2) from right to left, (3) vertical bedding with permeability monotonically decreases from top to bottom and (4) from bottom to top. Pressure curves (Figure 3-2a), as well as lnΔp_D (Fig. 2b) are plotted against the elapsed time with a designated color. It shows that if the part close to the upstream is more permeable (scenario (2)), very fast pressure decline occurs as soon as the flow begins, causing the non-linearity in the early period in Figure 3-2b, which means that the relationship between lnΔp_D and time is not linear. As time elapses, the relationships between lnΔp_D and time become linear in scenario (2) and (3) that the slopes are smaller than that in the scenario (1) which is the base case. The effective permeability ratios are 0.67 and 0.73 for scenarios (2) and (3), respectively, indicating the flow capacity is hampered (Table B1). Downstream curves in the two horizontal bedding scenarios almost overlap, indicating that the downstream pressure response is not sensitive to the horizontal bedding sequence as long as the mean value of permeability and porosity are the same. In contrast, if the bedding planes are horizontal, the pressure curves behave almost the same as the base case that the effective permeability ratio is 1.03 (Table B1), indicating that the flow capacity of the porous media is negligibly affected. It shows in Table B1 that vertical bedding (Hetero V) reduces the flow capacity while horizontal bedding (Hetero H) increases the flow capacity negligibly. Our simulation result is consistent with the laboratory observation by Bhandari et al. (2015) that they found the horizontal-bedding in Barnett shale is more permeable than the vertical bedding one. It has been believed that anisotropy exists in sedimentary rocks that the horizontal permeability is larger than the vertical permeability because of the overburden pressure and the vertical permeability decreases as the depth increases (Figure 3-3). In this work, we assume the matrix is isotropic in each segment, which means that the vertical permeability equals the horizontal permeability in all the segments composing the core plug, and evaluate the effective permeability as a whole. The results indicate that even when there is no anisotropy present in all the segments, effective permeability in the vertical direction is still smaller than that in the horizontal direction during the transient flow process.

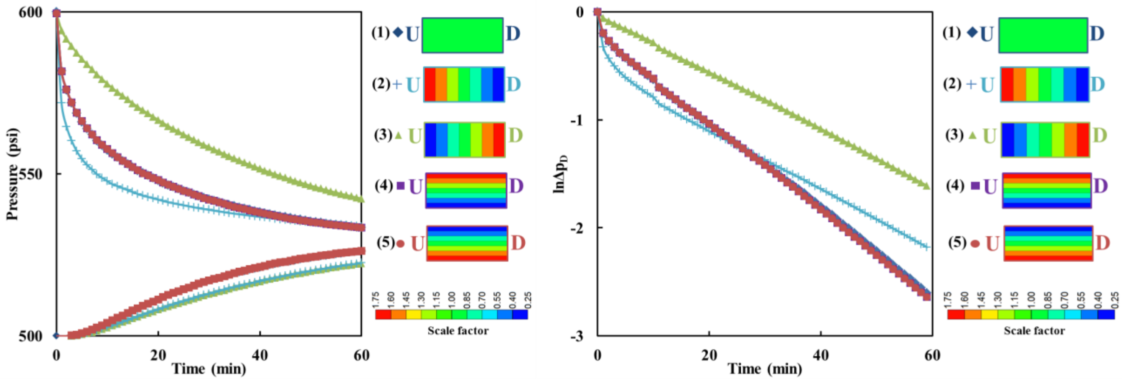

(a) (b)

Figure 3-2 Results of heterogeneous scenarios (1) base case, (2) vertical bedding with permeability/porosity decreasing monotonically from left to right (vertical isotropy), (3) vertical bedding with permeability/porosity increasing monotonically from left to right (vertical isotropy), (4) horizontal bedding with permeability/porosity decreasing from top to bottom (transverse isotropy), and (5) horizontal bedding with permeability/porosity increasing from top to bottom (transverse isotropy): (a) upstream and downstream pressure profiles; (b) natural logarithmic of the dimensionless pressure difference.

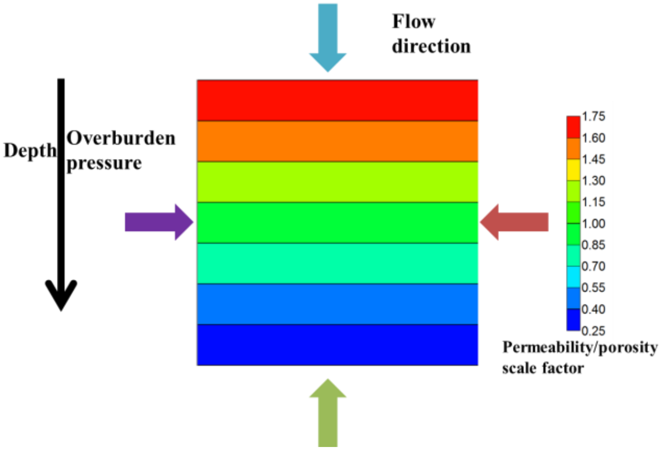

Figure 3-3 Flow process in four directions in a formation with increasing depth.

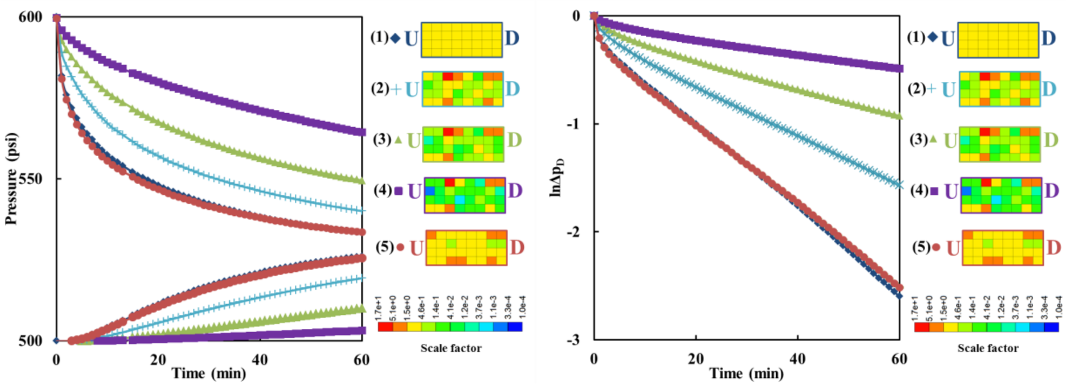

(a) (b)

Figure 3-4 Results of heterogeneous scenarios (1) base case, (2)) V_{dp} = 0.39 with grids uncorrelated, (3) V_{dp} = 0.53 with grids uncorrelated, (4) V_{dp} = 0.69 with grids uncorrelated, and (5) V_{dp} = 0.39 with correlation length of three girds in x and y directions: (a) upstream and downstream pressure profiles; (b) natural logrithmatic of the dimensionless pressure difference.

Figure 3-4a lists four scenarios with different heterogeneity. There are 8 grids in the x-direction and 4 grids in the y-direction. The Dykstra–Parsons Coefficient (V_{dp}) is used to evaluate the extent of heterogeneity, which is defined as:

$$V_{dp} = \frac{k_{50} - k_{84.1}}{k_{50}} \tag{3-12}$$

where k_{50} is the median and $k_{84.1}$ is the value with one standard deviation away from the median. Values of V_{dp} are 0.39, 0.53, 0.69, and 0.39 in scenarios (2), (3), (4) and (5), respectively. We constructed the conceptual models based on that V_{dp} ranges from 0.4 to 0.9 in most reservoirs.[103] Correlation length in scenarios from (2) to (4) is one grid size, meaning that each grid is uncorrelated. Correlation length in scenario (5) is 3 times of grid size in both x and y directions, meaning that permeability and porosity in adjacent 3 grids are correlated. Table B1 shows that heterogeneity increases flow resistance and the effective permeability ratio decreases from 0.6 to 0.18 as V_{dp} increases from 0.39 to 0.69. This trend is not difficult to understand because as the heterogeneity of the porous media increases, the energy dissipation occurring during the convective gas flow through adjacent pores increases. However, if the correlation length increases, the negative impact of heterogeneity on flow capacity can be much relieved: the effective permeability ratio is 0.95 in scenario (5) that only 5% of the flow capacity is lost: such observation reveals that the porous media behaves more like homogeneous despite the same V_{dp} with scenario (1). The reason is that kinetic energy dissipation occurs as fluid flows through heterogeneous porous media. The higher the degree of the heterogeneity, the larger the kinetic energy dissipation.[11, 104] As correlation length increases, the area of patches with similar properties increases, the chance of large differences of permeability and porosity between adjacent pores is reduced, leading to the reduced energy dissipation between adjacent pores. Thus the flow is more like in the homogeneous porous media.

3.3.2 Effect of fractures and vugs

Vugs are classified as the secondary dissolution pore types in carbonate reservoirs.[105] The size of vugs is usually noticeable by naked eyes. They are usually formed during the sedimentation and the later diagenetic process.[106] Vug, fracture, and cavity constitute secondary porosity of carbonate reservoirs.[107] The size of vug is smaller than the cavity. Vugs can be accessible or inaccessible depending on whether they are intersected with fractures; they greatly enhance the storage capacity of the porous media. In order to conduct upscaling for reservoir simulation purposes, it is necessary to characterize the contribution of vugs to the flow capacity of porous media as well. A flow simulation study with total 88 vugs by Kurtzman et al. shows that the number of vugs is positively correlated with air permeability of core plugs, and it can be used as an indicator of fracture connectivity.[105] We follow this conclusion that the number of vugs increases as fracture density increases and design a workflow to investigate the effect of vug on flow behavior: first, fractures are included in the matrix with different locations, width, orientations and lengths; second, different amount of vugs with the same dimension are included in the matrix; third, both fractures and vugs are included in the matrix.

Figure 3-5 shows five scenarios of fractured cores: (1) base case, (2) fracture located at the second half, (3) fracture located at the first half, (4) fracture penetrating the core with the width of 0.001 cm, (5) fracture penetrating the core with the width of 0.01 cm and (6) fracture penetrating the core with the width of 0.1 cm. Pressure profiles of scenarios (2) and (3) indicate that faster pressure decline occurs if the fracture is located at the first half, leading the larger s value and larger effective permeability ratio compared with the base case: the effective permeability ratios increase to 1.41 and 1.48, respectively (Table B1). Downstream pressures in scenarios (2) and (3) stay the same, which is consistent with the results in Figure 3-2, implying that downstream pressure is much less sensitive than the upstream pressure to the core-scale heterogeneity. While the fracture penetrates the whole length of the core sample, pressure responses become much faster, even the width of the fracture reduces to 0.001 cm in scenario (4). The slope in the semi-log plot of Figure 3-5b also behaves highly non-linear; after pressure equilibrium, large fluctuation of the slope appears caused by numerical dispersion because the upstream and downstream pressures are very close. As the fracture width increases to 0.01 cm in scenario (5), a dual-porosity indication, the double porosity region is formed that upstream and downstream pressure curves first converge then reach final equilibrium. The take-home message by comparing scenarios (4) and (5) is that there exists a “threshold value” of the fracture permeability that the double porosity region begins to form. The “first convergence” time is earlier with a wider fracture: it is about 0.3 min and 0.03 min for scenarios (5) and (6), respectively. This phenomenon is caused by the fact that gas flows faster in the fracture than in the matrix so that high-pressure gas in the fracture arrives in the downstream earlier than that in the matrix. Therefore, a part of high-pressure gas flows back to the matrix from the downstream. Figure 3-6 depicts pressure distribution profiles in scenario (6) at the time of 10 seconds, 50 seconds, 100 seconds and 300 seconds. It clearly shows that upstream and downstream reservoirs are first connected by the fracture, and the pressure is lower in regions away from the reservoirs and the fracture. As time goes on, the pressure was transmitted in the matrix; pressure gradient gradually reduces and completely diminishes at about 5 min. This finding reveals that, as long as the fracture, or the preferential flow path, does not run through the total length of the core, the double porosity region will not be formed. The formation of the double porosity region significantly accelerates the flow capacity of the porous media even when the width of the fracture is very small.

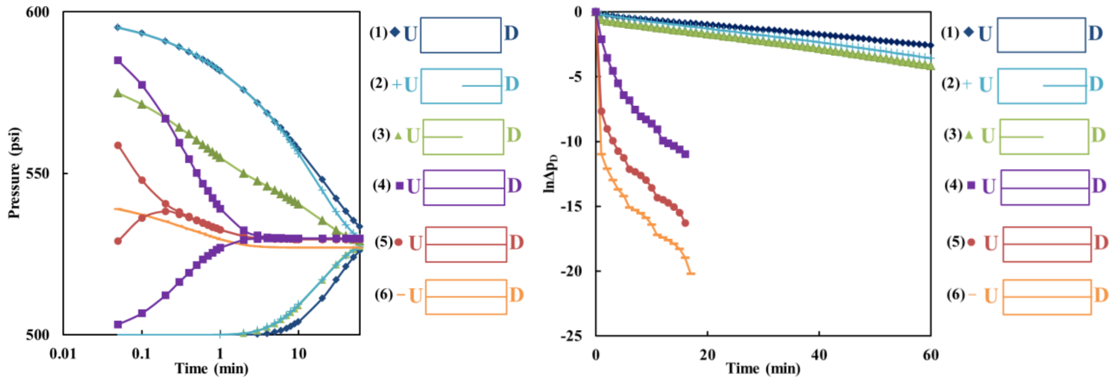

(a) (b)

Figure 3-5 Results of fractured scenarios with fracture (1) base case, (2) located at the second half, (3) located at the first half, (4) penetrating the core with the width of 0.001 cm, (5) width of 0.01 cm, and (6) width of 0.1 cm: (a) upstream and downstream pressure profiles; (b) natural logarithmic of the dimensionless pressure difference.

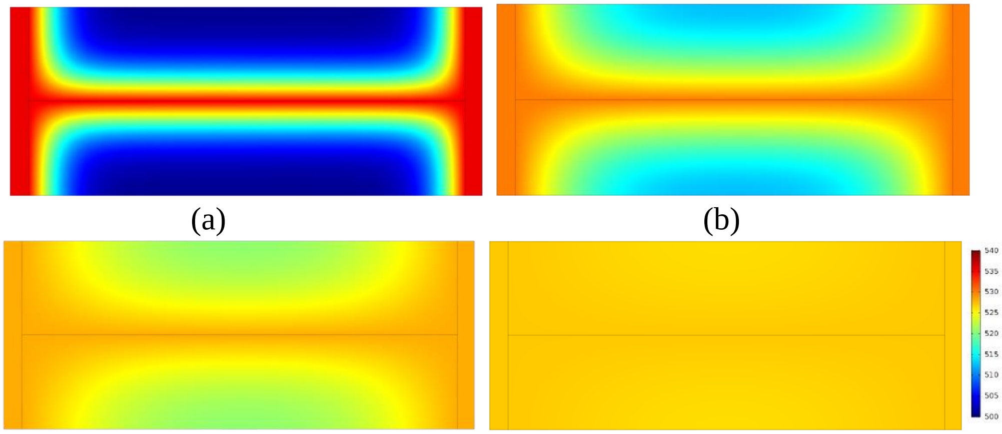

(a) (b)

(c) (d)

Figure 3-6 Pressure distributions (in psi) at different stages of scenario (6) of Fig. 5: (a) 10 seconds; (b) 50 seconds; (c): 100 seconds; and (d): 300 seconds.

Figure 3-7 shows five fractured scenarios with 8 pairs of intersecting fractures (with each fracture length of 0.5 cm). Orientation angles are set to vary from 15° to 75° in an increment of 15° for scenarios (2) to (6). It shows from Table B1 that the effective permeability does not change much as the orientation changes from 15° to 30° but decreases step by step from 30° to 75°. The effective permeability ratio with 75° becomes 1.01, indicating that fractures no longer contribute to the enhancement of the flow capacity, even though they increase the apparent porosity to 6.6% as seen by the lower equilibrium pressure than that in the base case.

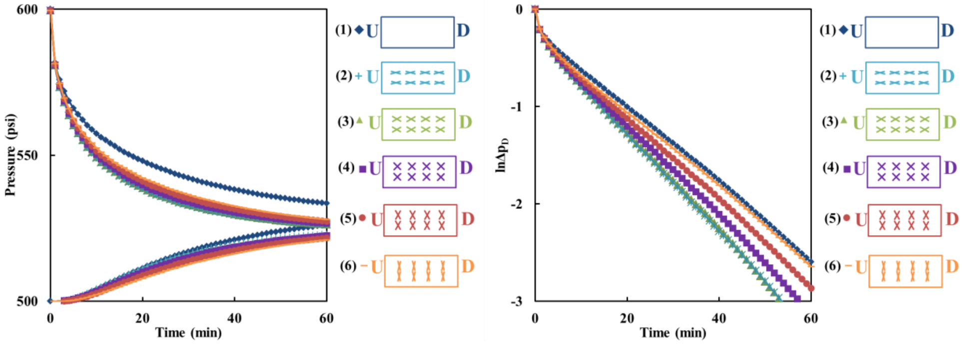

(a) (b)

Figure 3-7 Results of fractured scenarios with 8 pairs of 0.5-cm fractures (1) base case, (2) orientation degree of 15° , (3) 30° (4) 45°, (5) 60°, and (6) 75°: (a) Upstream and downstream pressure profiles; (b) natural logarithmic of the dimensionless pressure difference.

Figure 3-8 shows scenarios of fractured cores with a series of fracture length (with fracture orientation angle of 45°). The length increases from 0.5 cm to 1.3 cm in an increment of 0.2 cm for scenarios (2) to (6). These pairs of fractures begin to intersect with each other when the fracture length increases to 0.9 cm (scenario 5) that 8 intersection points are present. No more intersection points increase in scenario (6), though two adjacent pairs' parallel fractures are pretty close. In scenario (6) the intersection points number increases to 20. It shows from Table B1 that the effective permeability ratio increases exponentially with the fracture length increases, indicating that the development of the fracture network is crucial to improving the flow capacity of low-permeability reservoirs.

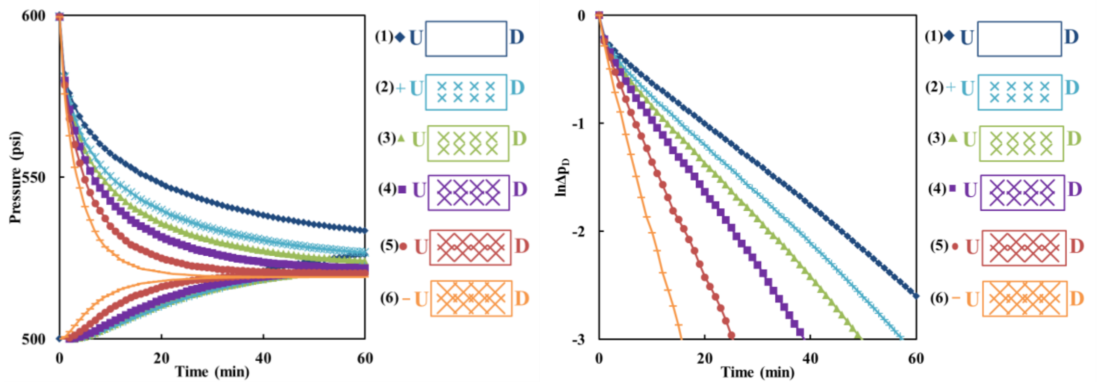

(a) (b)

Figure 3-8 Results of fractured scenarios with different fracture length (1) base case, (2) 0.5 cm, (3) 0.7 cm, (4) 0.9 cm, (5) 1.1 cm and (6) 1.3 cm: (a) Upstream and downstream pressure profiles; (b) natural logarithmic of the dimensionless pressure difference.

Figure 3-9 shows scenarios with different numbers of vugs with the same diameter of 0.1 cm. The permeability of vugs are set to be 10 Darcy and porosity is set to be unity. As the number of vugs increases from 3 to 35, the apparent porosity increases from 6.09% to 7.04% which are calculated based on the summation of matrix pore volume and the void volumes in fractures and vugs, demonstrating that vugs provide an important extra storage source. However, based on the analysis of the pressure profiles, it is observed that these scenarios deviate negligibly from the base case and the effective permeability ratio only deviates by 2% at the most from the base case, demonstrating that, if vugs are isolated they do not affect flow capacity of the porous media. This observation is consistent with the flow simulation results by Wu that vugs have negligible impacts on the flow behavior if they are not acting like joints connecting small fractures and large fractures when they only act as extra storage locations inside the matrix.[108]

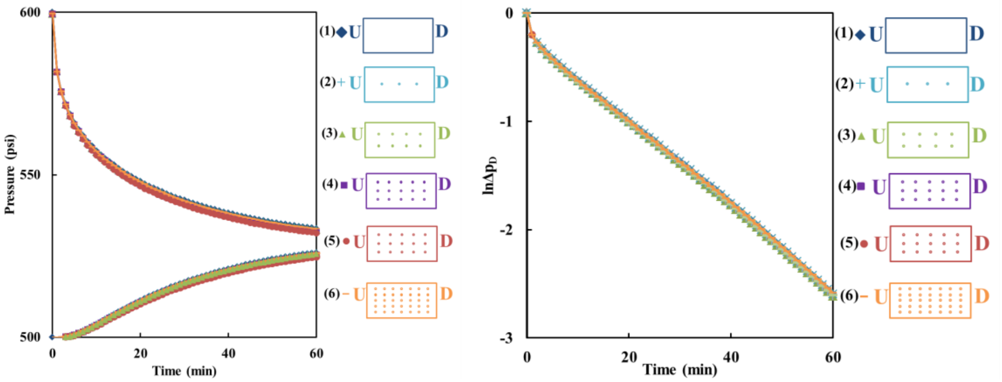

(a) (b)

Figure 3-9 Results of vuggy scenarios with vug number of (1) 0, (2) 3, (3) 8, (4) 15, (5) 24 and (6) 35: (a) Upstream and downstream pressure profiles; (b) natural logarithmic of the dimensionless pressure difference.

Wu also showed that the connection of vugs with fractures plays an important role in affecting the flow behavior from a triple-porosity model consisting of vug, fracture, and matrix.[108] As inspired by the fact that in certain cases, the number of vugs is correlated to the fracture density. Hence, the number of vugs are set to be 3, 8, 15, 24, 35 when fracture lengths are 0.5 cm, 0.7 cm, 0.9 cm, 1.1 cm and 1.3 cm, respectively, from scenarios (2) to (6) in Figure 3-10. As the diameter of vug is 0.1 cm which is the same the width of the fracture, vugs in line with the fractures increase the apparent fracture porosity because vugs' porosity is unity. Effective permeability with pure fracture and fracture-vug systems are plotted in Figure 3-11. In scenarios (2), (3) and (5), the effective permeability does not differ much from the two cases, which is because vugs are either located at the intersection of two crossed fractures or ending point of fractures. Only vugs in scenario (5) increase the effective permeability ratio from 2.89 to 3.67, which is significant. The increase is contributed by the vugs that connect two adjacent fracture networks. Figure 3-12a and

Figure 3-12b show pressure distributions at 10 minutes for scenarios (5) in Figure 3-8 and Figure 3-10, respectively. Figure 3-12a shows six distinguishable regions with pressure distributions. The matrix between two adjacent regions acts as a flow barrier that inhibits the continuous pressure propagation. In Figure 3-12a we can see several distinguishable regions are present because the fractures are not connected. In Figure 3-12b we can see that these regions are connected because vugs connect adjacent fractures. Therefore, the flow capacity of the system is greatly enhanced. In comparison, it is observed in Figure 3-12c and Figure 3-12d representing scenarios (6) in Figure 3-8 and Figure 3-10, that without the embedded vugs the fracture network has already been well connected, thus the flow behavior does not change much. To examine the locations of vugs on the flow behavior in the fractured core, we purposely placed vugs not along with the fractures as shown in Figure 3-13. Figure 3-14 shows the pressure and the natural logarithmic of the dimensionless pressure difference in comparison to the scenario (6) in Figure 3-10. It is observed that if the vugs are distributed outside the fractures, the dimensionless pressure decline rate is 3.98 1/min, which is even smaller than that in the scenario with only fractures, which is 4.07 1/min (Table B1). These results further prove that vugs do not increase the flow capacity unless they become the joint of connecting fractures.

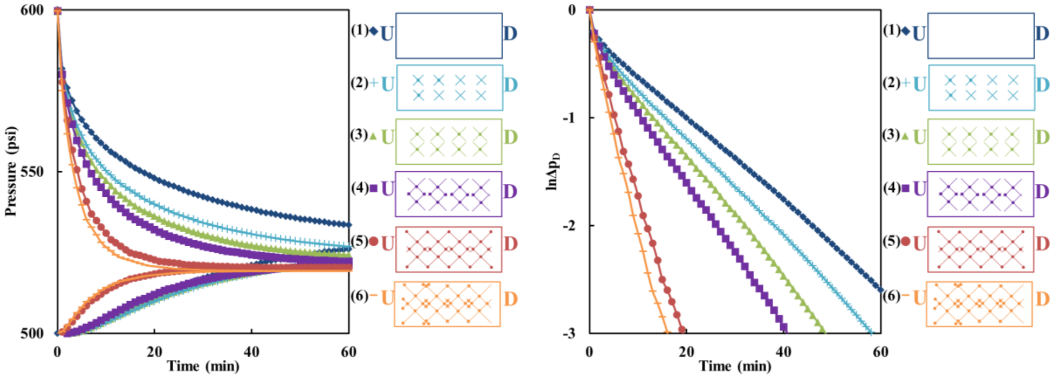

(a) (b)

Figure 3-10 Results of fractured and vuggy scenarios (1) base case, (2) 0.5 cm-fracture with 3 vugs, (3) 0.7-cm fracture with 8 vugs , (4) 0.9 cm-fracture with15 vugs, (5) 1.1-cm fracture with 24 vugs, and (6) 1.3-cm fracture with 35 vugs: (a) upstream and downstream pressure profiles; (b) natural logarithmic of the dimensionless pressure difference.

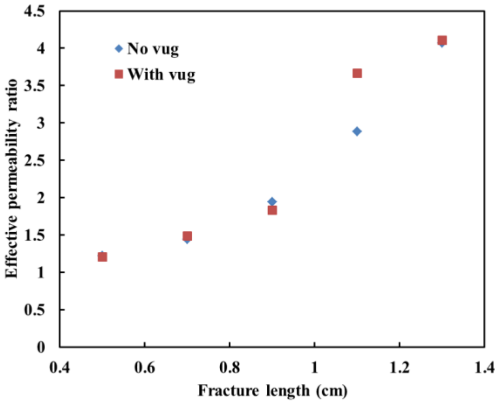

Figure 3-11 Effective permeability ratios of fractured cores with and without vugs.

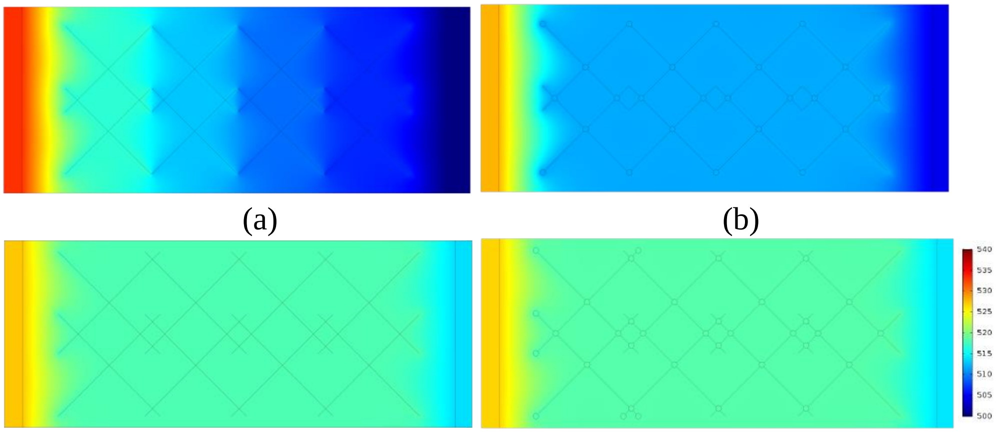

(a) (b)

(c) (d)

Figure 3-12 Pressure distribution profiles (with unit of psi) at 10 mins for fractured cores: (a) 1.1-cm fracture without vug (scenario (5) in Fig. 8); (b) 1.1-cm fracture with vug (scenario (5) in Fig. 10); (c) 1.3-cm fracture without vug (scenario (6) in Fig. 8); (d) 1.3-cm fracture with vug (scenario (6) in Fig. 10).

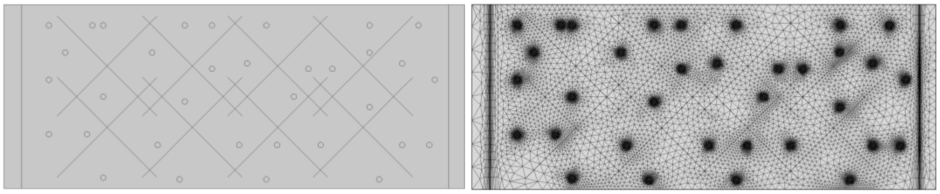

(a) (b)

Figure 3-13 Simulation scenario with vugs distributed randomly and not along the fractures: (a) locations of vugs and fractures; (b) grid settings of the system.

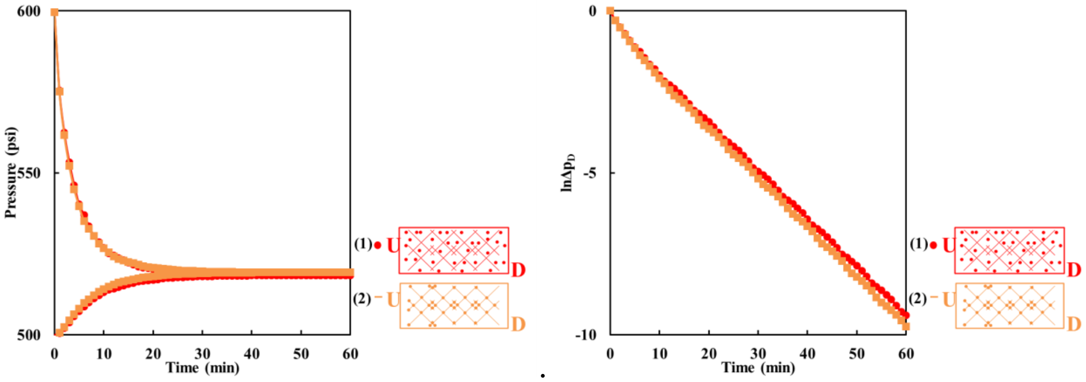

(a) (b)

Figure 3-14 Results of vuggy and fractured scenarios that (1) vugs distributed randomly and outside fractures (2) vugs distributed along fractures : (a) upstream and downstream pressure profiles; (b) natural logarithmic of the dimensionless pressure difference.

3.3.3 Comparison of transient and steady-state method

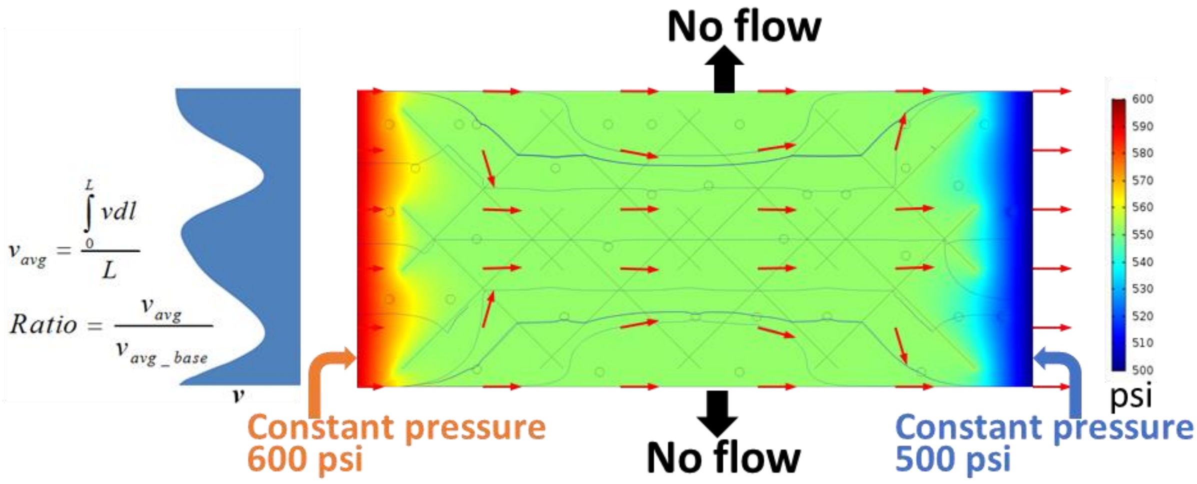

Figure 3-15 Schematic of estimating effective permeability ratio by the steady-state method. The red arrows indicate flow velocity directions and blue lines indicate streamlines, generated by the simulator.

Figure 3-15 shows the schematic of estimating effective permeability ratio based on the steady-state method. We exert constant boundary pressures of 600 psi and 500 psi on the left and right edges of the core sample, respectively, and no flow boundary condition on the lower and upper edges. After the fluid flow reaches a steady state, we plot the velocity along the length of the left edge. The average velocity, v_{avg}, is estimated as the ratio of the integration of velocity over the edge length. The veclocity can be integrated over the edge length directly because velocity is normal to the edge length at the left and right boundaries, as could be observed from the flow velocity directions and streamlines in Figure 3-15. According to Darcy's law, the effective permeability ratio is equivalent to the average velocity ratio.

Based on this methodology, we re-evaluated effective permeability ratios by the steady-state method of all the 34 scenarios, recorded the results in Table B1, and compared with the transient method in Fig. 16.

Overall, we can see that ratios from the steady-state method are consistent with that from the transient method. We divide the data points into six zones. In the heterogeneous zone, we can see the steady-state method is independent of flow directions when vertical heterogeneity is present in the core. In the single fracture zone, the ratio of the first-half fracture scenario (#11) by the steady-state method is only 0.05, which is inaccurate. The reason is that the fracture is connected with left edge directly, gas flows preferentially into the fracture first. The fracture acts like additional boundaries of the model where the fluid flows into. Thus, velocity integration only on the left edge cannot be used to estimate the effective permeability properly. We can also see that the results of three scenarios with different fracture widths (#12-#14) are the same, and very close to unity. The reason is similar to that for scenario#11. The fracture separates the core into two halves that it does not contribute to the flow capacity during the steady-state flow. However, in Figure 3-5 significant discrepancies are observed between different single-fracture scenarios during the transient flow process that the steady-state method cannot reveal. In the fracture angle zone, we can see that the results of the steady-state method are similar with that of the transient method: the 15° and 30° scenarios are very close, and there is a steady decrease when angle varies from 30° to 75°. In the fracture length zone, there is no obvious difference between the steady-state method and the transient method when fracture length is 0.7 cm and 0.9 cm, and the difference increases when the fracture length is 1.1 cm and 1.3 cm as the flow in fracture dominates. In the vug zone, the results of the steady-state and transient method are similar as the contribution of vugs to the flow capacity is negligible. In the fracture and vug zone, the difference between the two methods increases when fracture length increases. In summary, the steady-state method does not depict the transient flow behavior when the core sample is heterogeneous, and the discrepancy between the steady-state and transient methods becomes larger when the fracture length is longer.

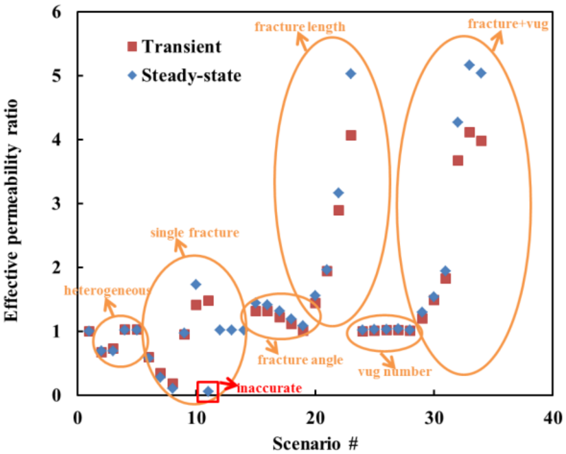

Figure 3-16 Effective permeability ratios based on the transient and steady-state methods for the total 34 scenarios.

3.4 Experimental study and history match of gas transient transmission test in the fractured core

In this section, we present the results of pulse-decay experiments on one fractured core sample. The pore pressure varies approximately from 200 psi to 800 psi, and the effective stress from 1,000 psi to 3,000 psi. History matching by CMOST was performed for each pulse-decay experiment to obtain the properties of the matrix and the fracture.[109] Using the collected data, we explored the dependency of porosity and permeability of both matrix and fracture on pore pressure and effective stress, and the fitness of curve matching with pore pressure.

In a typical pulse-decay laboratory test, two factors are likely affecting the flow in the fracture. First, it is the small temperature fluctuation caused by the Joule–Thomson effect occurring near the inlet when gas expands from the first upstream reservoir to the second upstream reservoirs. Joule–Thomson effect is more significant for carbon dioxide than natural gas or air.[110] In this work, helium is used as the flowing fluid attempting to minimizing this effect. Second, it is the manual opening of the valve that can hardly be 100% identical. In our experiment, we use the HIP valve that contains a tapered pin into the inner open space. We controlled the constant volume of the open space in the valve by opening the valve two circles every time and always tried to open steadily. However, the opening speed and the opening degree cannot be controlled in perfect accords by manual operations that likely create some uncertainty in fracture flow behavior.

Generally, there are two approaches to set properties of the fracture as tunable variables. One is setting fracture width as a variable assuming the fracture porosity is 100%; the other one is setting fracture porosity as a variable assuming the fracture width is constant. In this work, we choose the second approach by setting the fracture in the middle with the width of 0.07 cm. Schematic of the model set-up including the upstream reservoir, the core and downstream reservoir are shown in Figure 3-17. The size of the grid decreases as it is closer to the fracture to capture the interaction between the fracture and matrix properly.

The core used in this study is classified as carbonate-rich shale. It is 3.09 inches long with the diameter of 1.50 inches (Figure 3-17a). Its color is grey to light grey, with observable lamination but not along the entire length; some tiny cherts are present; longitudinal fracture is observed along the entire length splitting into smaller fractures, and other microfractures are visible as well. The numerical model is constructed with one fracture located in the middle of the core, though multiple fractures are observed at different heights with a major one located in the middle; this simplification should not affect the effective permeability because based on our previous conclusion in Fig. 2 that the effective permeability of the porous media is not affected by the configuration of horizontal bedding planes. It is worthy to note that with the aid of CT image, the model could be more realistically constructed rather than using the idealized fracture pattern.

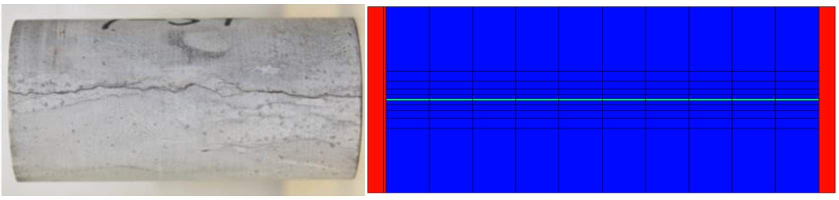
(a) (b)

Figure 3-17 (a) Fractured core; (b) grid settings of the core: the red represents upstream and downstream reservoirs, the green represents the fracture and the blue represents the matrix.

In section 3.3 as discussed previously, we constructed finite-element models in two dimensions to estimate effective permeability in the presence of fractures and matrix. In this section, we used the black oil simulator, IMEX in CMG software suite,[111] to simulate experiments in three dimensions based on the core size and the reservoirs after checking the result consistency between COMSOL and IMEX. Subsequently, we applied CMOST, which is another package in CMG software suite, to history match the experimental pressure curves by setting porosity and permeability of the matrix and the fracture to be tunable parameters in CMOST. Compressibility factor, density, and viscosity of helium from REFPROP are used as pressure-dependent parameters in the flow equations of the simulator.[112]

Effective stress is increased from 1,000 psi to 3,000 psi and kept constant for a series of experiments with varying pore pressure. Pore pressure increases continuously with a pressure pulse of approximately 100 psi. In the numerical model, the permeability of the upstream and downstream reservoirs is set to be 2D and the porosity is unity. Porosity and permeability of the matrix and the fracture are set to be tunable parameters to history match the experimental pressure curves in CMOST (Table 3-1). Total of 500 experiments are performed in CMOST for each set of laboratory data including the upstream and downstream pressure profiles. The case with the lowest global matching error (GME) is regarded as the optimal. History matching error is calculated as the relative error between the experimental data and the simulation data:

$$Q_i = \frac{1}{\sum_{j=1}^{N(i)} tw_{i,j}} \times \sum_{j=1}^{N(i)} \frac{\sqrt{\frac{\sum_{t=1}^{T(i,j)} (Y_{i,j,t}^{s} - Y_{i,j,t}^{s})^2}{NT(i,j)}}}{Scale_{i,j}} \times 100\% \times tw_{i,j} \tag{3-13}$$

where *i* denotes well (or sector) number, *j* denotes production type, *t* denotes time, *N(i)* is the number of production types for well *i*, *NT(i, j)* is the number of data points, $Y^{s}_{i,j,t}$ is the simulated data, $Y^{m}_{i,j,t}$ is the measured data, $tw_{i,j}$ is the term weight, and $Scale_{i,j}$ is the normalization scale. In our history matching process, there are two sectors (upstream and downstream grid blocks), one production type (grid pressure), 600 data points (600 seconds with one pressure data per second), and the term weight is one. The normalization method is set to be default, which means that the Method#1 is applied, further details of this method can consult the manual of CMOST.[109]

The GME is evaluated as:

$$GME = \frac{\sum LME_i w_i}{\sum w_i} \tag{3-14}$$

where *i* also denotes the well (or sector) number, LME represents local history matching error (for each sector), and w_i is weight, which is one for both sectors.

All the history matching results are from the optimal cases with least matching errors based on 500 simulation experiments that the GMEs are all below 0.2% during the first run.

Table 3-1 Range of properties of matrix and fracture during the history matching.

	Matrix	Fracture
Permeability (mD)	1E-5 - 1E-2	10 - 2000
Porosity (fraction)	1E-2 -1E-1	0.3 - 0.7

Fracture porsity discussed in this chapter is in the single-porosity system, which is different from that disccused in Chapter 5 where it is defined in a dual-permeaiblity system. Fracture porosity is not unity because of the surface roughness; it is defined as the ratio between void volume (V_{void}) and the total volume, as illustrated in Figure 3-18.[113]

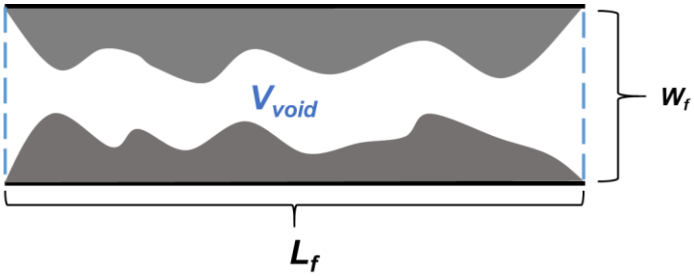

Figure 3-18. Fracture porosity casued by roughness on the surface.[113]

Based on Figure 3-18, fracture porosity is defined as:

$$\phi_f = \frac{V_{void}}{w_f L_f} \tag{3-15}$$

where L_f is the fracture length.

Figure B2 to Figure B4 demonstrate the full pressure profiles measured in the laboratory (black dot lines) and the fitted pressure profiles (solid blue lines) with the effective stress of 1,000 psi, 2,000 psi, and 3,000 psi, respectively; A total of 18, 22, 19 experiments were performed under the effective stress of 1,000 psi, 2,000 psi, and 3,000 psi, respectively (see Appendix B). We started a new experiment as soon as the pressure in the previous experiment reached equilibrium. Thus we covered the whole pressure range from the initial pressure to the final pressure. The pressure profiles all show a double porosity region before they reach the final equal equilibrium pressure. Before the convergence of upstream and downstream pressures, the fracture flow dominates in the fracture, and then matrix flow and matrix-fracture flow dominates. Pressure data points were recorded at one per second. In all the figures, the 3rd data points (at 2 sec) are in the double porosity region; the 4th data points (at 3 sec) begin to fall in the black-dot data group in the semi-log plot.

The second data points (at 1 sec) from upstream and downstream, which are the most influenced by the early fracture flow, are marked with red to more clearly observe their variations. Qualitatively, the closer the second point (red) to the other data points, the faster the flow in the fracture. It shows in Figure B2, Figure B3, and Figure B4 that locations of second data points do not have relationships with the pore pressure or the effective stress. The direct impact of this inconsistency is the variation of estimated fracture volume. Figure 3-19 depicts the ratio of fracture volume over the total void volume in the core. It indicates that the storage capacity in the matrix is the dominant and the ratios have significant standard deviations. This inconsistency implies that the permeability in the fracture might also be inconsistent with pressure. We propose several reasons for the uncertain flow behaviors in the fracture. First, the artifacts stated previously might alter the flow path from experiment to experiment which contributes to the irregular behaviors of the fracture volume and flow. Figure 3-17 shows that multiple microfractures with one main fracture are present in the core sample. The fracture network can provide different flow paths for the gas flows through. Second, the high-velocity flow causes the inertia effect which is inherently unpredictable even excluding the human errors. Third, because the fracture volume is much less than the pore volume in the matrix, slight deviation of the pressure points in the double porosity region would cause a significant deviation of the fracture volume and permeability; therefore, if fracture volume percentage in the total porosity of the core is higher, more consistent result from a series of pulse-decay experiments can be expected. Fourth, not knowing the exact width of the fracture might also be an uncertain factor toward interpreting the pressure curves that a proper selection of value is difficult to determine because of the complex fracture network present in the core. Fifth, the core applied in this study is very hard that the fracture compaction induced by the effective stress is negligible.

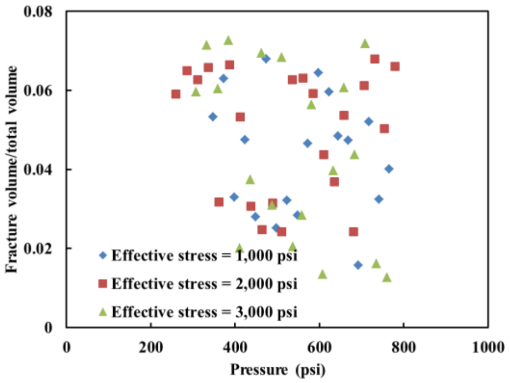

Figure 3-19 Ratios of fracture volume over pore volume as functions of effective stress and pressure, summarizing all the experiments.

Quantitative results of permeability/porosity of the matrix and fracture are demonstrated in Figure 3-20. It shows that the effects of effective stress and pore pressure on matrix permeability are clearly demonstrated, though not as consistent as experiments carried out on pure matrix. Permeability in the fracture and matrix has the difference of six orders of magnitude. The apparent permeability as a function of reciprocal of pore pressure is plotted in Figure 3-20a, and the first-order Klinkenberg equation is applied to fit the data points. k_{app} is the apparent permeability taking into account of both Darcy flow and slip flow,[81, 114, 115] and k_{∞} is the intrinsic permeability. Figure 3-20b shows that the matrix porosity decreases noticeably as the effective stress increases from 1,000 psi to 2,000 psi, whereas a continued decrease is not observed as the effective stress increases to 3,000 psi. This finding implies that the core sample studied is very hard, and matrix permeability is more sensitive to the effective stress than the matrix porosity. It is because the volume of the pore throat is only a small percentage of the total pore volume compared with the pore body. Although the pore volume is reduced negligibly by the effective stress, the suppression on the pore throats may have a rather profound effect on reducing the permeability.

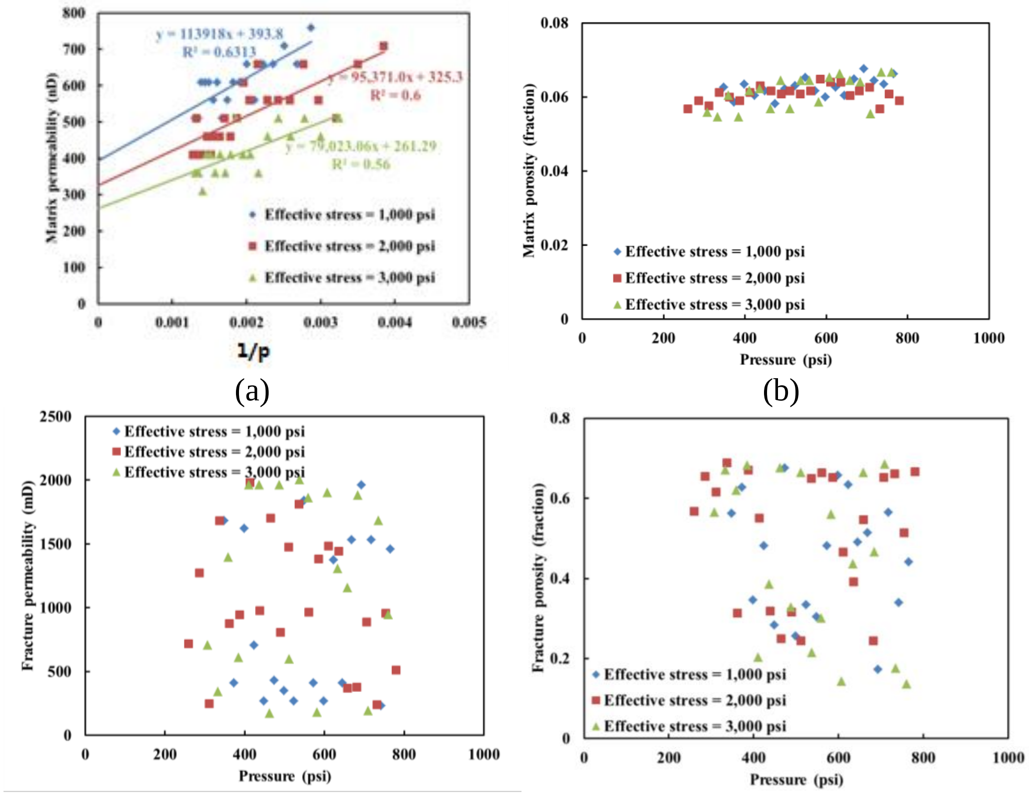

(a) (b)

(c) (d)

Figure 3-20 Estimated properties of matrix and fracture under different effective stress: (a) matrix permeability; (b) matrix porosity; (c) fracture permeability; and (d) fracture porosity.

The ratio of the slip flow over the Darcy flow based on Figure 3-20a is plotted in Figure 3-21. We can see that the slip flow is more important under low pressure that outweighs the Darcy flow starting from about 300 psi when the ratio is higher than unity. We can also see that slip flow is more important under higher effective stress. Because the intrinsic permeability of the porous media is proportional to the square of the pore diameter, this fact implies that in tight or shale reservoirs with nanometer-scale pore radius, the contribution of slip flow is more important for low-pressure gas when the effective stress causes the reduction of pore radius.

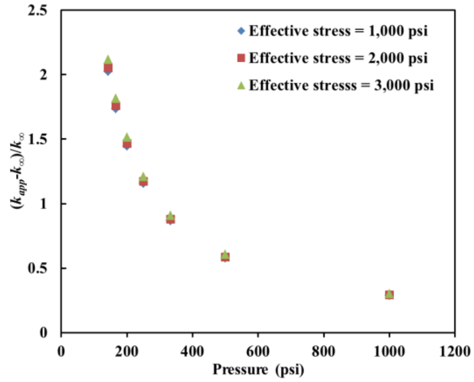

Figure 3-21 Ratio of slip flow over Darcy flow as functions of effective stress and pore pressure.

Figure 3-22a shows GME of all the history matching results. We used the same criteria for every history matching process, including ranges of parameters to be matched (Table 3-1), and the same number of experiments which is 500. Therefore, the results can reveal relationships between the matched parameters and pressure. Figure 3-20 shows that the GME reduces as the pore pressure increases. This finding indicates that the heterogeneity character of the core is revealed more obviously under low pressure than under high pressure. We performed an uncertainty and consistency study for the 2,000 psi effective stress experiments by re-running the history matching process. The 1st and 2nd matching results plotted in Figure 3-22b shows that the matching results are consistent and repeatable. Kamath et al. showed through theories and experiments that when using upstream and downstream reservoirs with much larger volume than the pore volume of the core,[83] the heterogeneous character of the core sample may not be revealed. Core heterogeneity is one source of difficulties perfectly matching the pressures curves, i.e., GME approaches zero. It shows in this study that heterogeneity of the core is revealed less obviously under high pressure than low pressure.

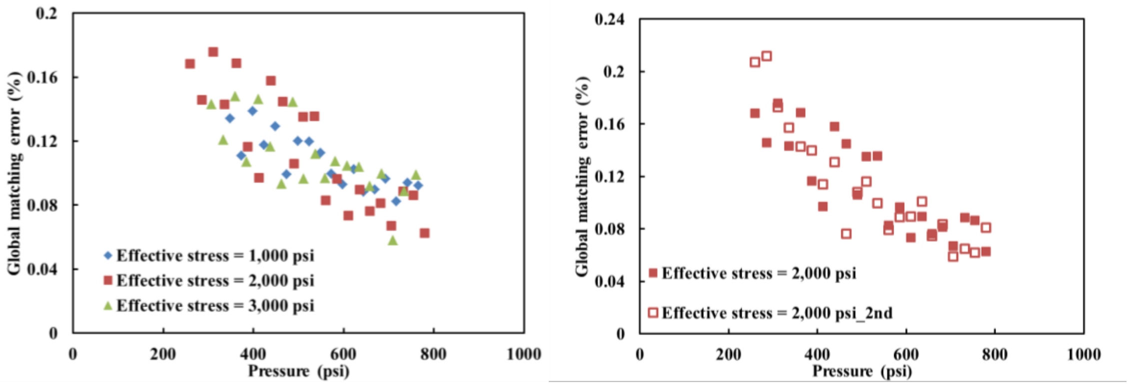

(a) (b)

Figure 3-22 (a) Global matching error under different effective stress, and (b) 1st and 2nd history matching results for the 2,000 psi effective stress experiments.

To evaluate the effect of heterogeneity on the history matching process, subsequently, we divide the core into 2 and 5 segments longitudinally to repeat the matching result, where permeability and porosity values for matrix/fracture for each segment are set individually.

Table 3-2 shows the matching results with different segments. We can see that as the number of divided segments increases, the GME reduces indicating a better curve fitting is obtained. It is worthy to note that the combination of properties with multiple segments fitting the pressure curves are not unique, and it may not imply the real property distributions. Nevertheless, we can infer from the results that heterogeneity is one cause of difficulties not perfectly fitting the upstream and downstream pressures simultaneously. From Table 3-2 we can also see the mean value of matrix porosity in the three settings are the same, 0.06. However, the fracture porosity differs from 0.35 (1-segment) to 0.55 (2-segment), whereas the 1-segment fitting line is only slightly different from that of the 2-segment (Figure 3-23), supporting the previously proposed reason that the small percentage of fracture volume to the total void volume (<8%) is an important factor causing the nonunique fracture properties.

Table 3-2 GME and matched properties with different segments.

Number of segments	1	2		5				
GME (%)	0.14	0.08		0.07				
Matrix porosity (fraction)	0.06	0.04	0.08	0.02	0.05	0.09	0.08	0.06
Matrix permeability (nD)	709.30	1608.40	509.50	6453.55	59.95	4255.75	809.20	209.80
Fracture porosity (fraction)	0.35	0.58	0.51	0.58	0.36	0.42	0.38	0.32
Fracture permeability (mD)	1621.90	995.05	925.40	965.20	1761.20	1920.40	487.60	975.15

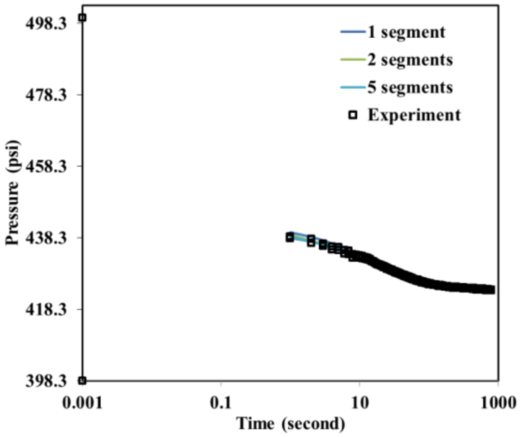

Figure 3-23 Matched pressure curves with different segments along with the experimental data. The zero-second experiment pressures are shifted to be at 0.001 second to be present on the semi-log plot.

3.5 Conclusions

In this work, we experimentally and numerically investigated transient gas transmission experiments in one natural, heterogeneous core and one fractured core. DFM is applied to simulate the core-scale gas pulse-decay experiment. Pressure history matching was successfully applied to estimate the double porosity and double permeability properties of heterogeneous carbonate-rich shales.

The effective permeability ratio based on the transient and steady-state method from the DFM simulation show comparable consistency. The transient method can reveal transient flow behaviors of some complex core configurations that the steady-state method cannot. Heterogeneity reduces the permeability of the core. The effective permeability ratio reduces to 11% and 18% with the Dykstra–Parsons coefficient of 0.69 as determined from transient and steady state method. Correlation length is also an important parameter considering heterogeneity effect on the gas flow process. A long correlation length reduces the heterogeneity effect hampering gas flow in heterogeneous porous media. Vugs themselves have negligible effects affecting the flow behavior unless they connect fracture networks. Flow capacity in fractured and vuggy porous media is greatly enhanced because of fracture. Fracture properties, such as orientation, length, and density are all important factors influencing the permeability. Vugs alone affect the flow capacity negligibly. The effective permeability ratio increases to 1%-2% when 35 0.1-cm diameter vugs are present in the core. The flow capacity of the fractured core does not change as the fracture orientation changes from 15° to 30° and show a step-wise decrease as it increases from 45˚ to 75˚. The ratio of effective permeability can increase to 4.11 when fracture network and vugs are present in the core (scenario #33 in Table B1). A double porosity region appears in pressure curves of the simulated pulse-decay experiment if the fracture penetrates along the length of the core with the width larger than a threshold value.

Regarding experiments on the fractured core, gas first arrives at the downstream through the fracture. Thus the downstream pressure is higher than the matrix, causing the high-pressure gas in the downstream flow back to the matrix, leading to the formation of the double porosity region in the pressure curves. Our results show that slip flow is more important under lower pressure. Slip flow contributes to the flow capacity about twice as much as Darcy flow under the pressure of 200 psi. The matrix porosity is less sensitive to the effective stress than the matrix permeability because the stress affects more on the pore throat than the pore size. The GME of all the history matching results ranges from 0.04% to 0.2%. We inferred from the history matching results that heterogeneity of the core is revealed more obviously under lower pressure based on the fact that the GME shows a trend of decreasing as pore pressure increases. In contrast, the fracture does not show a consistent trend like the matrix, which is a strong indication of uncertain turbulent flow caused by the inertia effect occurs in the fracture especially under the high pressure gradient, supported by the inconsistent locations of the pressure points at the first second observed from all the experiments. The GME decreases from 0.14% to 0.07% when the segment number of the core increases from 1 to 5. Based on this fact, we inferred that heterogeneity is one reason why the pressure curves are not perfectly matched.

3.6 Nomenclature

a	Volume ratio between pore volume and the upstream reservoir volume, dimensionless
b	Volume ratio between pore volume and the downstream reservoir volume, dimensionless
c	Gas compressibility, 1/Pa
$f_b(a,b)$	Polynomial of a and b in the base case, dimensionless
$f_{eff}(a,b)$	Effective value of $f(a,b)$, dimensionless
k	Permeability, nD or mD or m^2
k_{50}	Median, nD
$k_{84.1}$	Value with one standard deviation away from the median, nD
k_∞	Intrinsic permeability, nD
k_{app}	Apparent permeability, nD
k_b	Permeability in the base case, nD
k_{eff}	Effective permeability, nD

k_f	Fracture permeability, mD
L	Core length, m o ft
LME	Local matching error, %
L_f	Fracture length, m or ft
NT	Data points number, dimensionless
P	Pressure, psi or Pa
$p_d(0)$	Initial downstream pressure, psi or Pa
$p_d(t)$	Downstream pressure at time t, psi or Pa
$p_u(0)$	Initial upstream pressure, psi or Pa
$p_u(t)$	Upstream pressure at time t, psi or Pa
Q	History matching error, %
Q_m	Accumulation term, kg/m^3-s
s	Slope of the semi-log plot, 1/s
s_{b}	Slope of the semi-log plot in the base case, 1/s
s_{eff}	Effective value of the slope of the semi-log plot, 1/s
v_{avg}	Average velocity, m/s
v_{avg_base}	Average velocity in the base case, m/s
V_d	Volume of downstream reservoir, cm^3
V_{dp}	Dykstra–Parsons coefficient, dimensionless
V_p	Pore volume, cm^3
V_u	Volume of upstream reservoir, cm^3
V_{void}	Void volume in the fracture, m^3 or ft^3
w_f	Fracture width, m or ft

Δp_d	Dimensionless pressure, dimensionless
μ	Viscosity, Pa·s
ρ	Gas density, kg/m^3
ϕ	Porosity, dimensionless
ϕ_{eff}	Effective Porosity, dimensionless
ϕ_f	Fracture Porosity, dimensionless
$\overrightarrow{u_m}$	Velocity vector, m/s
$\vec{n}$	Normal vector, dimensionless

Chapter 4: Shale gas permeability evolution during the production process (Marcellus shale example)

This chapter is a copy of the published paper “A workflow to estimate shale gas permeability variations during the production process” in *Fuel* (May 2018, 15: 879-889) with format change after purchasing the copyright through Rightslink. Elsevier holds the copyright for this chapter. This chapter should be downloaded for only personal use, and further use of the materials in this chapter should purchase the copyright from Elsevier.

4.1 Abstract

Gas flow behavior in the tight shale porous matrix is complex due to the involvement of multiple physical processes. Pore size reduces as the effective stress increases during the production process, which will reduce the intrinsic permeability of the porous media. Slip flow and pore diffusion enhance gas apparent permeability, especially under low reservoir pressure. Adsorption not only increases original gas in place (OGIP) but also influences gas flow behavior because of the pore size reduction when the molecule size is comparable with the pore size along with the induced surface diffusion. Surface diffusion between the free gas phase and adsorption phase enhances gas permeability. Pore size reduction and the adsorption layer both have complex impacts on gas apparent permeability, plus the non-Darcy flow component make shale gas permeability look mysterious. These physical processes are difficult to couple with fluid flow, and previous research is generally incomplete. This work proposes a methodology to take these various effects into account simultaneously. Our results show that the geomechanical effect significantly reduces the intrinsic permeability of shale gas. However, slip flow and pore diffusion begin to overwhelm the geomechanical effect at reservoir pressure of 500 psi and below. As for the adsorption layer, it changes little of shale gas permeability but its induced surface diffusion might

increase gas flow capacity significantly at low pressure, and the influence depends on the value of surface diffusivity. The workflow proposed in this study is considered to be useful to describe shale gas permeability evolution considering these physics together.

4.2 Introduction

Despite the rapid growth of non-fossil fuels, fossil energy still is expected to account for 78% of the global energy consumption in 2040.[116] Natural gas is probably the most promising fossil fuel, and shale gas is a major component of natural gas supplies. Horizontal drilling and multi-stage hydraulic fractured wells provide great momentum for shale gas production. However, the production behavior of shale gas wells are not well understood due to the complex non-Darcy flow behaviors in the porous and fractured reservoir.[117-119]

Before digging into the production behavior, it is imperative to understand gas flow behavior in nanopores because the produced gas accounts for most of the volume in the matrix. Non-Darcy is a frequently used term to describe flow process deviated from Darcy flow. In shale reservoirs, non-Darcy flow in the fracture refers to the flow phenomenon with inertial effects caused by high flow velocity. The Forchheimer equation and the Barree and Conway models can be used to describe this phenomenon in both single-phase and multi-phase flow.[119-122] Non-Darcy flow in the matrix is caused by the multiphysics occurred in nano-sized pores, and the term "gas apparent permeability" is frequently used to account for that.

Gas apparent permeability is related to Knudsen number and intrinsic permeability. Knudsen number is defined as the ratio of gas molecule mean free path over the representative physical length of the porous media,[22] which is the pore diameter if a circular cross-section is assumed. Physics in the nanopores affect gas flow behavior by changing either Knudsen number or intrinsic permeability, or both of them. Based on a comprehensive literature review, four physics include the effective stress on the matrix, slip flow, Fickian diffusion and Knudsen diffusion and surface diffusion. Fickian diffusion and Knudsen diffusion are also termed together as pore diffusion to distinguish from surface diffusion.[123] Surface diffusion occurs between the free gas and adsorption phase in tiny pores.

It is difficult to understand the overall effect of these physics since they occur simultaneously during the process of gas production. As gas is depleted, pressure decrease will cause mean free path growth, which increases the Knudsen number. The effective stress is increasing because gas is depleted, leading to a smaller pore size, which reduces intrinsic permeability but increases the Knudsen number. Gas desorbs from the pore surface as gas is depleted, which enlarges pore size but decreases the Knudsen number. Surface diffusion near the pore surface increases gas transport capacity throughout the process.

Experimentally, the pulse-decay method is a feasible way to study gas flow behavior in tight porous media.[1, 6, 27, 123, 124] However, the permeability obtained from a pulse-decay experiment is gas apparent permeability of the porous media depending on the gas type, temperature and pressure.[124] In the literature, these effects are usually studied separately in gas shales. For example, Heller et al. measured the Marcellus shale matrix apparent permeability under a range of pore pressure and effective stress, based on which the stress-dependent pore size is estimated.[125] Sakhaee-Pour and Bryant investigated gas apparent permeability considering slip flow and pore diffusion with a constant pore diameter.[10] Inspired by them, we combined the experimental results by Heller et al. and the theory by Sakhaee-Pour and Bryant in this study to couple the geomechanical effect, adsorption and the slip flow with pore diffusion effect.[10, 125]

Surface diffusion has been recently reported to be an important flow mechanism in organic-rich shale reservoirs. Akkutlu and Fathi reported values of diffusivity in kerogen by pulse-decay experiments.[30] Fathi and Akkutlu used Lattice Boltzmann Method to describe this phenomenon.[26] Wu et al. investigated the importance of surface diffusion in pores with various sizes.[70] Sheng et al. coupled surface diffusion with slip flow, viscous flow and Knudsen diffusion using different values of surface diffusivity.[27] They all reached the conclusion that surface diffusion contribution to shale gas flow is significant in micro and mesopores and under low pressure.

In summary, most previous studies overlook the simultaneous effects of surface diffusion and the effective stress for gas flow in nanopores. What's more, all the physics are dynamically changing from the initial reservoir pressure to the pressure at the end of production, making it more difficult to describe gas permeability evolution. Accordingly, we propose a workflow and demonstrate how the procedure proceeds to consider the multiphysics together during gas production in the tight porous shale matrix.

4.3 Knudsen number and gas permeability

Table 4-1 Classification of flow regimes by Knudsen number.

Knudsen number range	< 1E-3	1E-3 < Kn < 1E-1	1E-1< Kn < 10	Kn > 10
Flow regime	continuum	slip flow	transition flow	free molecular flow

Table 4-2 Pore size classification (IUPAC).

Pore size range, nm	d < 2nm	2 nm < d < 50 nm	d > 50 nm
Class for tiny pore	micro	meso	macro

Knudsen number (Kn) has been used widely to define flow regimes in the porous media with a small pore size (Table 4-1) which is defined as the ratio of the mean free path over pore diameter (Eq. (4-1)).[21] Eq. (4-2) describes the formula calculating mean free path in this study.[126]

$$Kn = \frac{l}{d} \tag{4-1}$$

$$l = \frac{k_B T}{\sqrt{2} Z \pi d_{mol}^2 p} \tag{4-2}$$

where l is mean free path, in the unit of m, k_B is the Boltzmann constant, 1.38065E-23, in the unit of J/K; T is temperature in the unit of K, d is pore diameter and d_{mol} is the molecule diameter, in the unit of m, p is pressure, in the unit of Pa, and Z is gas compressibility factor to account for the non-ideal behavior of gas (In the original derivation of Eq. 4-2,[126] $PV = nRT$ is applied for ideal gas,[126] in our derivation $PV = ZnRT$ is applied for non-ideal gas; therefore Z will appear in the denominator). Table 4-2 lists the classification for the level of “small” in pore size by the International Union of Pure and Applied Chemistry (IUPAC).

Using properties of methane,[55] Fig.1 plots Knudsen number values as a function of pore pressure. Pore diameter is set to be 5 nm, 50 nm and 1,000 nm, which covers a wide range of pore size in organic matters reported by Wang and Reed.[127] Temperature is set to be from 100 °F to 400 °F which covers the temperature in most reservoirs. It shows that for most pores, from the initial pore pressure (usually below 10,000 psi) to the pore pressure at the end of production, flow regimes are in transition and slip flow regions. When the pore size is on the order of micrometer scale (> 1 μm), flow regime will shift to continuum flow when the reservoir pressure is higher than 1,000 psi, approximately. It also shows that a higher Knudsen number is obtained at a higher temperature.

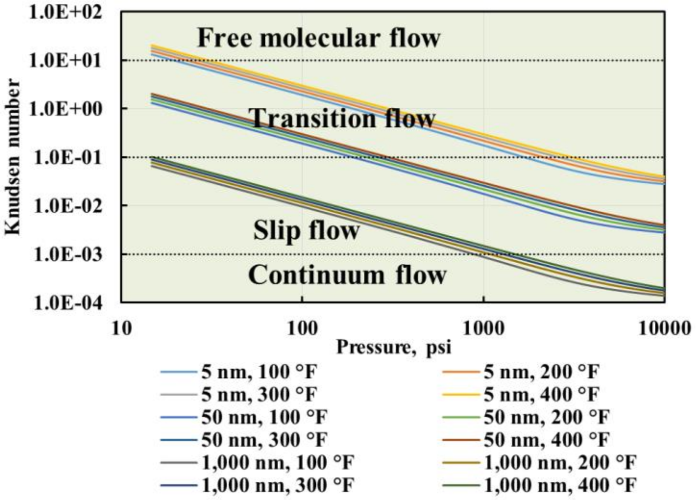

Figure 4-1 Flow regimes as a function of pressure in a typical shale gas reservoir.

Intrinsic permeability of the porous media is an inherent property of the porous media independent of flow conditions. It is termed interchangeably with liquid permeability or Darcy permeability. It is used when the pore size is relatively large, the flowing fluid is liquid, and the non-slip boundary condition is valid. The corresponding flow mechanism is continuum flow which occurs when the Knudsen number is below 1E-3. When the pore size is small and the flowing fluid is gas, the non-slip boundary condition breaks down, and the flow mechanism changes. Figure 4-2 describes several possible flow mechanisms in a small pore. When the Knudsen number is larger than 1E-3, gas slippage at the pore surface begins to enhance permeability, as indicated by the round dotted line. Surface diffusion is important in nanopores when the size of the gas molecule is comparable to the pore size.[70] It occurs in the region between the adsorption phase and free gas. Gas molecule moves from one spot to another by a "hopping" mechanism, as indicated by the black curve.[25] Pore diffusion, as indicated by the long dashed line, can be either Fickian diffusion or Knudsen diffusion; the latter one occurs when the mean free path of gas molecule size is comparable to the pore size. It involves frequent collisions between gas molecules and the pore surface. Viscous flow is also termed as Darcy flow that it is a major component of gas flow under high pressure and in conventional reservoirs with a large pore size, as indicated by the solid line.[21]

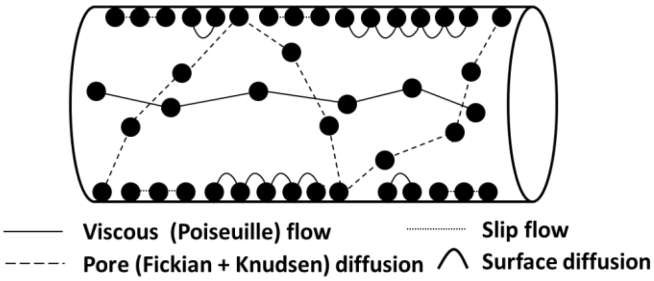

Figure 4-2 Flow mechanisms in nanopores. Molecules connected by lines (solid and dashed) indicate the flow path traveled by one molecule with time.

Knudsen number frequently acts as the connecting link between gas apparent permeability and intrinsic permeability. In this work, we employed the analytical relationships provided by the work of Sakhaee-Pour and Bryant.[10] Eq. (4-3) and (4-4) are used to describe the ratio between gas apparent permeability and intrinsic permeability in slip flow region (1E-3<Kn<1E-1) and transitional flow region (1E-1 < *Kn* < 10), respectively. Eq. (4-3) is constructed by imposing a first order slip boundary condition and Eq. (4-4) is constructed based on a high-order boundary condition.

$$f(K_n) = \frac{k_a}{k_\infty} = 1 + \alpha_1 K_n \tag{4-3}$$

$$f(K_n) = \frac{k_a}{k_\infty} = 0.8453 + 5.4576 K_n + 0.1633 K_n^2 \tag{4-4}$$

f(Kn) acts as the intrinsic permeability multiplier to obtain the apparent permeability. In Eq. (4-3), the value of α1 depends on the geometry of the porous media. Assuming the cross section is circular, α_1 is 5 if the first order Klinkenberg equation is applied and 13.58 if the Dusty Gas Model (DGS) is applied as reported by Sakhaee-Pour and Bryant.[10] Coefficients in Eq. (4-4) are obtained based on the results of the nonlinear regression model. In this study, we assume Eq. (4-

4) is fairly accurate considering the different values of α_1 using different methods and set Eq. (4-3) and (4-4) equal to one another at the transition point $Kn = 0.1$. Thus an adjusted value of α_1 and a smooth curve of $f(Kn)$ could be obtained, where $f(Kn)$ is positively related with Kn and larger than 1.

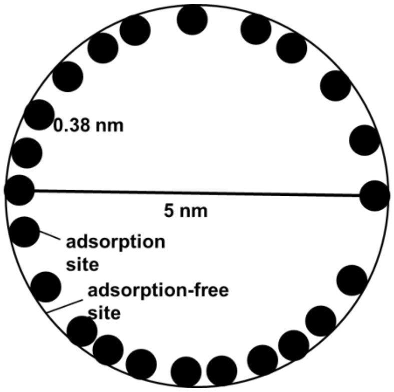

Figure 4-3 Schematic of monolayer adsorption of methane in a 5 nm-diameter pore.

Figure 4-3 shows the schematic when monolayer adsorption is present in a circular pore with the diameter of 5 nm. The black dot represents methane molecule with the diameter of 0.38 nm. Both adsorption spot and adsorption-free spot are available on the pore surface. The Langmuir isotherm can approximate the adsorption amount *q*:

$$q(p) = \frac{q_m p}{p + p_L} \tag{4-5}$$

where q_m is the maximum adsorption amount, and P_L is the Langmuir pressure at which half of the maximum adsorption amount is obtained.

The coverage of adsorption on surface area, θ, under the pressure *p* is

$$\theta = \frac{q(p)}{q_m} = \frac{p}{p + p_L} \tag{4-6}$$

Assuming the pore surface is fully covered with monolayer adsorption ($\theta = 1$), diameters of 5 nm, 50 nm will be reduced to 4.24 nm and 49.24 nm, respectively. Figure 4-4 plots of $f(Kn)$

as a function of pressure in a pore with diameters of 5 nm and 50 nm. For comparison, the curves with the reduced diameters because of adsorption are plotted as well. The dividing lines are drawn to separate transition flow and slip flow regimes at the point Knudsen number equals 0.1. α1 is adjusted based on the original value 5 to obtain a continuous and smooth curve for *f(Kn*). It is observed that the dividing pressure separating the two flow regimes increases as the pore size becomes smaller. Moreover, as pore size increases to 50 nm, the influence of adsorption on *f(Kn*) becomes negligible.

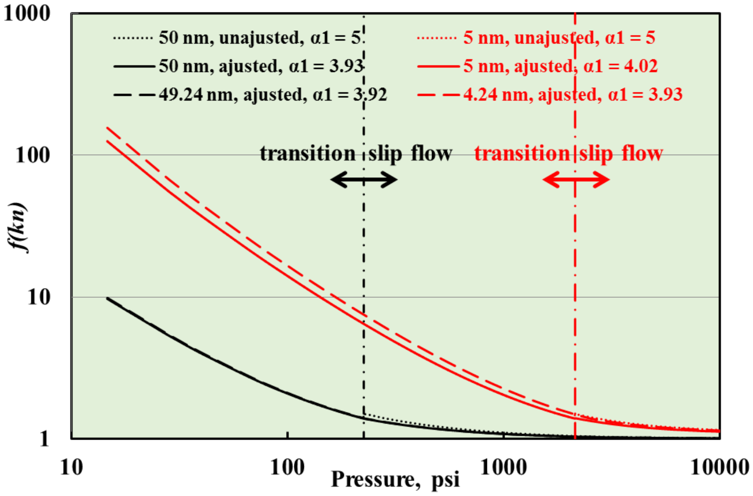

Figure 4-4 *f(Kn)* as a function of pore pressure in 5 nm-diameter and 50-nm diameter pores w/ and without modifying α1, the gas type is methane.

Reduction of pore size leads to the decrease of intrinsic permeability of the porous media, which is unfavorable to gas permeability. On the other hand, the adsorption layer increases *f(Kn*), which is favorable to gas permeability. Another significant physics affecting shale gas permeability is the effective stress. During shale gas production, the effective stress increases as gas is depleted, which reduces the intrinsic permeability. However, this effect also increases *f(Kn*), like that of the adsorption layer. Net effects of the geomechanical effect and the adsorption layer on the gas apparent permeability are not certain but a detailed calculation can estimate that.

It is noticed that Eq. (4-3) and Eq. (4-4) do not include surface diffusion. Therefore, *f(Kn)* should be modified after including this phenomenon. In the following sections, we will use data from a complete set of experiments performed on the Marcellus shale as an example to present procedures to take these physics into account step by step.

4.4 Results of permeability tests of the Marcellus shale

Heller et al. performed helium permeability measurements under the effective stress of 2,000 psi, 3,000 psi, and 4,000 psi on the porous shale matrix.[125] Figure 4-5 captures and plots their experimental permeability data points as a function of the reciprocal of pore pressure. Klinkenberg equations are used to fit the linear trend lines.[12]

$$\frac{k_a}{k_\infty} = 1 + \frac{k_b}{p} \tag{4-7}$$

where k_∞ is estimated as the intercept of the linear line. k_b is related to slippage and pore diffusion and is expressed as the equation

$$k_b = \frac{16c\mu}{d}\left(\frac{2RT}{\pi M_g}\right)^{1/2} \tag{4-8}$$

where c is gas compressibility, μ is gas viscosity, M_g is gas molecular weight, R is universal constant, and T is temperature. Based on this equation, pore size can be estimated. Figure 4-5 shows permeability profiles under the effective stress of 2,000, 3,000, and 4,000 psi. The increasing effective stress leads to the decrease of intrinsic permeability and pore size. Figure 4-6 shows a good linear relationship between the pore size and effective stress is obtained, which is extrapolated backward and forward to cover pore pressure investigated in this study.

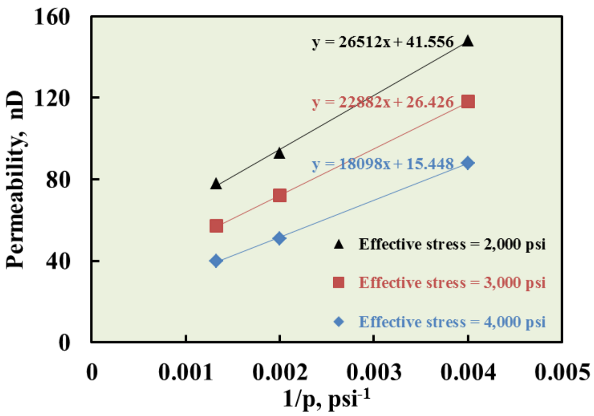

Figure 4-5 Gas permeability vs. 1/p under different effective stress.

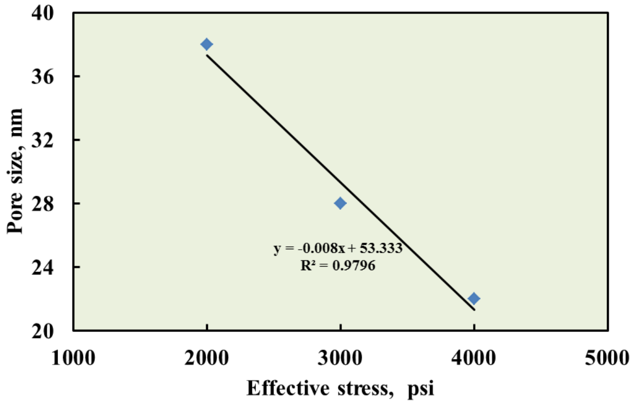

Figure 4-6 Size of nanopores under different effective stress.

The intrinsic permeability of the porous media is proportional to the square of pore size.

$$k_\infty \propto d^2 \tag{4-9}$$

Table 4-3 lists values of the pore size, the estimated intrinsic permeability from the intercept of the plot of permeability vs. reciprocal of pore pressure, and ratios between them are calculated. These values do not present a decreasing or increasing trend as effective stress increases. Mean value of the three ratios is calculated to be 3.15E-2 nD/nm^2. We make a compromise by assuming this mean value serves as a proportionality constant to calculate the intrinsic permeability at a given pore pressure during the production process.

Table 4-3 Intrinsic permeability and pore size under different effective stress for the Marcellus shale.

Effective stress, psi	Intrinsic permeability, k_∞, nD	Pore size, d, nm	$\frac{k_\infty}{d^2}$	Mean value of $\frac{k_\infty}{d^2}$
2,000	41.56	38	2.88E-2	3.15E-2
3,000	26.43	28	3.37E-2	
4,000	15.45	22	3.19E-2	

4.5 Langmuir adsorption isotherms of the Marcellus shale

Heller and Zoback measured methane adsorption on the same Marcellus shale sample and fit the adsorption profiles with the Langmuir model.[128] Because their tests were performed under laboratory temperature (104 °F); and generally, adsorption is higher under a lower temperature with the same reservoir pressure. The real temperature in the Marcellus shale is approximately 130 °F. Thus, we need to elevate the Langmuir isotherm to a higher temperature using one reliable correlation.

The parameter p_L involved in the Langmuir model (Eq. (4-5)) is expressed as:[130]

$$p_L(T) = \frac{1}{k_0 T^{-1/2} e^{-E/RT}} \tag{4-10}$$

where R is gas universal constant, in the unit of kcal K^{-1} mol^{-1}, T is temperature in the unit of K, k_0 is a constant, and E is characteristic adsorption energy in the unit of kcal/mol. k_0 and E are independent of temperature and pressure. We can see that at least two series of adsorption measurements under different temperatures are needed to be performed to estimate k_0 and E. Because only one series of data are available, we employ the E value obtained from the Devonian shale by Lu et al.: -3.74 kcal/mol.[118] Then the p_L at a different temperature can be estimated whereas q_m is the same when the temperature changes. Table 4-4 lists values of p_L and q_m in the Langmuir model under the laboratory temperature 104 °F and the elevated reservoir temperature 130 °F. Figure 4-7 plots the two adsorption isotherms under 104 °F and 130 °F.

Table 4-4 Langmuir model parameters under laboratory temperature and reservoir temperature for the Marcellus shale.

Temperature, °F	104	130
p_L, psi	556.2	741.5
q_m, scf/ton	28.3	

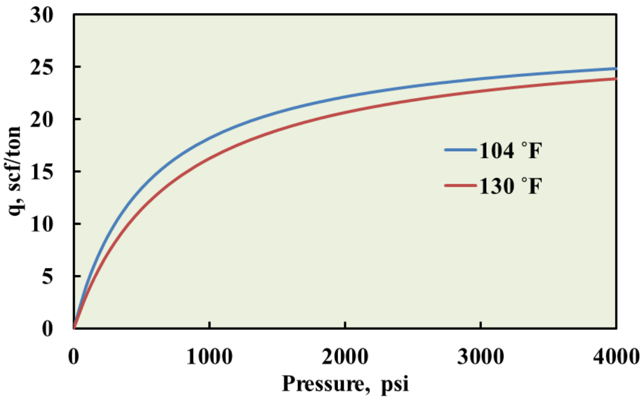

Figure 4-7 Adsorption isotherms of the Marcellus shale under the laboratory temperature (104 °F) and reservoir temperature (130 °F).

4.6 Methodology

Figure 4-8 describes the complex responses of k_∞ and *f(Kn)* during the process of pressure depletion. Gas apparent permeability is the product of k_∞ and *f(Kn)* while k_∞ is proportional to the square of pore diameter. *Kn* increases as reservoir pressure decreases. The increase of the effective stress and gas desorption occur as pressure decreases, they lead to pore size decrease and increase, respectively. Pore size increase directly causes k_∞ to increase and pore size decrease causes k_∞ to decrease. On the other hand, pore size increase induces the decrease of *Kn*, and consequently, *f(Kn)* decreases. In contrast, the decrease of pore size leads to *f(Kn)* increase.

Different phenomena affecting gas permeability in Figure 4-8 include the increasing effective stress, slip flow/pore diffusion and adsorption/desorption. The effective stress and gas desorption both have competing impacts influencing gas permeability. It is difficult to derive a model to fully couple all of them. A convenient way suggested in this work in is to consider these phenomena step by step. Surface diffusion is not shown in Figure 4-8 and it is taken into account at the last step by modifying the intrinsic permeability multiplier (section 5.4).

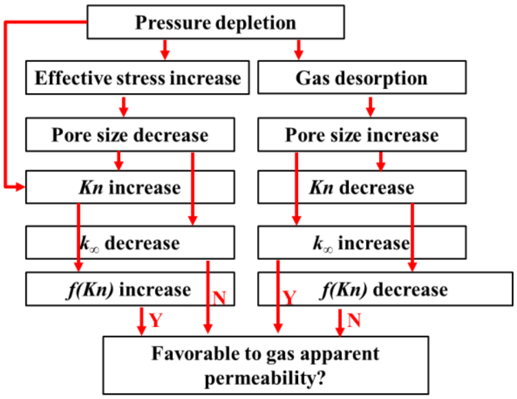

Figure 4-8 Change of k_∞ and *f(Kn)* during the pressure depletion process of gas production.

Table 4-5 to Table 4-8 list procedures to investigate the physics at a certain reservoir pressure. Two reservoir pressure examples are illustrated: 4,000 psi and 520 psi. The Table C1 and Table C2 in Appendix C provide the complete calculation procedures from 4,000 psi to 40 psi with the pressure step of 120 psi.

Table 4-5 describes the scenario considering the geomechanical effect. Table 4-6 describes the scenario considering the geomechanical effect and slip flow/pore diffusion. Table 4-7 describes the scenario considering the three physics: the geomechanical effect, slip flow/pore diffusion and adsorption layer. Table 4-8 describes scenarios considering all the aforementioned physics and surface diffusion.

4.6.1 Step 1: geomechanical effect

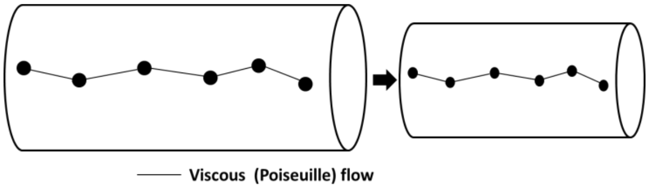

Figure 4-9 Step 1: include the geomechanical effect that reduces the pore size. Molecules connected by lines indicate the flow path traveled by one molecule with time.

The first step is to include the geomechanical effect (Figure 4-9). Initial pore pressure for the Marcellus shale is 4,000 psi and the initial effective stress is 1,000 psi. The effective stress increases as the pore pressure decreases. The corresponding initial pore size is 45.33 nm, as extrapolated from the trend lines in Figure 4-5. Using the proportionality constant in Table 4-3, we estimate the initial gas permeability by multiplying it with the stress-dependent pore size, which is 45.33 nm under the pore pressure 4,000 psi and the corresponding effective stress 1,000 psi.

$$k_{\infty} = 3.15E - 2 \times r^2 = 3.15E - 2 \times 45.33^2 = 64.66nD.$$

Table 4-5 Step 1-Geomechanical effect.

Pore pressure: p, psi	Effective stress: p_s, psi	Pore size: d, nm	Initial intrinsic permeability: k_∞, nD
4,000	1,000	45.33	64.66
520	4,480	17.49	9.63

4.6.2 Step 2: slip flow/pore diffusion

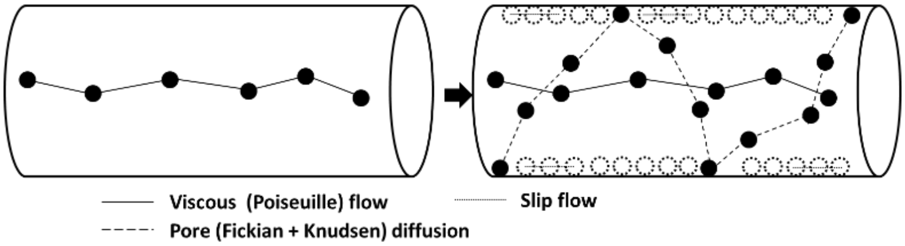

Figure 4-10 Step 2: include slip flow and pore diffusion based on step 1. Molecules connected by lines (solid and dashed) indicate the flow path traveled by one molecule with time.

The second step is to include the slip flow/pore diffusion component (Figure 4-10). *f(Kn)* is calculated using Eq. (4-3) and (4-4) in the two flow regimes. Its value under the initial pressure is 1.02, so the initial apparent permeability is

$$k_a = k_{\infty} \times f(Kn) = 64.67nD \times 1.02 = 65.99nD$$

Table 4-6 Step 2-Geomechanical effect and slip flow/pore diffusion.

Pore pressure p, psi	Pore size: r, nm	Kn	$f(Kn)$	Intrinsic permeability: k_∞, nD	Apparent permeability: k_a, nD
4,000	45.33	5.25E-3	1.02	64.66	65.99
520	17.49	1.08E-2	1.44	9.63	13.82

4.6.3 Step 3: adsorption layer effect

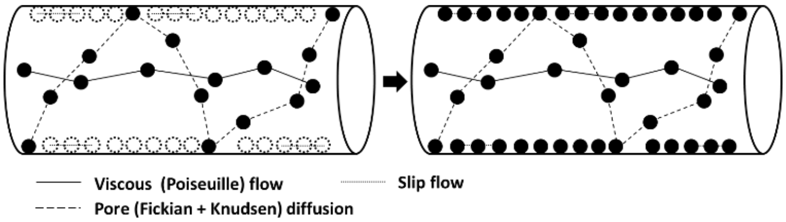

Figure 4-11 Step 3: include the adsorption layer based on step 2. The dashed dots indicate the volume of adsorption molecules is not considered while the solid dots indicate the volume of the adsorption molecules is considered. Molecules connected by lines (solid and dashed) indicate the flow path traveled by one molecule with time. Note: the schematic drawn here belongs to a specific size range of pores which is a good representative of our current shale gas/oil systems (0.01-1 µm).

The third step is to include the effect of adsorption layer without considering surface diffusion impact (Figure 4-11). Adsorption coverage on the pore surface under the initial reservoir pressure 4,000 psi (Eq. (4-6)) is

$$\theta = \frac{p}{p + p_L} = \frac{4,000}{4,000 + 741.5} = 0.84$$

where 741.5 psi is the Langmuir pressure that we estimated under the elevated reservoir temperature (Table 4-4).

Using the coverage value as the weighting factor, the corresponding effective pore size is

$$d_{eff} = d \times (1-\theta) + d_{ad} \times \theta = 45.33 \times (1-0.84) + 44.57 \times 0.84 = 44.69nm$$

thus, the effective intrinsic permeability is

$$k_{\infty eff} = 3.15E-2 \times d_{eff}^2 = 3.15E-2 \times 44.69^2 = 62.84nD.$$

The corresponding effective $f(Kn)$ is

$$f(Kn)_{eff} = f(Kn)\times(1-\theta) + f(Kn)_{ad}\times\theta = 1.02\times(1-0.84)+1.02\times0.84 = 1.02.$$

Thus, the effective apparent permeability is

$$k_{aeff} = k_{\infty eff}\times f(Kn)_{eff} = 62.84\times1.02 = 64.16nD$$

Table 4-7 Geomechanical effect, slip flow/pore diffusion and adsorption layer effect.

Pore pressure, psi	Pore size with adsorption: d_{ad}, nm	*f(Kn)* with adsorption: $f(Kn)_{ad}$	Adsorption coverage: θ	Effective pore size: d_{eff}, nm	Effective *f(Kn)*: $f(Kn)_{eff}$	Effective intrinsic permeability: $k_{\infty\,eff}$, nD	Effective apparent permeability: k_{aeff}, nD
4,000	44.57	1.02	0.84	44.69	1.02	62.84	64.16
520	16.73	1.46	0.41	17.18	1.45	9.28	13.43

4.6.4 Step 4: surface diffusion

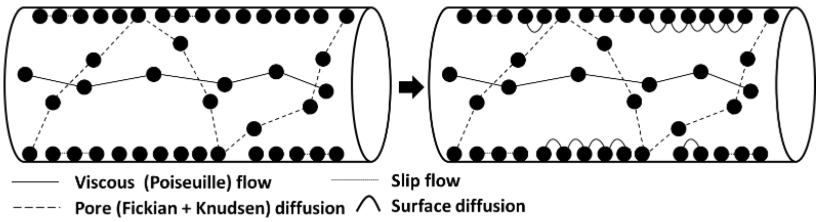

Figure 4-12 Step 4: include surface diffusion based on step 3. Molecules connected by lines (solid and dashed) indicate the flow path traveled by one molecule with time.

The final step is to include the effect of surface diffusion (Figure 4-12).

The mass flux of the Darcy component is:

$$J_D = -6.805\times10^{-18}\,\frac{k_{\infty eff}\,\rho_g\partial p}{\mu_g\partial x} \tag{4-11}$$

where ρ_g is gas density, in kg m^{-3}; μ_g is gas viscosity, in the unit of Pa·s.

The mass flux of the surface diffusion is:

$$J_{s-d} = -\frac{3.281 D_{s-d} C_{ad}\partial p}{p\partial x} \tag{4-12}$$

where $D_{s\text{-}d}$ is surface diffusivity, in the unit of m^2/s; C_{ad} is adsorption amount in a unit volume of rock, in the unit of kg/m^3; $J_{s\text{-}d}$ is in the unit of kg/(m^2·s). C_{ad} is calculated with the following formula.

$$C_{ad} = \frac{M_g q_m \theta \rho_r}{35.315 V_{std}} \tag{4-13}$$

where M_g is methane molecular weight which is 1.6E-2 kg/mol; ρ_r is rock density which is 2,400 kg/m^3 in this study; V_{std} is the standard volume of gas which is 22.4 L/mol.

If we make the surface diffusion flux formula in the form of the Darcy flux formula using an effective permeability $k_{s\text{-}d}$ for surface diffusion, Eq. (4-11) becomes

$$J_{s-d} = -6.805 \times 10^{-18} \frac{k_{s-d} \rho_g \partial p}{\mu_g \partial x} \tag{4-14}$$

thus, $k_{s\text{-}d}$ can be converted with Eq.(15)

$$k_{s-d} = 1.470 \times 10^{17} \frac{D_{s-d} C_{ad} \mu_g}{\rho_g p} \tag{4-15}$$

Therefore, the ratio between $k_{s\text{-}d}$ and $k_{\infty eff}$ is calculated as

$$F = 4.161 \times 10^{12} \frac{M D_{s-d} q_m \theta \rho_r \mu_g}{k_{\infty eff} \rho_g p V_{std}} \tag{4-16}$$

The final correction factor is added onto $f(Kn)_{eff}$ to obtain the final multiplier for $k_{\infty eff}$

$$f(Kn)_{tot} = f(Kn)_{eff} + F \tag{4-17}$$

The final apparent permeability including all the physics is

$$k_{atot} = k_{\infty eff} f(Kn)_{tot} \tag{4-18}$$

Table 4-8 Geomechanical effect, slip flow/pore diffusion, adsorption layer effect and surface diffusion.

Pore pressure, psi	Surface diffusivity: D_{s-d}, m^2/s	Gas viscosity: μ_g, Pa·s	Gas density: ρ_g, kg/m^3	Adsorption coverage: θ	Effective intrinsic permeability: $k_{\infty\ eff}$, nD	Effective $f(Kn)$: $f(Kn)_{eff}$	Ratio between k_{s-d} and $k_{\infty eff}$: F	Final correction factor: $f(Kn)_{tot}$	Final apparent permeability: k_{atot}, nD
4,000	1E-8	2.16E-5	174.41	0.84	62.84	1.02	8.40E-4	1.02	64.21
520	1E-8	1.26E-5	22.02	0.41	9.28	1.45	9.83E-2	1.55	14.34

Currently, the data of shale gas surface diffusivity are limited and there are no standard methods available to measure it in shales. Kang et al. reported the surface diffusivity in the kerogen to be between 1.55E-7 m^2/s and 8.80E-6 m^2/s and Akkutlu and Fathi reported it to be between 5.1E-8 m^2/s and 8.80E-6 m^2/s.[25, 30] Pressure pulse-decay experiments were usually performed to measure the surface diffusivity. A pressure pulse is introduced at the core upstream at the start of this experiment, and the pressure decline curve at the upstream is used to estimate the surface diffusivity value which is believed to be a function of gas type, temperature, pressure, pore size and TOC percentage. Considering the wide range of surface diffusivity, in this study, we decided to change it from 1E-8 m^2/s to 1E-5 m^2/s to observe impacts of different values on the flow behavior.

4.7 Results and discussion

4.7.1 Effects of the four types of physics

Figure 4-13 quantifies the geomechanical effect (effective stress), slip flow/pore diffusion and adsorption layer effect but no surface diffusion based on the results from step 1 to step 3. Pore pressure investigated ranges from the initial pressure 4,000 psi to the pressure at the end of production 40 psi.

Effective stress decreases the intrinsic permeability monotonically by reducing the pore size throughout the production process. Its impact is significant, the intrinsic permeability decrease from 64.66 nD initially to 5.86 nD at the pore pressure 40 psi, causing 91% permeability loss (dark red dotted curve in Figure 4-13).

Slip flow and pore diffusion help relieve the permeability decrease caused by the geomechanical effect. A turning point as well as the lowest point is observed which indicates slip flow and pore diffusion begins to overwhelm the geomechanical effect and cause the apparent permeability to increase at a critical pore pressure. The critical pore pressure is approximately at 500 psi (marked by the red cross). In addition, we can obtain the contribution of slip flow and pore diffusion to the total apparent permeability in the purple dotted curve by subtracting the intrinsic permeability in the dark red dotted curve. The calculated results indicate that slip flow and pore diffusion component outweighs the Darcy component approximately at 280 psi.

If we consider the effect the adsorption layer only regarding reducing the effective pore size, the impact is negligible since the orange dotted curve only deviated a little form the purple dotted curve. The impact is small because by there is great disparity between the molecule size and the pore size which is within mesoscale (2 nm-50 nm) in this study. Therefore, the impact is expected to be more significant if the pore size reduces to microscale. Besides, the orange dotted curve is higher than the purple dotted curve indicating that the positive effect from the slip flow and pore diffusion is larger than the negative effect from the effective pore size reduction.

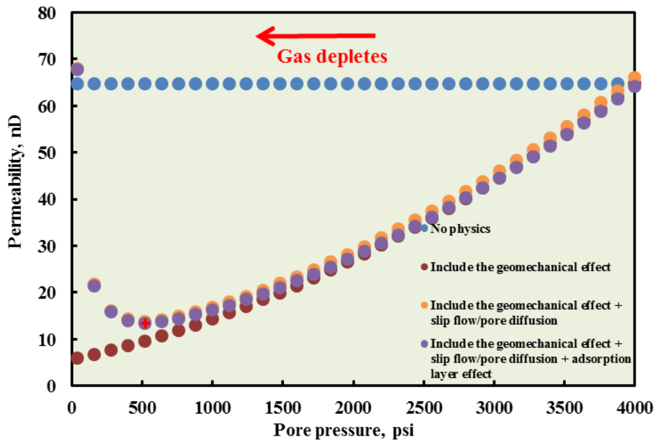

Figure 4-13 Permeability evolution during gas depletion in the Marcellus shale.

Figure 4-14 shows gas permeability evolution after including all the physics: the geomechanical effect, slip flow and pore diffusion, adsorption and surface diffusion. Four surface diffusivity values are investigated: 1E-8 m^2/s, 1E-7 m^2/s, 1E-6 m^2/s and 1E-5 m^2/s. Values in all the dotted curves of Figure 4-14 are larger than those in the orange dotted orange curve of Figure 4-13, indicating that surface diffusion enhances gas apparent permeability throughout the production process; and the difference between them are larger under low pressure indicating that surface diffusion is more important under low pressure. This characteristic is similar with that of slip flow and pore diffusion. As expected, a higher $D_{s\text{-}d}$ contributes more to the gas permeability. When $D_{s\text{-}d}$ is in the range of 1E-8 m^2/s and 1E-5 m^2/s, gas permeability still decreases at high pressure and increases at low pressure and the period of decreasing is shortened with a larger $D_{s\text{-}d}$, and the turning pressure point from decreasing trend to increasing trend is higher with a larger $D_{s\text{-}d}$. The decreasing trend is caused by the increasing effective stress and the adsorption layer that reduce the pore size that decrease the intrinsic permeability, and the increasing trend is caused by the slip flow and pore diffusion and surface diffusion. It is observed when $D_{s\text{-}d}$ increases to 1E-5 m^2/s, the turning point in the curve disappears that the total gas apparent permeability shows an increasing trend throughout the production process.

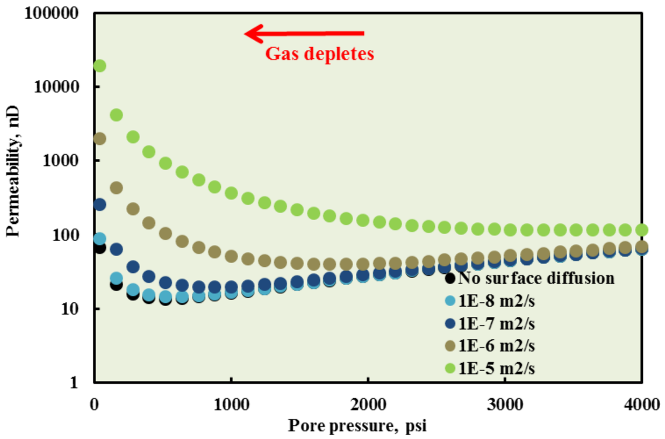

Figure 4-14 Total gas apparent permeability with various values of surface diffusivity.

To the best of our knowledge, this is the first attempt made in the open literature to quantify the multiphysics as a function of pore pressure, separately and totally during the lifetime of a shale gas reservoir, based on real shale reservoir geological settings and a series of experimental data. The results from this study demonstrate the aforementioned competing processes acting on shale matrix, which affect the flow behavior during shale gas production.

4.7.2 Sensitivity analysis of the magnitude of pore size versus effective stress

In this section, sensitivity analysis is performed to investigate the influence of the magnitude of pore sizes smaller than 50 nm with two subgroups. The subgroup of small pore size is 1/4th of the larger pore size group as a function of effective stress (Figure 4-15).

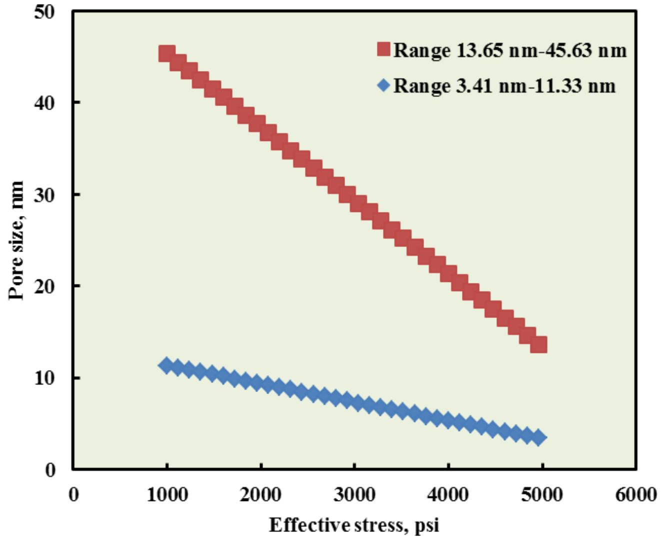

Figure 4-15 Pore size range 3.41 nm-11.33 nm and 13.65 nm-45.33 nm as a function of the effective stress.

Procedures to include the aforementioned physics are repeated for the updated pore size variations. Figure 4-16 and Figure 4-17 summarize the results as compared with Figure 4-13 and Figure 4-14. From Figure 4-16, it is observed that the permeability magnitude is much decreased but the overall trends of gas apparent permeability do not change. One novel finding in Figure 4-16 is that the critical turning point appears early during the gas depletion process: it is approximately at 1,000 psi (marked by the red cross) compared with 500 psi in Figure 4-13. Figure 4-17 shows that the difference between different surface diffusivity scenarios becomes larger as the pore size is reduced, indicating that surface diffusion plays a more important role in reservoirs with smaller pore size. The limiting surface diffusivity value that causes the gas apparent permeability increase throughout the gas depletion process lies between 1E-7 m^2/s and 1E-6 m^2/s, which is one order of magnitude smaller than the previous value which is between 1E-6 m^2/s and 1E-5 m^2/s.

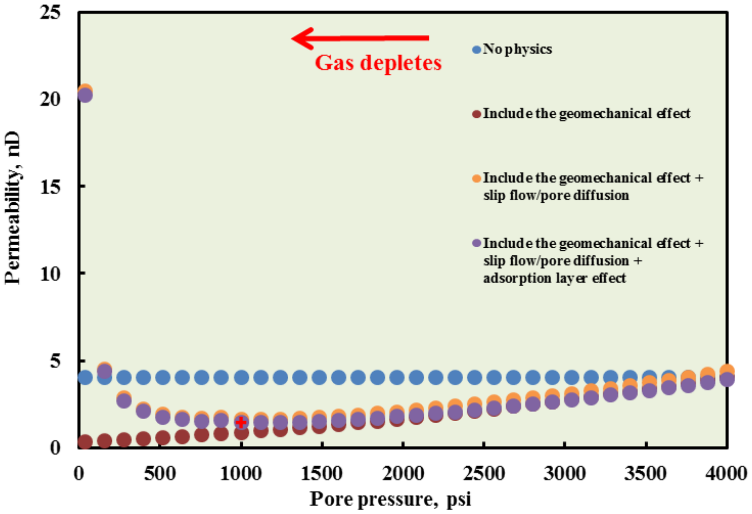

Figure 4-16 Permeability evolutions with the multiphysics using the updated pore size change as compared with Figure 4-13.

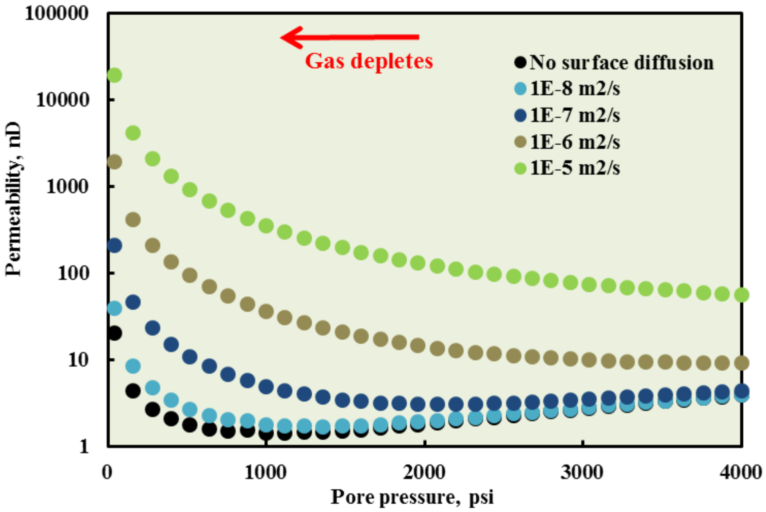

Figure 4-17 Permeability evolutions with different diffusivity using the updated pore size change as compared with Figure 4-14.

To experimentally validate the changes in gas apparent permeability, one needs to simulate the gas depletion process in real reservoirs. A series of gas apparent permeability experiments are required by varying the effective stress σ_e instead of the total stress σ_{tot} constant (Eq. (4-19)).[131] Transient gas transmission experiments might be more applicable than the conventional stead-steady methods for the nono-Darcy permeability scale of the tight shale matrix because the tests will be very time-consuming and the pressure drop across the core sample will be extremely high. A series of gas adsorption experiments are also required to characterize the adsorption isotherm to evaluate the adsorbed phase effect.

$$\sigma_e = \sigma_{tot} - \alpha P_p \tag{4-19}$$

4.7.3 Implications for shale gas production behavior

There are several implications for shale gas production behavior based on the results of shale gas flow behaviors obtained in this study.

The gas apparent permeability evolution during the lifetime of a gas well is complex due to the multiphysics. Accurate input of the dynamic shale petrophysical properties into reservoir simulators is important because most of the gas is stored in nanopores. Yu et al. showed that the total gas storage capacity in the Marcellus shale is positively correlated with the total organic carbon (TOC) fraction, and sometimes the simple monolayer Langmuir model fails to fit the adsorption isotherm.[73] Yu et al. showed that gas desorption contributes significantly to the early stage of gas production because the slope of the multilayer BET isotherm is sharper under high pressure. On this basis, gas adsorption contributes to gas recovery process because it increases the total gas in place (GIP). In this study we showed that adsorption also affects gas apparent permeability by reducing the effective pore size and inducing the surface diffusion phenomenon. For the BET adsorption scenario, the effective pore size will be reduced even further because the adsorbed phase occupies more volume in the pore space leading to further reduction of the intrinsic permeability. The multi-layer BET adsorption-induced surface diffusion should contribute more to the gas apparent permeability and it is obviously more complex than what is induced by the monolayer adsorption. To properly describe this, one needs to propose reliable models using kinetic theories considering not only the interactions between the rock surface and adsorbed molecules but also adsorbed molecules at different layers as well as between the adsorbed molecules and the free gas molecules.[13]

It has been experimentally proven that pore size reduces as the effective stress increases. However, we should notice that porosity of the porous media is not only related to the pore size but also related to the total number of pores. The number of pores does not necessarily remain constant because the structure of the pore network changes with the increasing effective stress. Thus, the relationship between the number of pores and effective stress might be needed for more petrophysical properties input.

In this study, a linear relationship between the pore size and effective stress is used. However, if more data points are collected, the relationship is not necessarily linear; so for a more realistic study, a wider range of effective stress values might be needed.

Surface diffusion positively contributes to the total gas permeability. However, the level of contribution largely depends on the value of surface diffusivity. Thus, an accurate laboratory-measured surface diffusivity is important for flow behavior description.

Although slip flow, pore diffusion and surface diffusion are believed to increase gas apparent permeability significantly under low reservoir pressure that we also proved this point in this work, it is not enough to justify the effects of multiphysics on the shale gas production behavior, which is more meaningful for real shale gas reservoir operators. The reason is that gas density is low at low pressure, which means that even gas apparent permeability is high under low pressure, shale gas production might be enhanced not much. For this reason, mass flux evaluation instead of permeability evaluation is more insightful for the purpose of justifying impacts of the multiphysics. In real field applications, the formation compaction not only reduces the pore size of nanopores but also reduces the width of the natural fracture and the artificial hydraulic fracture.

Besides, Forchheimer flow behavior caused by the inertial effect takes place in fractures. Therefore, dynamic properties of both nanopores and fractures should be realistically described using reservoir simulations to predict the reservoir production performance. For this purpose, this study provides the dynamic properties of nanopores that can be conveniently applied in the input of reservoir simulator.

4.8 Conclusions

The following conclusions regarding impacts of multiphysics on the matrix are obtained from this study.

Fully describing shale gas permeability evolution during the production process calls for three sets of experimental data: intrinsic permeability under different effective stress using non-adsorptive gas, adsorption isotherm under reservoir conditions and surface diffusivity measurement by the pulse-decay method.

The geomechanical effect, slip flow/pore diffusion, adsorption layer and surface diffusion all play roles affecting gas permeability evolution in shale reservoirs. Neglecting any of them might lead to incorrect properties of the tight porous media.

The increasing effective stress during shale gas production is unfavorable to shale gas flow process. Gas permeability is significantly lost due to the increasing effective stress.

Slip flow and pore diffusion are important for gas permeability under low pressure in the tight porous media. They might overwhelm the geomechanical effect and cause gas permeability enhancement at low pressure.

Adsorption layer reduces the gas permeability by reducing the effective pore size, but the effect is limited.

Surface diffusion increases gas permeability more under lower pressure. The total gas apparent permeability might keep increasing during the gas production process when the surface diffusivity is larger than a critical value.

Sensitivity analysis regarding the pore size magnitude reveals that, the turning pressure point at which gas apparent permeability begins to increase appears earlier in reservoirs with smaller pore size and surface diffusion is more important in smaller pores.

4.9 Nomenclature

c	Gas compressibility, 1/psi or 1/Pa
C_{ad}	Adsorption amount in a unit volume of rock, kg/m^3
d	Pore size, nm
d_{ad}	Pore size with adsorption, nm
d_{eff}	Effective pore diameter, nm
d_{mol}	Molecule diameter, nm
D	Gas molecule size, nm
D_{s-d}	Surface diffusivity, m^2/s
E	Characteristic adsorption energy of the porous media, kcal/mol
F	Ratio between k_{s-d} and $k_{\infty eff}$, dimensionless
$f(Kn)$	Ratio of gas apparent permeability over intrinsic permeability, dimensionless
$f(Kn)_{ad}$	$f(kn)$ with adsorption, dimensionless
$f(Kn)_{eff}$	Effective $f(kn)$, dimensionless
$f(Kn)_{tot}$	Final $f(kn)$ considering all the physics, dimensionless
J_D	Mass flux of Darcy flow, kg/(m^2·s)

$J_{s\text{-}d}$	Mass flux of surface diffusion, kg/(m^2·s)
k_0	Constant in the equation of the Langmuir pressure, K$^{1/2}$/psi
k_∞	Intrinsic permeability, nD
$k_{\infty eff}$	Effective intrinsic permeability, nD
k_a	Apparent permeability, nD
k_{aeff}	Effective apparent permeability, nD
k_{atot}	Apparent permeability considering all the physics, nD
k_B	Boltzmann constant, J/K
k_b	Klinkenberg term, psi
k_{eff}	Effective permeability, nD
k_f	Fracture permeability, mD
k_m	Matrix permeability, nD
Kn	Knudsen number, dimensionless
$k_{s\text{-}d}$	Effective permeability for surface diffusion, nD
l	Mean free path, m
M_g	Molecular weight, kg/mol
P	Pressure, psi or Pa
p_L	Langmuir pressure, psi
q	Adsorption amount, scf/ton
q_m	Maximum adsorption amount, scf/ton
R	Gas constant, J/(K·mol) or kcal/(K·mol)
T	Temperature, °F or K
v_{std}	Standard volume of gas, L/mol

α_1	Coefficient of permeability enhancement, dimensionless
θ	Adsorption coverage on the pore surface, dimensionless
μ_g	Viscosity, Pa·s
ρ_g	Gas density, kg/m^3
ρ_r	Rock density, kg/m^3
σ_e	Effective stress, psi
σ_{tot}	Total stress, psi
α	Biot coefficient, dimensionless

Chapter 5: Simulation study of shale gas production

The material in this chapter is currently under review by the journal of *SPE Reservoir Evaluation & Engineering*. The manuscript was submitted 16 January 2018, and the revised manuscript was submitted 29 October 2018.

5.1 Summary

Shale gas is a major component of natural gas supply in the United States. Multi-stage fractured horizontal wells significantly improve production performance of ultra-low permeability shale gas reservoirs. Researchers have believed that shale gas production simulations should take into account the complex flow behaviors in both fractures and the matrix. However, multiple physics exerted on the matrix considered are generally incomplete in previous studies. In this study, we considered comprehensive physics occurred in the matrix including the effective stress, slip flow/pore diffusion, adsorption/desorption, and surface diffusion, as well as dynamic properties of fractures. We investigated the importance of these physics separately and integratedly by step-by-step production simulations. Afterward, comprehensive sensitivity analysis with regards to stress-dependency of the matrix and fractures were performed. This work shows that natural fracture spacing is the most prominent factor affecting shale gas reservoir performance. The work highlights the importance of mechanical squeezing the pore volume by the effective stress to gas recovery. Surface diffusion might be essential for the gas recovery depending on surface diffusivity values. Slip flow and pore diffusion contribute to gas recovery not significantly even though they increase gas apparent permeability under low pressures.

5.2 Introduction

Shale gas gradually becomes the primary supplier of natural gas in the United States with the advancement of hydraulic fracturing in horizontal wells that significantly reduces the operation cost.

During hydraulic fracturing, proppants are pumped into the reservoir to prop open natural fractures in the Stimulated Reservoir Volume (SRV) region. The retained proppants relieve the loss of fracture permeability by the effective stress.[133, 134] In contrast, the unpropped natural fracture outside the SRV region (UNSRV) is more sensitive to the effective stress.

Dynamic properties of fractures and the matrix are required to perform realistic shale gas production simulations. It should be distinguished regarding the matrix and fracture properties as functions of pressure in the simulator.[135] In addition, flow behavior in the matrix is more complicated than that in fractures because some phenomena, such as slip flow and pore diffusion, and high adsorption only occur in nanopores of organic-rich shales.[21] Wasaki and Akkutlu showed that gas flow behavior is different from the liquid in nanopores where diffusion outweighs viscous fluid under low pressures.[136]

Ertekin et al. firstly used the concept of apparent permeability in the matrix by introducing a dynamic slippage factor.[137] Clarkson et al. also used the concept of apparent permeability accounting for the gas slippage and included gas desorption.[138] Cipolla et al. applied the discrete fracture model with focuses on the fracture stress-dependency and gas desorption.[117] They concluded that the fracture treatment is crucial to mitigating the reduced fracture permeability by the effective stress; distinguishing between SRV and UNSRV regions and using laboratory measured properties of fractures and the matrix are essential for reservoir simulations. Huang et al. modeled two-phase flow of water and gas in shales. They reached conclusions that the importance of slip flow depends on reservoir pressure; and the water-wet shale matrix might trap some gas that cannot be recovered.[139]

Considering that including pressure-dependent properties of fractures are relative comprehensive in previous attempts,[140] and little attention has been given to the dynamic properties of the matrix, we attempted to fill this gap in this work. And, based on our previous study about the workflow of estimating shale gas permeability evolution,[11] the objectives of this study are, therefore, (1) include detailed dynamic properties of the matrix and fractures (2) justify the importance of the multiple physics on the matrix to gas production along with the impact of natural fracture spacing (3) perform sensitivity analysis regarding stress-dependency of the matrix and fractures, and surface diffusivity.

5.3 Properties of matrix and fracture

5.3.1 Fracture properties

Figure 5-1 shows an example of fracture conductivity test in propped and unpropped samples as functions of closure stress. Two pieces of important information are obtained that are applied as guidelines of our reservoir simulation (1) the initial fracture conductivity is higher in the propped fracture than the unpropped fracture (2) fracture conductivity loss is relieved because of retained proppants that the unpropped fracture conductivity experiences three orders' magnitude of loss but the propped only experiences one order.

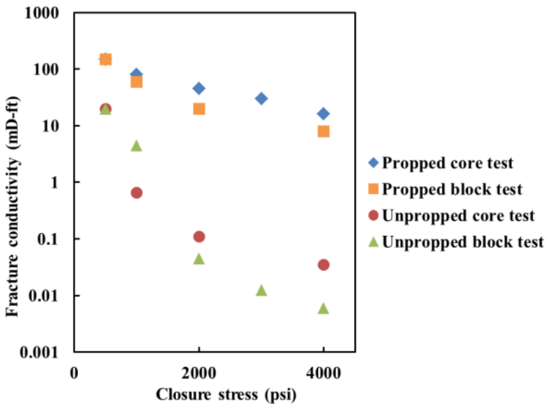

Figure 5-1 Fracture conductivity tests under different closure stress, data from Suarez-Rivera et al.[140]

Figure D1 shows propped fracture normalized effective permeability in two locations of the Marcellus shale with different concentrations of proppant.[142] The permeability under 1000 psi is regarded as the initial point. An exponential relationship is used to fit the experimental data:

$$k = k_0 \exp(-b\sigma_e) \tag{5-1}$$

where k_0 is the initial permeability, σ_e is the effective stress. A larger b value indicates that the fracture is more stress sensitive.

The same equation is used to describe the permeability evolution of unpropped fracture by the shear offset of the Marcellus shale.[143] Fitted results are summarized in Table D1.[144] b value in the unpropped fracture is 1.03E-3 and ranges from 3.6E-4 to 1.49E-3 for propped fractures. Considering the high heterogeneity in shale formations that properties from the two series of tests might differ significantly, and the general fact that propped fracture is less stress-sensitive, b value is set to be 1E-3 for unpropped fractures and vary from 3.5E-4 to 5.5E-4 for propped fractures (Figure 5-2a).

Different fracture surface roughness leads to different fracture porosity.[144] A power-law relationship (Eq. (5-2)) is selected to relate fracture permeability and fracture porosity by ranging the exponent *n* from 3 to 10.[145] Figure 5-2b shows ranges of upper and lower bounds of normalized fracture porosity. Similarly, the effective stress of 1000 psi is the starting point.

$$k / k_0 = (\phi / \phi_0)^n \tag{5-2}$$

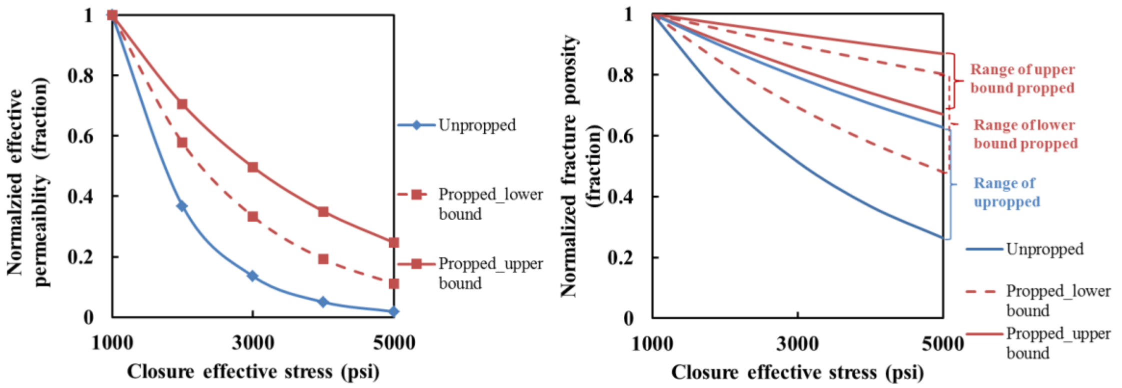

(a) (b)

Figure 5-2 (a) Normalized effective permeabilities and (b) porosity of fractures as functions of closure effective stress for unpropped propped fractures.

5.3.2 Matrix porosity

We only found one set of experimental data of matrix porosity as a function of the effective stress of the Marcellus shale. Considering the high heterogeneity of the shale matrix even in one block, we performed a comprehensive literature survey regarding stress-dependency of shale matrix porosity as recorded in Figure D2. The exponential (Eq. (5-3)) and power- law (Eq. (5-4)) relationships are applied to fit the experimental data:[146-150]

$$\phi = \phi_0 \exp(-m\sigma_e) \tag{5-3}$$

$$\phi = \phi_0 (\sigma_e / \sigma_0)^{-q} \tag{5-4}$$

Obviously, an improved goodness of fit is obtained using the power-law relationship. Table D2 summaries *q* values that range from 7.68E-3 to 1.12E-1. Upper and lower bounds of the normalized matrix porosity with *q* equals to 7.5E-3 to 1.2E-1 are applied in our reservoir simulations (Figure 5-3).

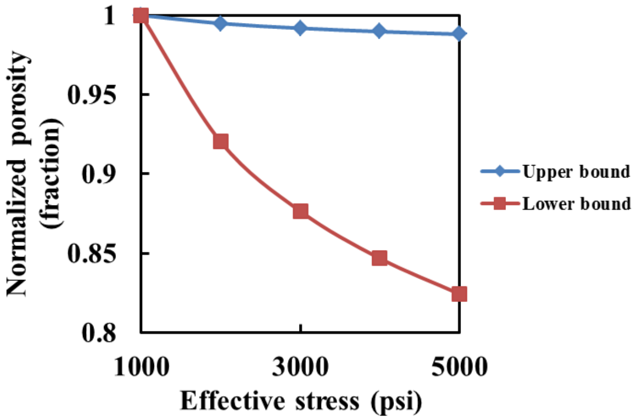

Figure 5-3 Normalized porosity of the matrix with upper and lower bounds that q equals 7.5E-3 and 1.2E-1, respectively.

5.3.3 Matrix permeability

For the matrix permeability, our previous results considering the multiple physics occurred in nanopores are applied,[11] which is based on experimental data conducted on the Marcellus shale. These experimental data include permeability values under different effective stress using the pulse-decay method and methane adsorption capacity of the same shale fitted by Langmuir isotherms.[125, 128]

Figure 5-4 and Figure 5-5 describes the complex physic exerted on the matrix during gas depletion. Gas apparent permeability (k_a) is the product of k_∞ and $f(K_n)$ (Eq. (5-5)) and k_∞ is proportional to the square of pore size (Eq. (5-6)). Kn increases as the reservoir pressure decreases. The increase of effective stress and gas desorption occur simultaneously as gas depletes, causing the pore size to decrease and increase, respectively. Pore size increase directly causes k_∞ to increase and pore size decrease causes k_∞ to decrease. On the other hand, pore size increase induces Kn decrease, and consequently, $f(Kn)$ decreases, which is unfavorable to the gas permeability. Similarly, the decrease of pore size indirectly leads to $f(Kn)$ increase, which is favorable to the gas permeability. Based on our analysis, the adsorption-induced surface diffusion component continues to increase during the lifetime of a gas well. However, whether the net effect is positive or negative is not certain that one needs to perform a detailed gas production simulation.

$$k_a = k_\infty \times f(Kn) \tag{5-5}$$

$$k_\infty \propto d^2 \tag{5-6}$$

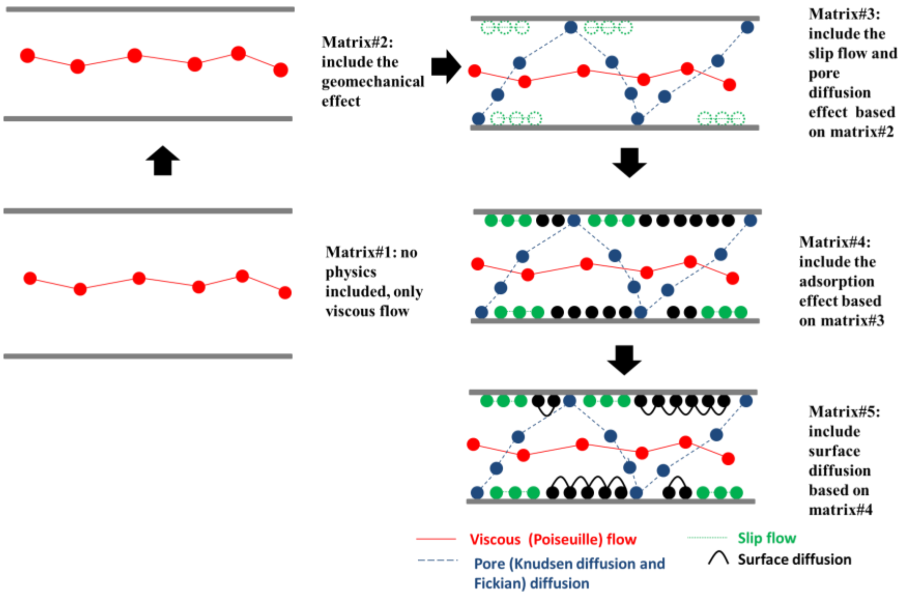

Figure 5-4 Four steps to take into account the multiphysics exerted on the matrix (modified from Jia et al.[11]). Molecules connected by lines (solid and dashed) indicate the flow path traveled by one molecule with time. Note: The schematic drawn here belongs to a specific size range of pores which is a good representative of our current shale gas/oil systems (0.01-1 µm).

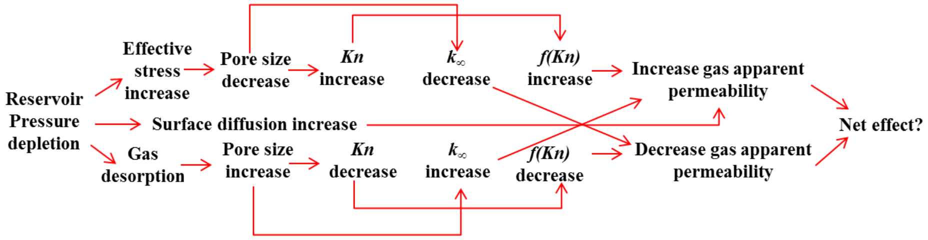

Figure 5-5 Change of k_∞ and *f(Kn)* during pressure depletion of gas production.

The pore size, *d*, is needed to calculate *Kn*. Heller et al. estimated the pore size from the Klinkenberg equation:[12]

$$k_a = k_\infty \left(1 + \frac{K_b}{p}\right) \tag{5-7}$$

By expressing the total flux as the summation of the Poiseuille flow and Knudsen flow, the apparent permeability can be expressed as:[125]

$$k_a = \frac{d^2}{12A}\left[1+\frac{16c\mu}{dp}(\frac{2RT}{\pi M})^{1/2}\right] \tag{5-8}$$

where *A* is the flow cross-section area. Therefore, the pore size can be estimated as:

$$d = \frac{16c\mu}{K_b}(\frac{2RT}{\pi M})^{1/2} \tag{5-9}$$

Practically, a series of permeability measurements as a function of 1/*p* are needed to estimate the pore size along with gas properties under the average flowing pressure.

Correlations between *Kn* and *f(Kn)* in different flow regimes by Sakhaee-Pour and Bryant are used to take into account of slip flow and pore diffusion,[10] which includes Knudsen diffusion and Fickian diffusion. Eq. (5-10) provides the correlation in the slip-flow regime that *Kn* ranges from 10^{-3} to 0.1, and Eq. (5-11) provides the correlation in the transition flow regime that *Kn* ranges from 0.1 to 10.

$$f(K_n) = \frac{k_g}{k_\infty} = 1+\alpha_1 K_n \tag{5-10}$$

$$f(K_n) = \frac{k_g}{k_\infty} = 0.8453+5.4576K_n+0.1633K_n^2 \tag{5-11}$$

In our previous work,[11] four steps were devised to investigate the evolution of gas permeability during gas production. The effective stress reducing the pore size is evaluated at the first step. Slip flow and pore diffusion are evaluated at the second step. Adsorption layer is evaluated at the third step and surface diffusion is evaluated at the last step (Figure 5-4). Akkutlu and Fathi matched upstream pressure curves of pulse-decay experiments by a non-linear history matching algorithm to obtain the surface diffusivity values.[30] They reported surface diffusivity values ranging from 5.1E-8 m^2/s to 8.8E-6 m^2/s from 10 pulse-decay experiments in 3 core samples.

Based on their values, we vary surface diffusivity form 1E-8 m^2/s to 1E-5 m^2/s in reservoir simulations.

Based on the procedures described in Figure 5-4, five matrix settings are generated as described in Table 5-1. Figure 5-6a shows the five permeability curves with different matrix settings, from the initial effective stress of 1000 psi to 4960 psi, corresponding to the initial reservoir pressure of 4000 psi to 40 psi. In matrix#1, permeability is a constant of 65 nD. In matrix#2, the effective stress causes 90% of permeability loss at the end of production. In matrix#3, slip flow and pore diffusion enhance gas permeability significantly at low reservoir pressures. The apparent permeability starts to increase at a turning point of approximately 500 psi at which slip flow and pore diffusion begin to outweigh the effective stress. In matrix#4, the volume occupied by the adsorption layer is taken into account, the net effect of which on permeability is also negative, like the effective stress. However, the effect is limited because the gas molecule size is still small compared with the pore size in our study, which can be expected to be larger in a pore with the initial pore size smaller than 10 nm. In matrix#5, surface diffusion is taken into account and Figure 5-6(b) shows surface diffusivity dependent permeability curves. Like slip flow and pore diffusion, surface diffusion is also favorable to gas apparent permeability, and its impact depends on the value of surface diffusivity. When surface diffusivity is smaller than 1E-6 m^2/s, a turning pressure point is observed wherein the permeability starts to increase when pressure decreases. If surface diffusivity is larger than a critical value (between 1E-6 m^2/s and 1E-5 m^2/s), this turning point disappears, and gas apparent permeability will increase throughout the production process.

Table 5-1 Properties of different matrix settings.

Matrix#1	Properties constant during gas depletion
Matrix#2	Consider the effective stress
Matrix#3	Consider the effective stress and slip flow/pore diffusion
Matrix#4	Consider the effective stress, slip flow/pore diffusion and adsorption/desorption
Matrix#5	Consider the effective stress, slip flow/pore diffusion, adsorption/desorption, and surface diffusion

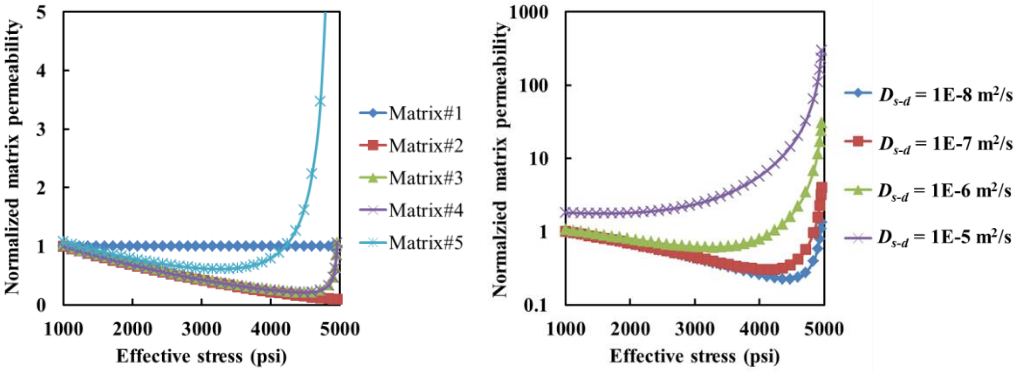

(a) (b)

Figure 5-6 (a) Normalized permeability evolution in different matrix settings (b) after taking account into surface diffusion with different values of surface diffusivity.

5.4 Reservoir model settings

Table 5-2 lists basic parameters in the reservoir model with dual permeability. Figure 5-7 shows the hydraulic fracture, SRV and UNSRV regions in the reservoir. A one-stage fractured horizontal well is placed in the center of the reservoir with no flow boundary conditions. The SRV region accounts for 23% of the total reservoir volume. The initial conductivity of the hydraulic fracture is 200 mD·ft. Normalized porosity and permeability of uncropped fractures in Figure 5-2 are used to describe properties of unpropped natural fractures in the UNSRV region, while normalized porosity and permeability of propped fractures are used to describe properties of propped fractures in the SRV region. The SRV region is distinguished from the UNSRV region by setting the initial effective permeability and effective porosity of fractures as 5 times that in the UNSRV region.

Table 5-2 Basic reservoir settings.

Reservoir temperature (°F)	130	Langmuir pressure (psi)	741.5
Initial reservoir pressure (psi)	4000	Langmuir adsorption maximum (scf/ton)	196.4
Depth (ft)	5000	Water saturation (%)	0
Closure pressure gradient (psi/ft)	1	Matrix initial porosity (fraction)	0.05
Grid size (ft)	10×10×10	Matrix initial permeability (nD)	65
Grid number	63×31×5	Initial effective stress (psi)	1,000

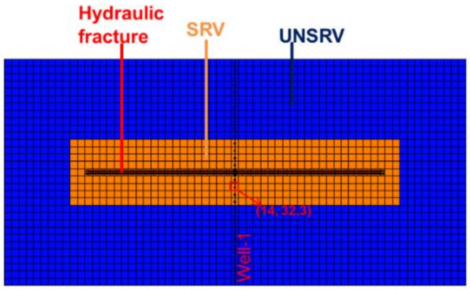

Figure 5-7 Hydraulic fracture, SRV and UNSRV regions in a single-stage fractured horizontal well. Fractures in the UNSRV region and SRV region are more stress-dependent and less stress-dependent, respectively.

The dual permeability model implemented in this study is developed into numerical schemes for flow in fractured reservoirs.[143] Figure 5-8a depicts flow connections between the matrix and fractures. Figure 5-8b shows the volume of natural fracture in a grid cell conceptually. This model accounts for three types of flow connections: from fracture to fracture; from fracture to the matrix, and from the matrix to matrix. Concepts of effective permeability (k_{eff}) and effective porosity (ϕ_{eff}) in the simulator are defined as:

$$k_{eff} = \frac{2k_{nf}W_{nf}}{D_f} \tag{5-12}$$

$$\phi_{eff} = \frac{3W_{nf}}{D_f} \tag{5-13}$$

where k_{nf}, w_{nf}, D_f are intrinsic permeability, width and natural fracture spacing, respectively. If we assume the intrinsic conductivity of the unpropped natural fracture is 1E-3 mD·ft, the effective permeability and porosity with different fracture spacing can be calculated (Table 5-3).

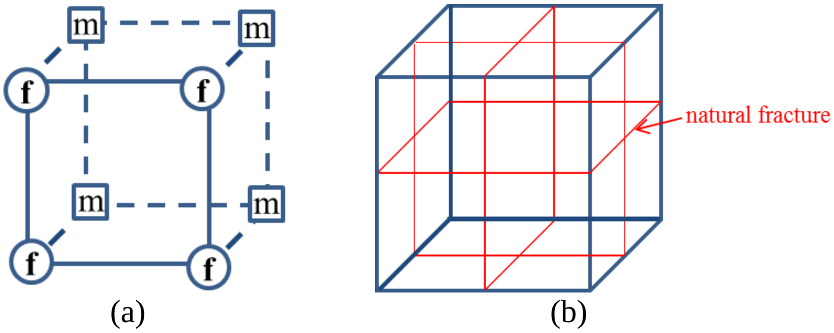

(a) (b)

Figure 5-8 (a) Flowing connections in the dual-permeability model, modified from Wu (2015), f represents fracture and m represents matrix (b) conceptual schematic shows the volume of natural fracture occupied in a grid cell.[108]

Table 5-3 Effective permeability and porosity with different natural fracture spacings.

Natural fracture spacing (ft)	Effective permeability (mD)	Effective porosity (fraction)
5	4.0E-04	6.0E-04
10	2.0E-04	3.0E-04
20	1.0E-04	1.5E-04
50	4.0E-05	6.0E-05

Table 5-4 summarizes simulation scenarios that will be performed. Besides the matrix settings, fracture spacing, stress dependency of the matrix and fractures, and the minimum BHP ranging from 50 psi to 2000 psi are also investigated. Reservoir setting with shorter fracture spacing and a lower BHP is expected to lead to faster gas production. Gas production simulation lasts for 5 years and the criterion of the choosing the range of fracture spacing and minimum BHP is that the cumulative gas production does not reach a plateau at the end of 5 years to compare gas recovery factor. Otherwise, the comparison is meaningless. It is recognized that the BHP rarely drops to such a low pressure as 50 psi. However, in a real field, the well operator always tries to keep the BHP as low as possible without pumping off the well, and this study covered a wide range of to provide a comprehensive evaluation.

Table 5-4 Simulations scenarios.

Matrix permeability	Natural fracture spacing (ft)	Minimum BHP (psi)	Matrix porosity	Fracture porosity	Propped fracture permeability
Matrix#1 Matrix#2 Matrix#3 Matrix#4 Matrix#5	5 10 20 50	50 500 1000 2000	Less/more stress dependent	Less/more stress dependent	Less/more stress dependent

5.5 Results and discussions

Gas production lasts for 5 years with a constant minimum BHP. Figure 5-9 shows field gas recovery at the end of 5 years as a function of natural fracture spacing. Figure 5-9a, b, c, and d show results with minimum BHPs of 50 psi, 500 psi, 1000 psi and 2000 psi, respectively, when surface diffusivity is 1E-6 m^2/s. Overall, a higher recovery is obtained at a lower BHP because a larger drawdown pressure leads to a higher depletion rate. The final gas recovery factor drops from averagely 15% to 10% as the BHP increases from 50 psi to 2000 psi. At a given BHP, natural fracture spacing is the dominant factor in all matrix settings. Differences between the other four settings and matrix#5 which considers the full physics, regarded as errors (Eq. (5-14)), are shown in Figure 5-10.

$$Error = \frac{matrix\#X - matrix\#5}{matrix\#5}$$

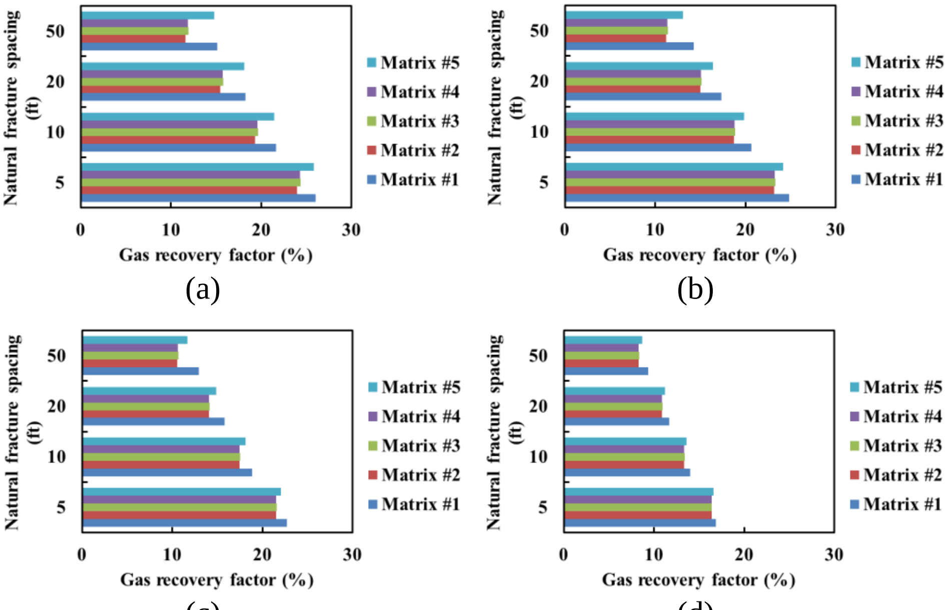

(a) (b)

(c) (d)

Figure 5-9 Field gas recovery factors after producing for 5 years.

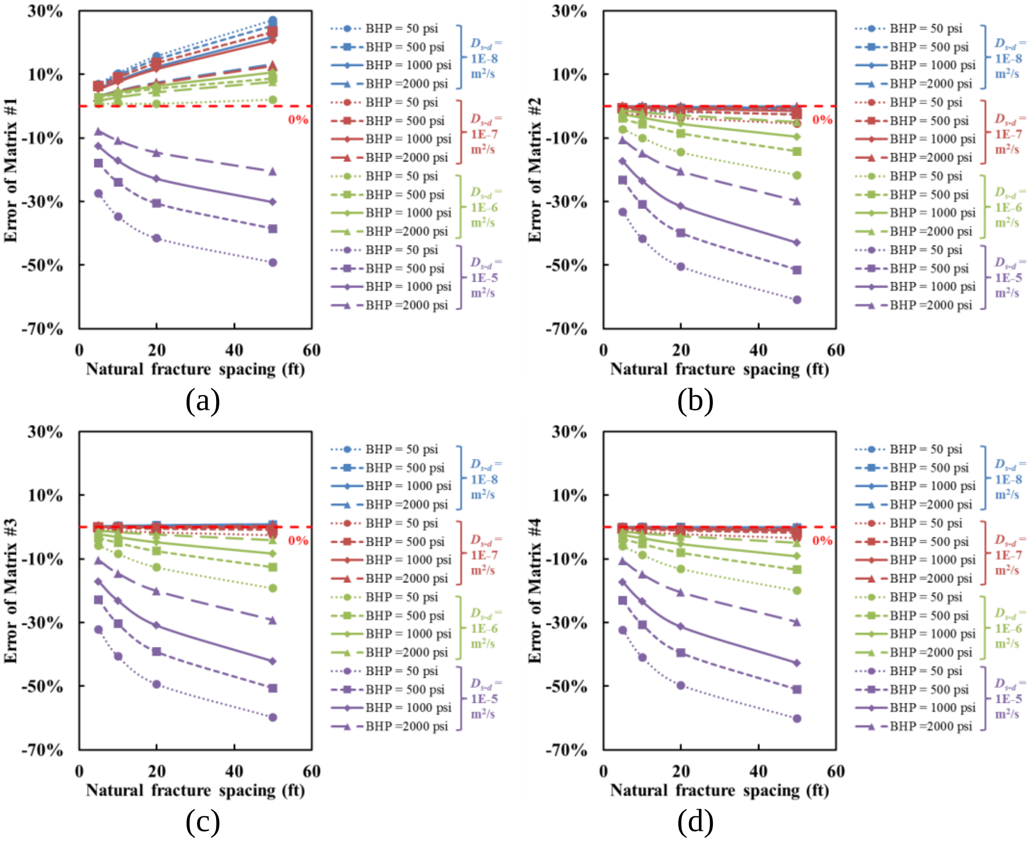

(a) (b)

(c) (d)

Figure 5-10 Gas recovery errors by comparing (a) matrix#1 (b) matrix#2 (c) marix#3 (d) matrix#4, and matrix#5 which takes full physics into account.

A positive error indicates gas production is overestimated while a negative error indicates gas production is underestimated. A red dashed line is drawn at the 0% error to separate positive and negative zones. Afterward, simulation results with more stress dependent matrix and fractures are compared.

5.5.1 Impact of effective stress on the matrix

None of the physics mentioned is included in matrix#1. Porosity and permeability changes by the effective stress are included in matrix#2 to couple with fluid flow. Therefore, the impact of effective stress can be revealed by comparing Figure 5-10a and Figure 5-10b. Pore compaction by effective stress has two effects. On one hand, pore compaction squeezes gas from nanopores to fractures to favor gas production. On the other hand, pore compaction reduces matrix permeability and porosity, hampering flow within the matrix and from the matrix to fractures, which is unfavorable for gas production.

Figure 5-10a shows that the gas recovery factor is overestimated with matrix#1 in all simulation scenarios if no physics in the matrix is considered unless the surface diffusivity is 1E-5 m^2/s. Errors increase as the natural fracture spacing increases. After taking into the effective stress, all curves move down that the errors become negative, indicating that the net effect of pore compaction is unfavorable for gas production.

We use distributions of matrix porosity and permeability, and effective permeability of fractures at the end of 5 years to explain the unfavorable net effect of pore compaction. Figure 5-11 compares distributions of these properties with matrix#1 and matrix#2, respectively, when the well is operated with the minimum BHP of 50 psi and the natural fracture spacing is 20 ft. Pressure distributions are similar in most parts of reservoirs, but matrix#2 scenario shows higher pressures near the wellbore region, implying a lower gas recovery. In terms of matrix porosity and permeability of matrix#2, the lowest porosity drops to 4.9% from the original 5% and the lowest permeability drops to 10 nD from the original 65 nD. In addition, the retained effective permeability of fractures is higher with matrix#2 near the wellbore because the reservoir is less depleted. Therefore, gas production is lower because of pore compaction near the wellbore region, which is more severe when the well is operated with a low BHP.

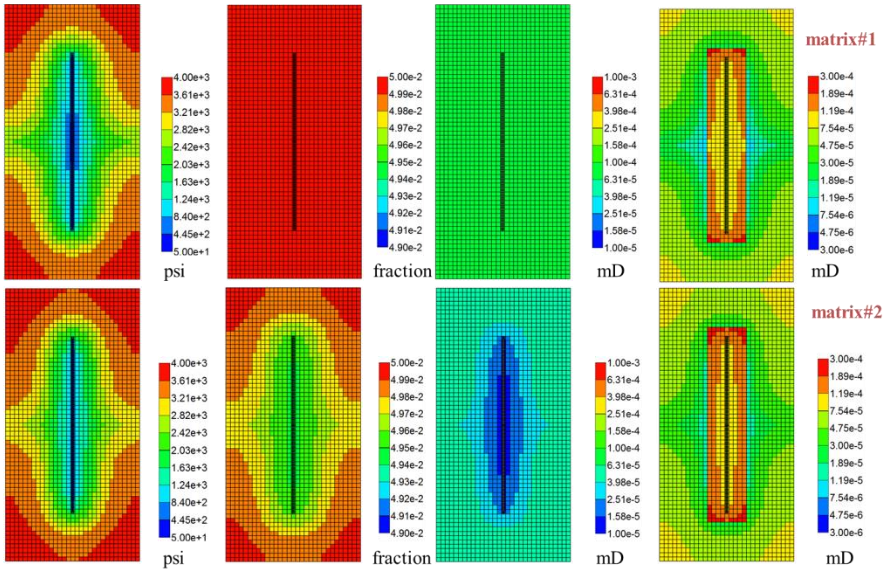

(a) (b) (c) (d)

Figure 5-11 Distributions of (a) pressure (b) matrix porosity (c) matrix permeability (d) effective fracture permeability after 5 years with matrix#1 and matrix#2.

5.5.2 Impact of slip flow/pore diffusion

Slip flow and pore diffusion are included in matrix#3 in addition to the effective stress. Impacts of slip flow and pore diffusion can be evaluated by comparing Figure 5-10b and Figure 5-10c. Although it is observed that slip flow and pore diffusion enhance the apparent permeability, whether or not their contribution to the gas production volume is significant is not certain because they only play roles under low pressures. No obvious change is observed between Figure 5-10b and Figure 5-10c, indicating that slip flow and pore diffusion contribute to gas recovery negligibly compared with the effective stress.

Figure 5-12 shows matrix permeability evolutions at the grid of (14,32,3) (pointed out in Figure 5-7) with matrix#2 and matrix#3. The permeability starts to increase after 6817 days with matrix#3 at about 500 psi in accordance with the permeability curve in Figure 5-6, which is an indication that slip flow and pore diffusion begin to play a role under low reservoir pressures. However, in real field practice, shale gas reservoirs are only economically productive for 2-4 years and after that, refracturing has to be applied. Therefore, it implies that the importance of slip flow and pore diffusion are limited because before they play a role, the well has ceased to produce.

5.5.3 Impact of adsorption/desorption

Adsorption/desorption's impact on influencing matrix permeability is included in matrix#4. The impact can be evaluated by comparing Figure 5-10c and Figure 5-10d. The adsorption layer reduces the effective pore size by occupying volume on the pore surface, but the pore size reduction is limited: pore size reduces from 45.33 nm to 13.65 nm as the effective stress increases from 1000 psi to 4960 psi without considering adsorption, and from 44.57 nm to 12.89 nm considering adsorption. Figure 5-6 shows that permeability curve with matrix#4 is slightly lower than that with matrix#3 which is not very obvious as it has been normalized. As a result, one would expect the adsorption layer would reduce gas production slightly. Results show that the adsorption is indeed unfavorable for gas production but the effect is negligible because there is no obvious difference between Figure 5-10c and Figure 5-10d.

Even though the adsorption layer affects gas production in terms of influencing matrix permeability, it is essential to gas production because it significantly increases Original Gas in Place (OGIP). Table 5-5 shows gas volume in place in different forms. In the matrix, gas volume percentage by the adsorption phase is 51.0% in all scenarios. In the fracture, gas volume slightly decreases as the natural fracture spacing increases. However, even when the fracture spacing is as short as 5 ft, gas volume in the fracture only accounts for 1.1% of OGIP.

Table 5-5 Gas volume in place (std. ft^3).

Natural fracture spacing (ft)	OGIP	Adsorption	Matrix	Fracture	Adsorption/matrix	Matrix/OGIP
5	2.67E+08	1.35E+08	2.64E+08	2.84E+06	50.99%	98.93%
10	2.65E+08	1.35E+08	2.64E+08	1.42E+06	50.99%	99.46%
20	2.65E+08	1.35E+08	2.64E+08	7.11E+05	50.99%	99.73%
50	2.64E+08	1.35E+08	2.64E+08	2.84E+05	50.99%	99.89%

5.5.4 Impact of surface diffusion

Surface diffusion is included in matrix#5. The impact of surface diffusion can be evaluated by Figure 5-10d. Approximately, errors of production forecast are 0.1%, 1%, 5%, and 30% when surface diffusivity equals 1E-8 m^2/s, 1E-7 m^2/s, 1E-6 m^2/s, and 1E-5 m^2/s, respectively. The error increases as the natural fracture spacing increases because surface diffusion only occurs in the matrix. Also, the error increases with a lower BHP because surface diffusion is more important under lower pressures, and a longer natural fracture spacing because gas volume is larger in the matrix.

Figure 5-12 shows matrix permeability evolutions at the grid of (14,32,3) with matrix#4 and matrix#5. With matrix#4, permeability begins to increase after 6970 days. Permeability curves with matrix#5 experiences shorter periods of decline as the surface diffusivity increases. Permeability begins to increase after 6755 days, 1612 days, and 181 days when the surface diffusivity equals 1E-8 m^2/s, 1E-7 m^2/s, and 1E-6 m^2/s, respectively (Figure 5-13). When surface diffusivity is 1E-5 m^2/s, no permeability decline is experienced and the magnitude of permeability is almost two orders higher than that with 1E-6 m^2/s. Results imply that the permeability enhancement would relieve the intrinsic permeability loss by the effective stress but the degree of enhancement largely depends on the magnitude of surface diffusivity, and there is a quantitative change between 1E-6 m^2/s and 1E-5 m^2/s.

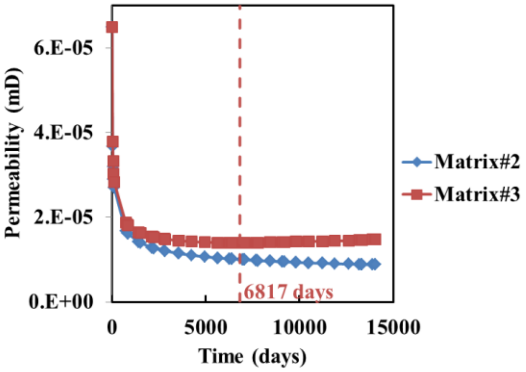

Figure 5-12 Matrix permeability evolution at the grid of (14,32,3) with matrix#2 and matrix#3.

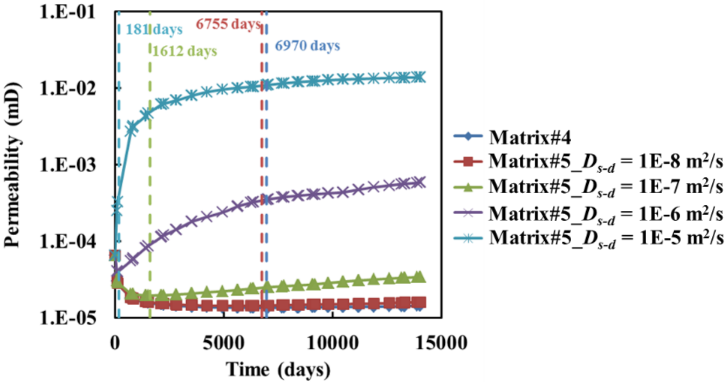

Figure 5-13 Matrix permeability evolution at the grid of (14,32,3) with matrix#4 and matrix#5.

5.6 Sensitivity analysis of stress dependency

Considering heterogeneity of shale reservoirs and different hydraulic fracturing processes prop open natural fractures to different degrees depending on frac pumping technologies and propping agents. Sensitivity analysis was performed regarding stress-dependency of rock properties. Aspects investigated include matrix porosity, permeability of propped fractures and porosity of fractures. Figure 5-14a shows gas recovery factors using the lower bound of the matrix porosity curve present in Figure 3. Figure 5-14b shows gas recovery factors using the upper bound of propped fracture permeability curve present in Figure 5-2. Figure 5-14 shows gas recovery factors using lower bounds of fracture porosity for both unpropped and propped fracture present in Figure 5-2.

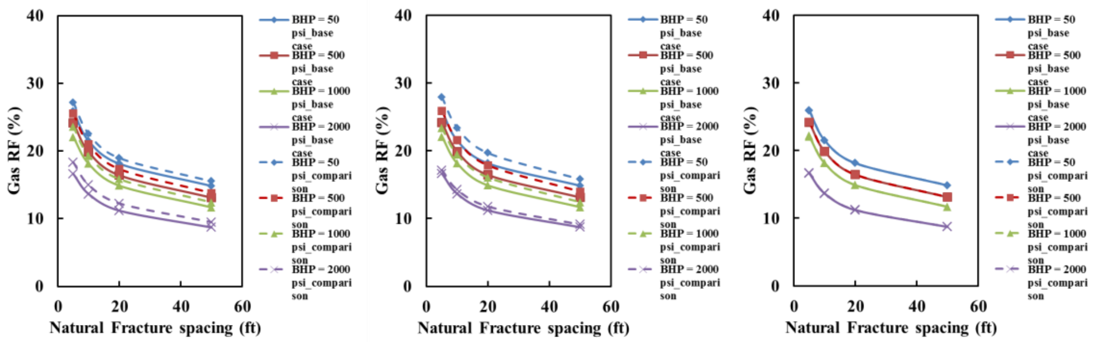

(a) (b) (c)

Figure 5-14 Gas recovery factors with (a) more stress-dependent matrix porosity (b) less stress-dependent permeability of propped fractures (c) more stress-dependent porosity of fractures.

5.6.1 Sensitivity of stress-dependency of matrix porosity

The net effect of pore compaction has two outcomes: reduction of matrix porosity and matrix permeability. Impairment of transport capacity arises from the reduction of both matrix porosity and matrix permeability. However, the matrix porosity reduction also has a beneficial side to gas production because of the mechanical squeezing effect. Therefore, the net effect of matrix porosity reduction is uncertain. Figure 5-14a shows that simulation scenarios using more stress-dependent matrix porosity achieve higher gas recovery, indicating the net effect of matrix porosity reduction is positive to gas recovery. Given the fact that the net effect of pore compaction is unfavorable to gas recovery, we can infer that the matrix permeability rather than the matrix porosity reduction is the cause of unfavorable impact on gas production.

5.6.2 Sensitivity of stress-dependency of fractures

Less stress-dependent propped fractures refers to that proppants with more mechanical strength are applied to hold propped fractures open to withstand the closure effective stress. Figure 5-14b shows that less stress-dependent SRV region leads to a higher gas recovery, implying the importance of improving efficiency of hydraulic fracturing that includes selection of proppants with high crush strength and fracturing fluids with excellent proppant carrying capacity.

Fracture porosity arises from the roughness on the surface.[113] Eq. (5-2) uses n to characterize the relationship between fracture permeability and fracture porosity considering different surface roughness. Contrary to the intuition, Figure 5-14c shows that more stress-dependent fracture porosity does not affect the gas recovery performance. The reason is that gas volume in fractures only accounts for 1.1% of OGIP (Table 5-5). Therefore the mechanical squeezing effect is negligible, unlike the matrix porosity; fracture permeability rather than fracture porosity contributes to the flow capacity in shale reservoirs. The reason is that as fracture porosity decreases, the increased gas storage in the matrix compensates for the loss in the fracture conductivity.

5.7 Conclusions

In this work, the importance of multiple physics exerted on the matrix for shale gas recovery is justified by performing a series of production simulations. Our study highlights the importance of natural fracture spacing, effective stress and surface diffusion for gas recovery. The detailed conclusions are as follows.

The effective stress exerted on the shale matrix reduces pore volume in nanopores, improving the transport of gas out of the matrix and into fractures and finally the wellbore, which is a favorable mechanism for gas production. However, the net impact of effective stress on the shale matrix is unfavorable for gas production because of matrix permeability impairment.

Though it is observed that matrix permeability impairment is mitigated by slip flow and pore diffusion under low pressures, the enhancement of gas production due to the mitigation is limited because most shale wells ceased to produce before slip flow and pore diffusion plays a role.

Gas adsorption is a major component of OGIP; the percentage is 51% in our simulations. However, the impact of the adsorption layer influencing matrix permeability on gas production is limited.

Forecast errors of 5-year shale gas production without considering surface diffusion are 0.1%, 1%, 5%, 30% when surface diffusivity is 1E-8 m^2/s, 1E-7 m^2/s, 1E-6 m^2/s, and 1E-5 m^2/s, respectively. Therefore, it is crucial to obtain accurate surface diffusivity in organic-rich shales.

Natural fracture spacing outweighs multiple physics on the shale matrix in influencing shale gas recovery. Improved hydraulic fracturing efficiency with high mechanical strength proppants help transport gas from nanopores to the wellbore, facilitating gas production. Furthermore, fracture permeability is essential for shale gas production performance, but fracture porosity is not.

5.8 Nomenclature

A	Flow cross-section area, m^2
b	Fitting parameter in Eq. (5-1), 1/psi
c	Gas compressibility, 1/psi or 1/Pa
d	Pore size, nm/m/ft
D_f	Fracture spacing, ft
D_{s-d}	Surface diffusivity, m^2/s
k	Permeability, nD
k_0	Initial permeability, nD
k_∞	Intrinsic permeability, nD

k_a	Apparent permeability, nD or m^2
K_b	Klinkenberg constant, psi
k_{eff}	Effective permeability, nD
Kn	Knudsen number, dimensionless
k_{nf}	Natural fracture permeability, mD
M	Molecular weight in Eq. (5-8) and Eq. (5-9), g/moL
m	Fitting parameter in Eq. (5-3), 1/psi
n	Exponent in Eq. (5-2), dimensionless
p	Pressure, psi or Pa
q	Fitting parameter in Eq. (5-4), dimensionless
R	Gas constant, 8.314 J/(mol·K)
T	Temperature, K
W_{nf}	Natural fracture width, ft
μ	Viscosity, cP or Pa·s
σ_e	Effective stress, psi
ϕ	Porosity, dimensionless
ϕ_0	Initial porosity, dimensionless
ϕ_{eff}	Effective porosity, dimensionless

Summary

This dissertation focused on investigating shale gas flow behavior using experimental and numerical approaches. New insights have been provided to understand the complex flow behavior in organic-rich shales and its implications deeply. Specially, pulse-decay experiments have been performed on both unfractured and fractured core samples; both analytical and numerical approached have been employed to interpret petrophysical properties of shales. In addition, a workflow is constructed to couple several physics in the routine shale core analysis to provide a permeability evolution curve to be used in shale gas production simulations. The specific contributions of this dissertation are as follows.

Three types of porosity and three types of permeability are investigated in terms of behavior of different gases. The three different types of porosity are intrinsic porosity, apparent porosity, and porosity (ϕ_{app}) applied in the flow equation. Three types of permeability are intrinsic permeability, apparent permeability including adsorption effect, and apparent permeability excluding adsorption effect. Apparent porosity is different from the intrinsic porosity when adsorption is present: apparent porosity is $(1 + Da)$ times than the intrinsic porosity, where Da is the density ratio between the adsorbed phase and free gas phase. Two types of adsorption, Gibbs/excess adsorption and absolute adsorption, need to be differentiated that the Gibbs/excess one should be applied in the governing equation for adsorptive gas. Helium apparent permeability is higher than nitrogen and carbon dioxide, which is in accordance with trends of Knudsen number. The apparent porosity, ϕ_{app}, which is $(1 + Ka)$ times the intrinsic porosity, should be applied in the formula of the approximate analytical solution to estimate apparent permeability, where Ka is termed as the differential partition coefficient which is different from Da. Ka can be used to evaluate the contribution of adsorption to permeability.

A 2D finite-element based model is constructed to model the transient flow process during the pulse-decay experiment. Factors of fractures influencing transient flow behavior include location, orientation, and length, The concept of effective permeability is put forward to analyze the contribution of complex configuration to the flow behavior. By comparing the effective permeability in the steady-state and transient flow processes, it is found that the transient flow process depends on flow direction but the steady-state process does not if the core sample is heterogeneous. During the pulse-decay experiments, a dual porosity region might be formed if the fracture network penetrates the core sample, causing the downstream pressure first increase then decrease. Based on the history matching of upstream and downstream pressure profiles on the fractured core, it is found that the matrix permeability is more sensitive to the pore pressure and effective stress than the matrix porosity, fracture porosity, and fracture permeability. Pressure curves are successfully matched for the total 59 experiments on the fractured core with the error less than 0.2%. Based on the history matching error of the experimental pressure curves, it is found that there is a trend of decreasing as the pore pressure increases, implying a fact that fluid flow is more likely in a homogeneous porous media under higher pressure.

A workflow to estimate shale gas permeability curve is proposed to be used in the routine shale gas reservoir modeling. Experimental data required to obtain such a curve include pore size change a function of effective stress, adsorption profiles, and surface diffusivity. The pore size change is used to forecast intrinsic permeability change as a function of effective stress. Empirical correlations by Sakauepour and Bryant are applied to include the effect of slip flow and pore diffusion. The adsorption profile is used to obtain the effective pore size because of the adsorption layer. The flux of surface diffusion with surface diffusivity ranging from 1E-8 m2/s to 1E-5 m2/s is added to the total flux to obtain the final apparent permeability. The results indicate that the effective stress causes permeability loss of about 90% at the end of gas production. Due to slip flow and pore diffusion, permeability loss is mitigated especially under low pore pressure. At the pore pressure approximately 500 psi, apparent permeability begins to increase as pore pressure continues to decrease. The adsorption layer effect of influencing flow behavior is negligible when the pore size range is 13.65 nm to 45.63 nm, and higher when the pore size range is 3.41 nm to 11.33 nm. Surface diffusion might enhance apparent permeability and the enhancement level depends on the magnitude of surface diffusivity. There is a threshold value between 1E-6 m^2/s to 1E-5 m^2/s that apparent permeability monotonically increases as the pore pressure decreases or the effective stress increases.

It is observed that slip flow, pore diffusion, and surface diffusion indeed relieve the negative impact of effective stress on flow capacity impairment. However, whether or not they affect shale gas production noticeably as well is uncertain because of two reasons: shale gas wells seldom reach low pressure under 500 psi when these effects literally play roles, and gas density is low under low pressures. Shale gas production simulations need to take into account the dynamic properties of both the matrix and fractures. A single-stage hydraulic fractured horizontal well is placed in the reservoir. Permeability evolution curves developed for the matrix in chapter 4 are used. Lower and upper bounds of porosity evolution curves are applied to test the sensitivity of pore compaction effect. Experimental results of natural fracture with and without embedded proppants are applied for the propped fractures and unpropped fractures, respectively. Lower and upper bounds of fracture permeability can be used to test the sensitivity of the proppant crushing strength. Different simulation scenarios include setting the bottom hole pressure, natural fracture spacing and surface diffusivity. The results indicate that the net impact of pore compaction, which results in both porosity and intrinsic permeability decreases, is negative for gas production.

However, the squeezing effect from the porosity reduction is favorable to increase gas production. Slip flow, pore diffusion, and the adsorption layer affect gas production negligibly even when the bottom hole pressure is operated with 50 psi. Production forecast errors after 5 years are 0.1%, 1%, 5%, and 30% when surface diffusivity equals 1E-8 m^2/s, 1E-7 m^2/s, 1E-6 m^2/s, and 1E-5 m^2/s, respectively. The results imply that as long as surface diffusivity is smaller than 1E-6 m^2/s, surface diffusion effect can be ignored for engineering applications.

References

1. Brace, W. F.; Walsh, J. B.; Frangos, W. T., Permeability of granite under high pressure. *Journal of Geophysical Research* **1968**, *73* (6), 2225-2236.

2. Sutherland, H. J.; Cave, S. P., Argon gas permeability of New Mexico rock salt under hydrostatic compression. *International Journal of Rock Mechanics and Mining Sciences* **1980**, *17*, 281-287.

3. Lin, W., Compressible fluid flow through rocks of variable permeability. *Lawrence Livermore Laboratory, Livermore, California*. **1977**.

4. Hsieh, P. A.; Tracy, J. V.; Neuzil, C.E.; Bredehoeft, J. D.; Silliman, S. E., A transient laboratory method for determining the hydraulic properties of 'tight' rocks—I. theory. *International Journal of Rock Mechanics and Mining Sciences & Geomechanics Abstracts* **1981**, *18* (3), 245-252.

5. Dicker, A. I.; Smits, R. M., A practical approach for determining permeability from laboratory pressure-pulse decay measurements, International Meeting on Petroleum Engineering **1988**, 1-4 November. SPE-17578-MS.

6. Cui, X.; Bustin, A. M. M.; Bustin, R. M., Measurements of gas permeability and diffusivity of tight reservoir rocks: different approaches and their applications. *Geofluids* **2009**, *9* (3), 208-223.

7. Ivanov, M. S.; Bondar, Y. A.; Markelov, G. N., Recent achievements in the DSMC method and its applications to studying jets in vacuum chamber. 51st IUVSTA Workshop on Modern Problems & Capability of Vacuum Gas Dynamics **2007**.

8. Mason, E. A.; Malinauskas, A. P., Gas transport in porous media: the Dusty-Gas model (Chemical Engineering Monographs), Elsevier Science **1983**.

9. Karniadakis, G.; Beskok, A.; Aluru, N., Microflows and nanoflows: fundamentals and simulation. Springer **2005.**

10. Sakhaee-Pour, A.; Bryant S. Gas permeability of shale. *SPE Reservoir Evaluation & Engineering* **2012**, *15* (4), 401-409.

11. Jia, B.; Tsau, J.; Barati, R., A workflow to estimate shale gas permeability variations during the production process. *Fuel* **2018**, *220*, 879-889.

12. Klinkenberg, L. J., The permeability of porous media to liquids and gases. Drilling and Production Practice. **1941**.

13. Heid, J. G.; McMahon, J. J.; Nielsen, R. F.; Yuster, S. T., Study of the Permeability of Rocks to Homogeneous Fluids. American Petroleum Institute. **1950**.

14 Jones, F. O.; Owens, W. W., A laboratory study of low-permeability gas sands. *Journal of Petroleum Technology* **1980**, 1631–1640.

15. Sampath, K.; Keighin, C. W., Factors affecting gas slippage in tight sandstones. *Journal of Petroleum Technology* **1981**, *34* (11), 2715-2720.

16. Florence, F. A.; Rushing, J. A.; Newsham, K. E.; Blasingame, T. A., Improved permeability prediction relations for low permeability sands. SPE Rocky Mountain Oil and Gas Technology Symposium **2007**, 16-18 April. SPE-107954-MS.

17. Civan, F., Effective Correlation of apparent gas permeability in tight porous media. *Transport in Porous Media* **2010**, *82* (2), 375-384.

18. Beskok, A.; Karniadakis, G. E., A model for flows in channels, pipes, and ducts at micro and nano scales. *Nano-scale Microscale Thermophysical Engineering* **1999**, *3* (1), 43-77.

19. Loyalka S. K.; Hamoodi S. A., Poiseuille flow of a rarefied gas in a cylindrical tube: solution of linearized Boltzmann equation. *Physics of Fluids A* **1990**, *2* (11), 2061–2065.

20. Tison, S.A.; Tilford, C.R., Low density water vapor measurements, The NIST Primary Standard and Instrument Response, NIST Internal Report 5241. **1993**.

21. Javadpour, F., Nanopores and apparent permeability of gas flow in mudrocks (shales and siltstone). *Journal of Canadian Petroleum Technology* **2009**, *48* (8). 16-21.

22. Roy, S.; Raju, R.; Chuang, H. F.; Cruden, B. A., Meyyappan, M., Modeling Gas flow through microchannels and nanopores; *Journal of Applied Physics* **2003**, *93* (8), 4870-4879.

23. Wu, K.; Li, X.; Guo, C.; Wang, C.; Chen, Z., A Unified Model for Gas Transfer in Nanopores of Shale-Gas Reservoirs: Coupling Pore Diffusion and Surface Diffusion. *SPE Journal* **2016** *21* (5), 1583-1611.

24. Zhai, Z.; Wang, X.; Jin, X.; Sun, L.; Li, J.; Cao, D., Adsorption and diffusion of shale gas reservoirs in modeled clay minerals at different geological depths. *Energy & Fuels* **2014**, *28* (12), 7467-7473.

25. Kang, S. M.; Fathi, E.; Ambrose, R. J.; Akkutlu, I. Y., Signal, R. F., Carbon dioxide storage capacity of organic-rich shales. *SPE Journal* **2011**, *16*, 842-855.

26. Fathi, E.; Akkutlu, I. Y., Lattice Boltzmann method for simulation of shale gas transport in Kerogen. *SPE Journal* **2012**, *18*, 27-37.

27. Sheng, M.; Li, G.; Huang, Z.; Tian, S.; Shah, S.; Geng, L., Pore-scale modeling and analysis of surface diffusion effects on shale-gas flow in kerogen pores. *Journal of Natural Gas Science and Engineering* **2015**, *27*, 979-985.

28. Chai, D.; Fan, Z.; Li, X., A unified convection-diffusion layered model for non-ideal rarefied gas flow in nanoscale porous media. ECMOR XVI-16th European Conference on the Mathematics of Oil Recovery **2018**.

29. Wang, H.; Wang, X.; Jin, X.; Cao, D., Molecular dynamics simulation of diffusion of shale oils in Montmorillonite, *The Journal of Physical Chemistry C* **2016**, *120* (16), 8986-8991.

30. Akkutlu, I. Y.; Fathi, E., Multiscale gas transport in shales with local kerogen heterogeneities. *SPE Journal* **2012**, *17* (4), 1002-1011.

31. Willhite, G. P.; Byrnes. A.; Dubois, M. K.; Pancake, R. E.; Tsau, J.; Daniels, J. R.; Flanders, W. A., A pilot carbon dioxide test, Hall-Gurney field, Kansas. *SPE Reservoir Evaluation & Engineering* **2012**, *15* (5), 520-532.

32. Jin, L.; Sorensen, J.; Hawthorne, S. B.; Smith, S. A.; Pekot, L. J.; Bosshart, N. W.; Burton-Kelly, M. E.; Miller, D. J.; Grabanski, C. B.; Gorecki, C. D.; Steadman, E. N.; Harju, J. A., Improving oil recovery by use of carbon dioxide in the Bakken unconventional System: a laboratory investigation. *SPE Reservoir Evaluation & Engineering* **2016**, *20* (3), 602-612.

33. Hawthorne, S. B.; Jin, L.; Kurz, B. A.; Miller, D. J.; Grabanski, C. B.; Sorensen, J. A.; Pekot, L. J.; Bosshart, N. W.; Smith, S. A.; Burton-Kelly, M. E.; Heebink, L. V.; Gorecki, C. D.; Steadman, E. N.; Harju, J. A., Integrating petrographic and petrophysical analyses with CO_2 permeation and oil extraction and recovery in the Bakken tight oil formation. SPE Unconventional Resources Conference **2017**, 15-16 February. SPE-185081-MS.

34. Jia, B.; Tsau, J.; Barati, R., Role of molecular diffusion in heterogeneous shale reservoirs during CO_2 huff-n-puff. SPE Europec featured at 79th EAGE Annual Conference & Exhibition **2017**, 12-15 June. SPE-185797-MS.

35. Clarkson, C. R.; Haghshenas, B., Modeling of supercritical fluid adsorption on organic-Rich shales and coal. Unconventional Resources Conference **2013**, 10-12 April. SPE-164532-MS.

36. Aljamaan, H. Petrophyical investigation on gas transport properties of the Barnett shale. SPE Annual Technical Conference and Exhibition **2013**, 30 September-2 October, SPE-167264-STU.

37. IEA., 20 Years of carbon capture and storage-accelerating future deployment. **2016**. http://www.iea.org/publications/freepublications/publication/20-years-of-carbon-capture-and-storage.html. (accessed April 2017)

38. Auset, M.; Keller, A., Pore-scale visualization of colloid straining and filtration in saturated porous media using micromodels. *Water Resources Research* **2006** *42* (12), W12S02.

39. Jin, L.; Wojtanowicz, A. K. Progression of injectivity damage with oily waste water in linear flow. *Petroleum Science* **2014**, *11* (4), 550-562.

40. Wang, S.; Feng, Q., Javadpour, F.; Xia, T.; Li, Z., Oil adsorption in shale nanopores and its effect on recoverable oil-in-place. *International Journal of Coal Geology* **2015**, 147–148, 9-24.

41. Jones, S. C., A technique for faster pulse-decay permeability measurements in tight rocks. *SPE Formation Evaluation* **1997** *12* (1), 19-26.

42. Ghanizadeh, A.; Gasparik, M.; Amann-Hildenbrand, M.; Gensterblum, Y.; Krooss, B. M., Experimental study of fluid transport processes in the matrix system of the European organic-rich shales: I. Scandinavian Alum Shale. *Marine and Petroleum Geology* **2014**, *51*, 79-99.

43. Ghanizadeh, A.; Bhowmik, S.; Haeri-Ardakani, O.; Sanei, H.; Clarkson, C. R., A comparison of shale permeability coefficients derived using multiple non-steady-state measurement techniques: examples from the Duvernay formation, Alberta (Canada). *Fuel* **2015**, *140*, 371-387.

44. Ghanizadeh, A.; Amann-Hildenbrand, A.; Gasparik, M.; Gensterblum, Y.; Krooss, B. M.; Littke, R., Experimental study of fluid transport processes in the matrix system of the European organic-rich shales: II. Posidonia shale (Lower Toarcian, Northern Germany). *International Journal of Coal Geology* **2014**, *123*, 20-33.

45 Gas Research Institute (GRI)., Development of laboratory and petrophysical techniques for evaluating shale reservoirs. Final report, prepared by ResTech Houston, Inc. Houston, Texas. **1996**.

46. Jia, B.; Tsau, J.; Barati, R., Evaluation of core heterogeneity effect on pulse-decay experiment. International Symposium of the Society of Core Analysis **2017**, 27-30 August.

47. Singh, H.; Javadpour, F., Langmuir slip-Langmuir sorption permeability model of shale. *Fuel* **2015**, *164*, 28-37.

48. Pang, Y.; Solidman, M. Y.; Denng, H.; Xie, X., Experimental and analytical investigation of adsorption effects on shale gas transport in organic nanopores. *Fuel* **2017**, *199*, 272-288.

49. Landry, C. J.; Prodanović, M. Eichhubl, P., Direct Simulation of supercritical gas flow in complex nanoporous media and prediction of apparent permeability. *International Journal of Coal Geology* **2016**, *15*9, 120-134.

50. Wang, J.; Kang, Q.; Chen, L.; Rahman, S. S., Pore-scale lattice Boltzmann simulation of micro-gaseous flow considering surface diffusion effect. *International Journal of Coal Geology* **2017**, *169*, 62-73.

51. Sun, H.; Yao, J.; Cao, Y.; Fan, D.; Zhang, L., Characterization of gas transport behaviors in shale gas and tight gas reservoirs by digital rock analysis. *International Journal of Heat and Mass Transfer* **2017**, *104*, 227-239.

52. Alnoaimi, K. R.; Duchateau, C.; Kovscek, A. R., Characterization and measurement of multiscale gas transport in shale-core samples. *SPE Journal* **2016**, *21* (2), 573-588.

53. Hu, H., Methane adsorption comparison of different thermal maturity kerogens in shale gas system. *Chinese Journal of Geochemistry* **2014**, *33* (4), 425-430.

54. Cannavò, F., 2012. Sensitivity analysis for volcanic source modeling quality assessment and model selection. *Computer & Geosciences* **2012**, *44*, 52-59.

55. Lemmon, E. W.; Huber, M. L.; McLinden, M. O., NIST Standard Reference Database 23: reference fluid thermodynamic and transport properties-REFPROP, Version 9.0, National Institute of Standards and Technology, Standard Reference Data Program, Gaithersburg **2010**.

56. Humayun, R.; Tomasko, D. L., High-resolution adsorption isotherms of supercritical carbon dioxide on activated carbon. *Thermodynamics* **2000**, 4**6** (10), 2065-2075.

57. Sudibandriyo, M.; Pan, Z.; Fitzgerald, J. E.; Robinson, R. L.; Gasem, K. A. M., Adsorption of methane, nitrogen, carbon dioxide, and their binary mixtures on dry activated carbon at 318.2 K and pressures up to 13.6 MPa. *Langmuir* **2003**, *19*(13), 5323–5331.

58. Gasem, K. A. M.; Robinson, R. L.; Fitzgerald, J. E.; Mohammad, S. A.; Chen, J. S.; Arumugam, A., Improved adsorption models for coalbed methane production and CO_2 sequestration. Final Technical Report for Advanced Resources International, Houston, Texas. **2007**.

59. Ravikovitch, P. I.; Neimark, A. V., Density functional theory model of adsorption on amorphous and microporous silica materials. *Langmuir* **2006**, 22, 11171–11179.

60. Wei, M.; Zhang, L.; Xiong, Y.; Li, J.; Peng, P., Nanopore structure characterization for organic-rich shale using the non-local-density functional theory by a combination of N_2 and CO_2 adsorption. *Microporous and Mesoporous Materials* **2016**, 227, 88-94.

61. Zhu, Y.; Su, H.; Jing, Y.; Guo, J.; Tang, J., Methane adsorption on the surface of a model of shale: a density functional theory study. *Applied Surface Science* **2016**, 387, 379-384.

62. Pini, R., Assessing the adsorption properties of mudrocks for CO_2 sequestration. *Energy Procedia* **2014**, 63, 5556-5561.

63. Arri, L. E.; Yee, D.; Morgan, W. D.; Jeansonne, M. W., Modeling coaled methane production with binary gas sorption. SPE Rocky Mountain Regional Meeting **1992**, 18-21 May, SPE 24363.

64. Fitzgerald, J. E.; Pan, Z.; Sudibandriyo, M.; Robinson, R. L.; Gasem, K. A. M.; Reeves, S., Adsorption of methane, nitrogen, carbon dioxide and their mixtures on wet Tiffany coal. *Fuel* **2005**, 84, 2351-2363.

65. Busch, A.; Alles, S.; Gensterblum, Y;, Prinz, D.; Dewhurst, D. N.; Raven, M. D.; Stanjek, H.; Krooss, B. M., Carbon dioxide storage potential of shales. *International Journal of Greenhouse Gas Control* **2008**, 2, 297-308.

66. Jeon, P. R.; Choi, J.; Yun, T. S.; Lee, C. H., Sorption equilibrium and kinetics of CO_2 on clay minerals from subcritical to supercritical conditions: CO_2 sequestration at nanoscale interfaces. *Chemical Engineering Journal* **2014**, 255, 705-15.

67. Weniger, P.; Kalkreuth, W.; Busch, A.; Krooss, B. M., High-pressure methane and carbon dioxide sorption on coal and shale samples from the Paraná Basin, Brazil. *International Journal of Coal Geology* **2010**, 84, 190-205.

68. Tang, X.; Ripepi, N., High pressure supercritical carbon dioxide adsorption in coal: adsorption model and thermodynamic characteristics. *Journal of CO_2 Utilization* **2017**, 18, 189-197.

69. Zhou, C.; Hall. F.; Gasem, K. A. M.; Robinson, R. L. J., Predicting gas adsorption using two-dimensional equations of state. *Industrial & Engineering Chemistry Research* **1994**, *33* (5): 1280-1289.

70. Sudibandriyo, M.; Mohammad, M. A.; Robinson, R. L.; Gasem, K. A. M., Ono–kondo lattice model for high-pressure adsorption: pure gases. *Fluid Phase Equilibria* **2010** *299* (2), 238-251.

71. Clarkson, C. R.; Bustin, R. M.; Levey, J. H., Application of the mono/multilayer and adsorption potential theories to coal methane adsorption isotherms at elevated temperature and pressure. *Carbon* **1997**, *35*(12), 1689-1705.

72. Ozdemir, E., Chemistry of the adsorption of carbon dioxide by Argonne Permian coals and a model to simulate CO_2 sequestration in coal seams. Ph.D. dissertation **2004**, University of Pittsburgh.

73. Yu, W.; Sepehrnoori, K.; Patzek, T. W., Modeling gas adsorption in Marcellus shale with Langmuir and BET isotherms. *SPE Journal* **2016,** *20* (2), 589-600.

74. Dubinin, M. M., Chemistry and physics of carbon, Vol 2. Marcell Dekker, New York **1996**.

75. Patzek, T. W.; Male, F.; Marder, M., Gas production in the Barnett shale obeys a simple scaling theory. *PNAS* **2013**, *110* (49), 19731-19736.

76. Abou-Kassem, J. H.; Mattar, L.; Dranchuk, P. M., Computer calculations of compressibility of natural gas. *Journal of Canadian Petroleum Technology* **1990**, *48* (8), 16-21.

77. Sutton, R. P., Fundamental PVT calculations for associated and gas/condensate natural-gas systems. *SPE Reservoir Evaluation & Engineering* **2009**, *10* (3), 270-284.

78. Jia, B.; Li, D.; Tsau, J.; Barati, R., Gas permeability evolution during production in the Marcellus and Eagle Ford shales: coupling diffusion/slip-flow, geomechanics, and adsorption/desorption. Unconventional Resources Technology Conference **2017**, 24-26 July, URTEC-2695702-MS.

79. Do, D. D., Adsorption analysis: equilibrium and kinetics. Imperial College Press, London. **1998**.

80. Wu, K.; Li, X.; Wang, C.; Yu, W.; Chen, Z., Model for surface diffusion of adsorbed gas in nanopores of shale gas reservoirs. *Industrial & Engineering Chemistry Research* **2015**, *54* (12), 3225-3236.

81. EIA, Annual energy outlook 2017 with projections to 2050. **2017**.

82. Gale, J. F. W.; Holder, J., Natural fractures in some US shales and their importance for gas production. London, Petroleum Geology Conference series **2011**, 7, 1131-1140.

83. Cai, J.; Wei, W.; Hu, X.; Liu, R.; Wang, J., Fractal characterization of dynamic fracture network extension in porous media. *Fractals* **2017**, *25* (2), 1750023.

84. Jin, H., Source rock potential of the Bakken shales in the Williston basin, North Dakota and Montana. Ph.D. dissertation, Colorado School of Mines. **2014**.

85. Chen, C., Multiscale imaging, modeling, and principal component analysis of gas transport in shale reservoirs. *Fuel* **2016**, *182*, 761-770.

86. Sun, Q.; Zhang, N.; Fadlelmula, M.; Wang, Y., Structural regeneration of fracture-vug network in naturally fractured vuggy reservoirs. *Journal of Petroleum Science and Engineering* **2018**, *165*, 28-41.

87. Civan, F.; Rai, C. S.; Sondergeld, C. H., Determining shale permeability to gas by simultaneous analysis of various pressure tests. *SPE Journal* **2012**, *17* (3), 717-726.

88. Jia, B.; Tsau, J.; Barati, R., Different flow behaviors of low-pressure and high-pressure carbon dioxide in shales. *SPE Journal* **2018**, *23* (4), 1452-1468.

89. Javadpour, F.; Fisher, D.; Unsworth, M., Nanoscale gas flow in shale gas sediments. *Journal of Canadian Petroleum Technology* **2007**, *46* (10), 55-61.

90. Fathi, E.; Tinni, A.; Akkutlu, I.Y., Correction to Klinkenberg slip theory for gas flow in nano-capillaries. *International Journal of Coal Geology* **2012**, *103*, 51-59.

91. Ning, Y.; Jiang, Y.; Liu, H.; Qin, G., Numerical modeling of slippage and adsorption effects on gas transport in shale formations using the lattice Boltzmann method. *Journal of Natural Gas Science and Engineering* **2015**, *26*, 345-355.

92. Ning, X., The measurement of matrix and fracture properties in naturally fractured low permeability cores using a pressure pulse method. Ph.D. dissertation, Texas A&M University. **1992**.

93. Kamath, J.; Boyer, R. E.; Nakagawa, F. M. Characterization of core scale heterogeneities using laboratory pressure transients. *SPE Formation Evaluation* **1992**, *7* (3), 219-227.

94. Cronin, M. B., Core-scale heterogeneity and dual-permeability pore structure in the Barnett shale. Master thesis, University of Texas at Austin. **2014**.

95. Bhandari, A. R.; Flemings, P. B.; Polito, P. J.; Cronin, M. B.; Bryant, S. L., Anisotropy and stress dependence of permeability in the Barnett shale. *Transport in Porous Media* **2015**, *108*, 393-411.

96. Meldi, M.; Lucor, D.; Sagaut, P.; Quantification of the effects of uncertainties in turbulent flows through generalized Polynomial Chaos. *Journal of Physics: Conference Series* **2011**, *318*, 042055.

97. Ye, Z.; Ghassemi, A., Deformation properties of saw-cut fractures in Barnett, Mancos and Pierre shales. 50th US Rock Mechanics/Geomechanics Symposium **2016**, 26-29 June. ARMA-2016-420.

98. Jones, F. O., A Laboratory study of the effects of confining pressure on fracture flow and storage capacity in carbonate rocks. *Journal of Petroleum Technology* **1975**, *27* (1), 21-27.

99. Gangi, A. F., Variation of whole and fractured porous rock permeability with confining pressure. *International Journal of Rock Mechanics and Mining Sciences* **1978**, *15* (5), 249-257.

100. Alnoaimi, K. R., Influence of cracks and microcracks on flow and storage capacities of gas shales at core-level. Ph.D. dissertation, Stanford University. **2016**.

101. Huo, D.; Gong, B., Discrete modeling and simulation on potential leakage through fractures in CO_2 sequestration. SPE Annual Technical Conference and Exhibition **2010**, 19-22 September. SPE-135507-MS.

102. Liang, B.; Jiang, H.; Li, J.; Gong, C.; Jiang, R.; Pei, Y.; Wei, S., Flow in multi-scale discrete fracture networks with stress sensitivity. *Journal of Natural Gas Science and Engineering* **2016**, *35*, 851-859.

103. Garmeh, G.; Jonhs, R. T., Upscaling of miscible floods in heterogeneous reservoirs considering reservoir mixing. *SPE Reservoir Evaluation & Engineering* **2010**, *13* (5), 747-763.

104. Chen, C., Effect of reservoir heterogeneity on primary recovery and CO_2 huff 'n' puff recovery in shale-oil reservoirs. *SPE Reservoir Evaluation & Engineering* **2014**, 17 (3), 404-413.

105. Kurtzman, D.; Jennings J. W.; Lucia, F. J., Dissolution vugs in fractured carbonates: A complication? or perhaps a key for simplifying reservoir characterization. *Geophysical Research Letters* **2007**, *34*, L20409.

106. İncı, U., Lignite and carbonate deposition in Middle Lignite succession of the Soma Formation, Soma coalfield, western Turkey. *International Journal of Coal Geology* **1998**, *37*, 287-313.

107. Duerr, A. D., Types of secondary porosity of carbonate rocks in injection and test wells in Southern Peninsular Florida. U.S. Geological Survey, Water-Resources Investigations Report 94-4013. **1995**.

108. Wu, Y., Multiphase Fluid flow in porous and fractured reservoirs. Gulf Professional Publishing. **2015**.

109. CMOST., CMOST user guide enhance & accelerate sensitivity analysis, history matching, optimization & uncertainty analysis. **2016**.

110. Civan, F., Can gas-permeability of fractured-shale be determined accurately by testing of core plugs, drill cuttings, and crushed samples? SPE/AAPG/SEG Unconventional Resources Technology Conference **2017**, 24-26 July. URTEC-2666389-MS.

111. IMEX., 2016. IMEX user guide, three-phase, black-oil reservoir simulator.

112. Lemmon, E. W.; Huber, M. L.; McLinden, M. O., NIST reference fluid thermodynamic and transport properties—REFPROP. NIST standard reference database. **2002**.

113. Crain, P. E., Crain's petrophysical handbook by E. R. (Ross) Crain, online at www.spec2000.net. 2018.

114. Li, J.; Yu, T.; Liang, X.; Zhang, P.; Chen, C.; Zhang, J., Insights on the gas permeability change in porous shale. *Advances in Geo-Energy Research* **2017**, *1* (2), 69-73.

115. Jia, B.; Tsau, J.; Barati, R., Role of molecular diffusion in heterogeneous, naturally fractured shale reservoirs during CO_2 huff-n-puff. *Journal of Petroleum Science and Engineering* **2018**, *164*, 31-42.

116. IEA., Annual energy outlook 2016 with projections to 2040 International Energy Agency, http://www.eia.gov/outlooks/aeo/pdf/0383(2016).pdf (accessed January 2016).

117. Cipolla, C. L.; Lolon, E. P.; Erdle, J. C.; Rubin, B., Reservoir modeling in shale-gas reservoirs. *SPE Reservoir Evaluation & Engineering* **2010**, *13* (4), 638-653.

118. Clarkson, C. R.; Nobakht, M.; Kaviani, D.; Ertekin, T., Production analysis of tight-gas and shale-Gas reservoirs using the dynamic-slippage concept. *SPE Journal* **2010**,17, 230-242.

119. Forchheimer, P., Wasserbewegung durch Boden, Z. Ver. Deutsch. Ing **1901**, *45*, 1782-1788.

120. Barree, R. D.; Conway, M., Beyond beta factors: a complete model for Darcy Forchheimer and trans-Forchheimer flow in porous media. SPE Annual Technical Conference and Exhibition **2004**, 26-29 September. SPE-89325-MS.

121. Barree, R. D.; Conway, M., Multiphase non-Darcy flow in proppant packs. *SPE Production & Operations* **2009**, *24* (2), 257-268.

122. Lee, R.; Logan, R. W.; Tek, M. R., Effect of turbulence on transient flow of real gas through porous media. *SPE Reservoir Evaluation & Engineering* **1987**, *2* (1), 108-120.

123. Civan, F.; Rai, C. S.; Sondergeld, C. H., Intrinsic shale permeability determined by pressure-pulse measurements using a multiple-mechanism apparent-gas-permeability non-Darcy model. SPE Annual Technical Conference and Exhibition **2010**, 19-22 September. SPE-135087-MS.

124. Jia, B.; Tsau, J.; Barati, R., Different flow behaviors of low-pressure and high-pressure CO_2 in Shales. Unconventional Resources Technology Conference **2017**, 24-26 July. URTEC-2690239-MS.

125. Heller, R.; Vermylen, J.; Zoback, M., Experimental investigation of matrix permeability of gas shales. *AAPG Bulletin* **2014**, *98* (5), 975-995.

126. "Mean Free Path, Molecular Collisions". Hyperphysics.phy-astr.gsu.edu. http://hyperphysics.phy-astr.gsu.edu/hbase/Kinetic/menfre.html. <Accessed 12/05/2018>

127. Wang, F. P.; Reed, R. M., Pore networks and fluid flow in gas shales. SPE Annual Technical Conference and Exhibition **2009**, 4-7 October. SPE-124253-MS.

128. Heller, R.; Zoback, M., Adsorption of methane and carbon dioxide on gas shale and pure mineral samples. *Journal of Unconventional Oil and Gas Resources* **2014**, *8*, 14-24.

129. Arthur, W. A.; Gast, A. P., Physical Chemistry of Surfaces, Wiley. **1997**.

130. Lu, X.; Li, F.; Watson, A. T., Adsorption studies of natural gas storage in Devonian shales. *SPE Formation Evaluation* **1995**, *10*, 109-113.

131. Terzaghi, K.; Peck, R. B., Soil mechanics in engineering practice. New York: John Wiley & Sons. **1948**.

132. Medved, I.; Černý, R., Surface diffusion in porous media: A critical review. *Microporous Mesoporous Materials* **2011**, *142*, 405-422.

133. Economides, M.; Nolte, K., Reservoir Stimulation. Wiley. **2010**.

134. Barati, R.; Liang, J., A review of fracturing fluid systems used for hydraulic Fracturing of oil and gas wells. *Journal of Applied Polymer Science* **2014**, *131* (16).

135. Liu, H.; Rutqvist, J.; Berryman, J. G., On the relationship between stress and elastic strain for porous and fractured rock. *International Journal of Rock Mechanics and Mining Sciences* **2009**, *46* (2), 289-296.

136. Wasaki, A.; Akkutlu, I. Y., Permeability of organic-rich shale. *SPE Journal* **2015**, *20* (6), 1384-1396.

137. Ertekin, T.; King, G. A.; Schwerer, F. C., Dynamic gas slippage: a unique dual-mechanism approach to the flow of gas in tight formations. *SPE Formation Evaluation* **1986**, *1* (1), 43-52.

138. Clarkson, C. R.; Nobakht, M.; Kaviani, D.; Ertekin, T., Production analysis of tight-gas and shale-gas reservoirs using the dynamic-slippage concept. *SPE Journal* **2012**, *17* (1), 230-242.

139. Huang, X.; Bandilla, K. W.; Celia, M. A., Multi-physics pore-network modeling of two-phase shale matrix flows. *Transport in Porous Media* **2015**, *111* (1), 123-141.

140. Minkoff, S. E.; Stone, C. M.; Bryant, S.; Peszynska, M.; Wheeler, M. F., Coupled fluid flow and geomechanical deformation modeling. *Journal of Petroleum Science and Engineering* **2003**, *38* (1), 37-56.

141. Suarez-Rivera, R.; Burghardt, J.; Edelman, E.; Stanchits, S.; Surdi, A., Geomechanics considerations for hydraulic fracture conductivity. US Rock Mechanics /Geomechanics Symposium **2013**, 23-26 June. ARMA-2013-666.

142. Frash, L. P.; Carey, J. W., Experimental measurement of fracture permeability at reservoir conditions in Utica and Marcellus shale. SPE/AAPG/SEG Unconventional Resources Technology Conference 2017, 24-26 July. URTEC-2666764-MS.

143. Mcginley, M. J., The Effects of Fracture Orientation and Anisotropy on Hydraulic Fracture 49 Conductivity in the Marcellus Shale. Master Thesis, Texas A&M University. **2015**.

144. Dilmore, R., Exploring the behavior of shales as seals and storage reservoirs for CO_2. National Energy Technology Laboratory Carbon Storage R&D Project Review Meeting Developing the Technologies and Infrastructure for CCS **2014**, 12-14 Aug.

145. Raghavan, R.; Chin, L. Y., Productivity changes in reservoirs with stress-dependent permeability. SPE AnnualTechnical Conference and Exhibition **2002**, 29 September-2 October. SPE-77535-MS.

146. Dong, J.; Hsu, J.; Wu, W.; Shimamoto, T.; Hung, J.; Yeh, E.; Wu, Y.; Sone, H., Stress-dependence of the permeability and porosity of sandstone and shale from TCDP Hole-A. *International Journal of Rock Mechanics and Mining Sciences* **2010**, *47* (7), 1141-1157.

147. Chen, D.; Pan, Z.; Ye, Z., Dependence of gas shale fracture permeability on effective stress and reservoir pressure: model match and insights. *Fuel* **2015**, *139*, 383-392.

148. Reyes, L.; Osisanya, S. O., Empirical correlation of effective stress dependent shale rock properties. Petroleum Society's Canadian International Petroleum Conference **2000**, 4-8 June. PETSOC-2000-038.

149. Fink, R.; Krosses, B. M.; Amann, A., Stress-dependence of porosity and permeability of the Upper 25 Jurassic Bossier shale: An experimental study. Geological Society London Special Publications 454. **2017**.

150. Yildirim, L., Evaluation of petrophysical properties of gas shale and their change due to interaction with water. Master Thesis, Penn State University. **2014**.

Appendix A. Calculations of isothermal gas compressibility and gas viscosity in chapter 2

The calculation of isothermal gas compressibility is based on the work Abou-Kassem et al.[76]

$$c_r = c_g p_c = \frac{1}{\rho_r}\left(\frac{\partial \rho_r}{\partial p_r}\right)_{T_r}$$

where p_c is gas critical pressure; c_r, ρ_r, p_r and T_r are reduced compressibility, reduced density, reduced pressure and reduced temperature, respectively, dimensionless.

The following procedures are given below to step-by-step calculate gas compressibility.

- Determine gas critical temperature and pressure T_c and p_c.
- Calculate gas reduced temperature and pressure T_r and p_r by

$$p_r = \frac{p}{p_c} \qquad T_r = \frac{T}{T_c}$$

- Determine ρ_r by

$$\rho_r = 0.27\frac{p_r}{ZT_r}$$

- Determine Z factor with

$$Z = 1 + B_1\rho_r + B_2\rho_r^2 + B_3\rho_r^5 + B_4(1 + B_5\rho_r^2)\rho_r^2 \times \exp(-B_5\rho_r^2)$$

where $B_1 = A_1 + (A_2 / T_r) + (A_3 / T_r^3) + (A_4 / T_r^4) + (A_5 / T_r^5)$

$$B_2 = A_6 + (A_7 / T_r) + (A_8 / T_r^2)$$

$$B_3 = -A_9\left[(A_7 / T_r) + (A_8 / T_r^2)\right]$$

$$B_4 = A_{10} / T_r^3$$

$$B_5 = A_{11}$$

$$A_1 = 0.3265 \quad A_2 = -1.0700 \quad A_3 = -0.5339 \quad A_4 = 0.01569 \quad A_5 = -0.05165 \quad A_6 = 0.5475 \quad A_7 = -0.7361$$

$$A_8 = 0.1844 \quad A_9 = 0.1056 \quad A_{10} = 0.6134 \quad A_{11} = 0.7210$$

Alternatively, *Z* factor can be obtained directly from the REFPROP program.

- Calculate $\partial p_r/\partial \rho_r$ by

$$\left(\frac{\partial \rho_r}{\partial p_r}\right)_{T_r} = \frac{T_r}{0.27} \times \left[1 + 2B_1\rho_r + 3B_2\rho_r^2 + 6B_3\rho_r^5 + (B_4\rho_r^2)(3 + 3B_5\rho_r^2 - 2B_5^2\rho_r^4) \times \exp(-B_5\rho_r^2)\right]$$

- Calculate reduced compressibility c_r from ρ_r and $(\partial p_r/\partial \rho_r)/T_r$ by

$$c_r = \left[\rho_r \left(\frac{\partial p_r}{\partial \rho_r}\right)_{T_r}\right]^{-1}$$

- Calculate gas compressibility by

$$c_g = c_r / p_c$$

The following procedures are given to step-by-step calculate gas viscosity. They are based on the work of Sutton.[67]

- Determine X and Y by

$$X = 3.47 + \frac{1,588}{T} + 0.0009M_g \qquad Y = 1.66378 - 0.04679X$$

where *T* is temperature, in the unit of °R; and M_g is the molecular weight.

- Determine ξ by

$$\xi = \frac{0.9490T_c^{1/6}}{M_g^{1/2} p_c^{2/3}}$$

- Determine μ_{gsc} by

$$\mu_{gsc} = 10^{-4} \times \left[0.8077T_r^{0.618} - 0.357 \times \exp(-0.449T_r) + 0.340 \times \exp(-4.058T_r) + 0.018\right] / \xi$$

Determine μg in the unit of cP by

$$\mu_g = \mu_{gsc} \times \exp(X \rho_g^Y)$$

Appendix B. Result table and pressure curves in chapter 3

Table B1 Parameters in all the simulation scenarios and effective permeability ratios over the base case.

Scenario	ϕ	***a***	***b***	***f(a,b)***	**|*s*|, 1/second**	ϕ**/*f(a,b)***	**Ratio: transient vs. steady-state**
1. Base case	6.00%	6.15E-01	6.76E-01	1.16	0.04	0.05	1.00 vs. 1.00
2. Hetero_V	6.00%	6.15E-01	6.76E-01	1.16	0.03	0.05	0.67 vs. 0.69
3. Hetero_V_Reverse	6.00%	6.15E-01	6.76E-01	1.16	0.03	0.05	0.73 vs. 0.69
4. Hetero_H	6.00%	6.15E-01	6.76E-01	1.16	0.04	0.05	1.03 vs. 1.02
5. Hetero_H_Reverse	6.00%	6.15E-01	6.76E-01	1.16	0.04	0.05	1.03 vs. 1.02
6. Hetero_ V_{dp} _0.39	6.00%	6.15E-01	6.76E-01	1.16	0.02	0.05	0.60 vs. 0.58
7. Hetero_V_{dp}_0.53	6.00%	6.15E-01	6.76E-01	1.16	0.01	0.05	0.35 vs. 0.28
8. Hetero_ V_{dp} _0.69	6.00%	6.15E-01	6.76E-01	1.16	0.01	0.05	0.18 vs. 0.11
9. Hetero_ V_{dp} _0.39_corr	6.00%	6.15E-01	6.76E-01	1.16	0.04	0.05	0.95 vs. 0.97
10. Frac_2nd half	6.01%	6.15E-01	6.77E-01	1.16	0.06	0.05	1.41 vs. 1.73
11. Frac_1st half	6.01%	6.15E-01	6.77E-01	1.16	0.06	0.05	1.48 vs. 0.05
12. Frac_D_f_0.001 cm	6.00%	6.15E-01	6.76E-01	1.16	-	0.05	- vs. 1.02
13. Frac_ D_f _0.01 cm	6.00%	6.15E-01	6.76E-01	1.16	-	0.05	- vs. 1.02
14. Frac_ D_f _0.1 cm	6.01%	6.16E-01	6.78E-01	1.16	-	0.05	- vs. 1.02
15. Frac_L_0.5 cm_15˚	6.60%	6.76E-01	7.44E-01	1.27	0.05	0.05	1.32 vs. 1.44
16. Frac_L_0.5 cm_30˚	6.60%	6.76E-01	7.44E-01	1.27	0.05	0.05	1.32 vs. 1.42
17. Frac_L_0.5 cm_45˚	6.60%	6.76E-01	7.44E-01	1.27	0.05	0.05	1.22 vs. 1.31
18. Frac_L_0.5 cm_60˚	6.60%	6.76E-01	7.44E-01	1.27	0.04	0.05	1.11 vs. 1.19
19. Frac_L_0.5 cm_75˚	6.60%	6.76E-01	7.44E-01	1.27	0.04	0.05	1.01 vs. 1.08
20. Frac_L_0.7 cm_45˚	6.90%	7.07E-01	7.78E-01	1.32	0.06	0.05	1.44 vs. 1.56
21. Frac_L_0.9 cm_45˚	7.06%	7.23E-01	7.95E-01	1.34	0.07	0.05	1.94 vs. 1.96
22. Frac_L_1.1 cm_45˚	7.36%	7.54E-01	8.29E-01	1.39	0.11	0.05	2.89 vs. 3.16
23. Frac_L_1.3 cm_45˚	7.43%	7.61E-01	8.37E-01	1.41	0.16	0.05	4.07 vs. 5.02
24. Vug_D_0.1 cm_3	6.09%	6.24E-01	6.86E-01	1.18	0.04	0.05	1.00 vs. 1.02
25. Vug_D_0.1 cm_8	6.24%	6.39E-01	7.03E-01	1.20	0.04	0.05	1.01 vs. 1.02
26. Vug_D_0.1 cm_15	6.44%	6.60E-01	7.26E-01	1.24	0.04	0.05	1.02 vs. 1.03
27. Vug_D_0.1 cm_24	6.71%	6.87E-01	7.56E-01	1.28	0.04	0.05	1.02 vs. 1.03
28. Vug_D_0.1 cm_35	7.04%	7.21E-01	7.93E-01	1.34	0.04	0.05	1.01 vs. 1.02
29. Frac_L_0.5 cm_45˚ w/ Vug_D_0.1 cm_3	6.65%	6.81E-01	7.49E-01	1.27	0.05	0.05	1.20 vs. 1.30
30. Frac_L_0.7 cm_45˚ w/ Vug_D_0.1 cm_8	7.02%	7.19E-01	7.91E-01	1.34	0.06	0.05	1.49 vs. 1.54
31. Frac_L_0.9 cm_45˚ w/ Vug_D_0.1 cm_15	7.28%	7.45E-01	8.20E-01	1.38	0.07	0.05	1.83 vs. 1.94
32. Frac_L_1.1 cm_45˚ w/ Vug_D_0.1 cm_24	7.89%	8.08E-01	8.89E-01	1.48	0.14	0.05	3.67 vs. 4.27
33. Frac_L_1.3 cm_45˚ w/ Vug_D_0.1 cm_35	7.99%	8.19E-01	9.01E-01	1.50	0.16	0.05	4.11 vs. 5.16
34. Frac_L_1.3 cm_45˚ w/ Vug _D_0.1 cm_35_ran	7.99%	8.19E-01	9.01E-01	1.50	0.16	0.05	3.98 vs. 5.04

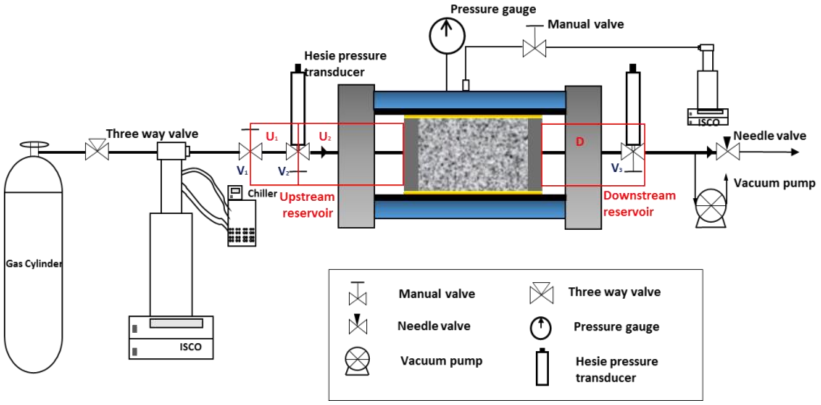

Figure A1 Schematic of the pulse-decay set-up.[78]

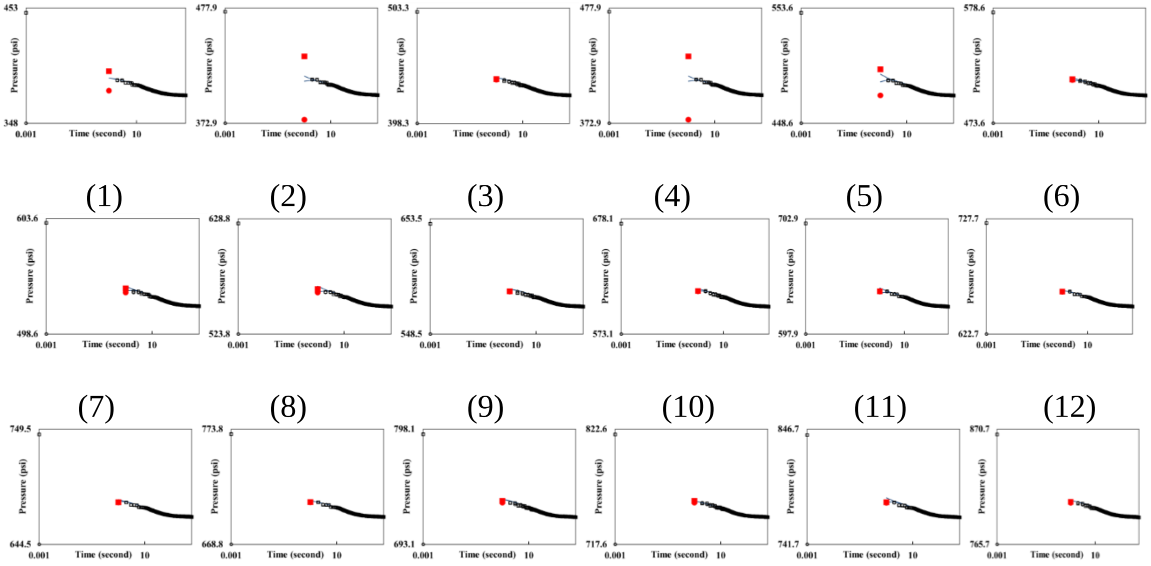

(1) (2) (3) (4) (5) (6)

(7) (8) (9) (10) (11) (12)

(13) (14) (9) (10) (11) (12)

Figure B2 Full pressure profiles (black dots highlighted with red for the second data point) along with history matching results (blue lines) for all the pressure transmission tests under the effective stress of 1,000 psi. The first data point is shifted to 0.001 second to be able to appear at the logarithmic axis. Each plot represents an individual experiment.

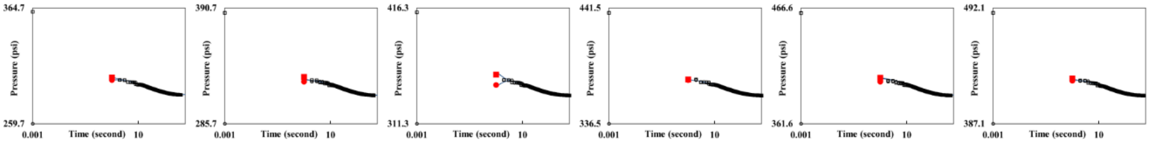

(1) (2) (3) (4) (5) (6)

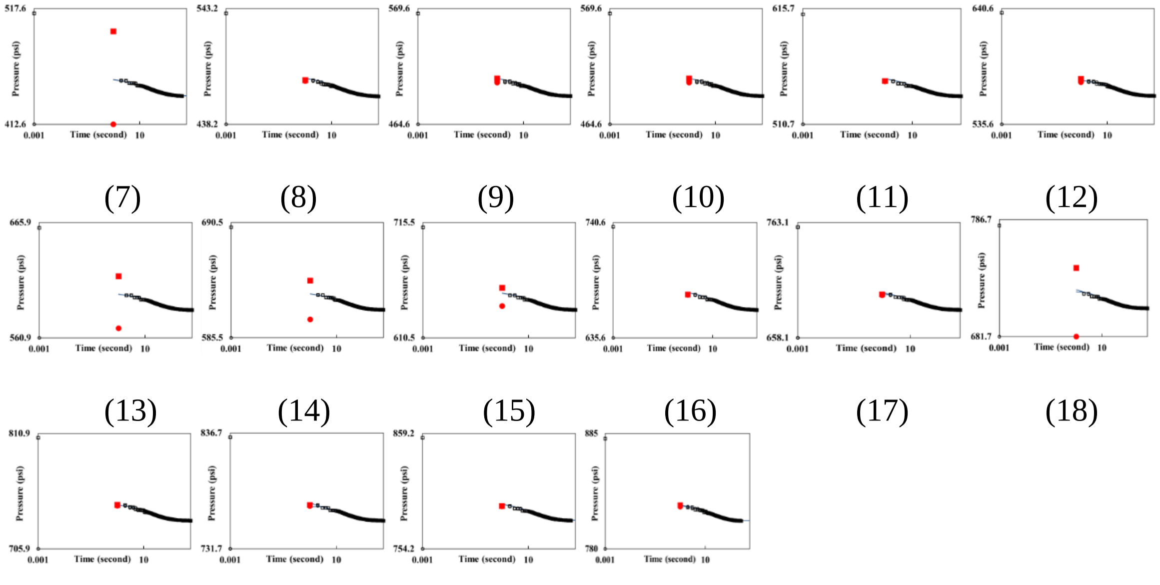

(7) (8) (9) (10) (11) (12)

(13) (14) (15) (16) (17) (18)

(19) (20) (21) (22)

Figure B3 Full pressure profiles (black dots highlighted with red for the second data point) along with history matching results (blue lines) for all the pressure transmission tests under the effective stress of 2,000 psi. The first data point is shifted to 0.001 second to be able to appear at the logarithmic axis. Each plot represents an individual experiment.

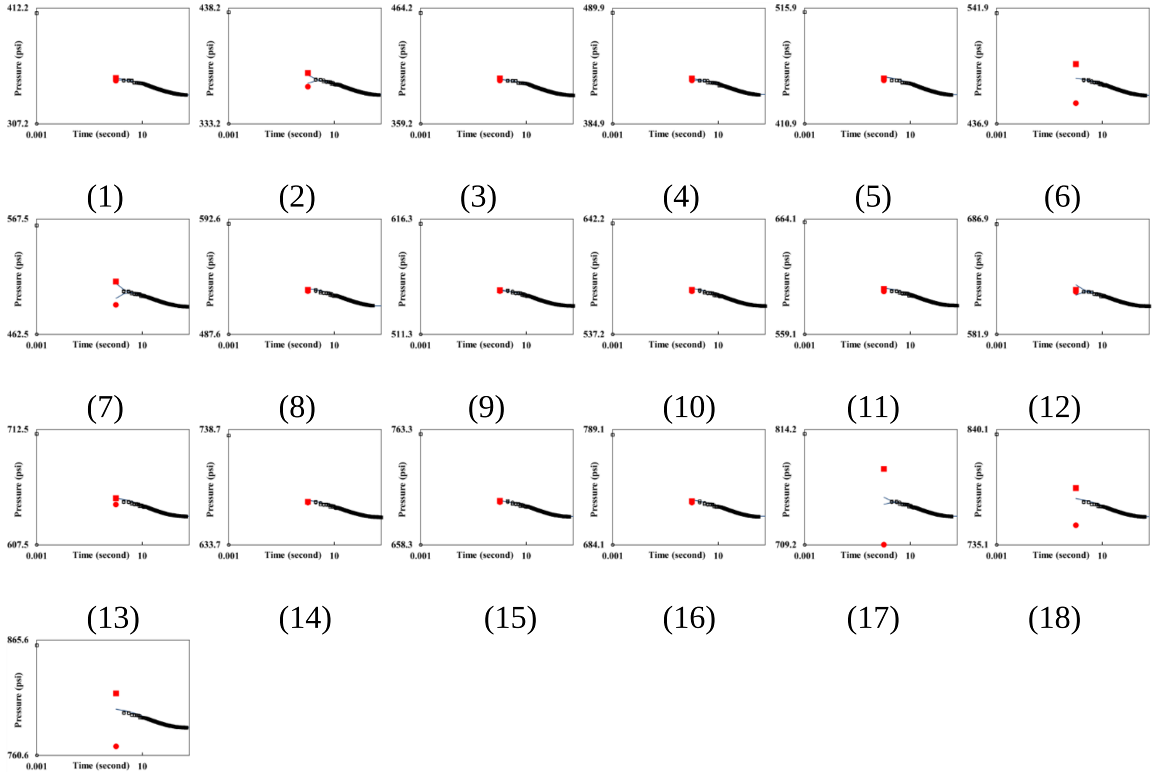

(1) (2) (3) (4) (5) (6)

(7) (8) (9) (10) (11) (12)

(13) (14) (15) (16) (17) (18)

(19)

Figure B4 Full pressure profiles (black dots highlighted with red for the second data point) along with history matching results (blue lines) for all the pressure transmission tests under the effective stress of 3,000 psi. The first data point is shifted to 0.001 second to be able to appear at the logarithmic axis. Each plot represents an individual experiment.

Appendix C. Calculation details of permeability evolution in chapter 4

The appendix provides calculation details at all the discrete pressure points. Table C1 shows the data from step 1 to step 3 in the main text and Table C2 shows the data in step 4 with different values of surface diffusivity.

Table C1 Calculation details of considering geomechanical effect, slip flow/pore diffusion and adsorption layer.

p, psi	p_s, psi	r, nm	r_{ad}, nm	θ	k_∞, nD	k_a, nD	$k_{\infty eff}$, nD	$f(Kn)_{eff}$	k_{aeff}, nD	k_{atot}, nD
4,000	1000	45.33	44.57	0.84	64.66	65.99	62.84	1.02	64.16	69.44
3,880	1120	44.37	43.61	0.84	61.95	63.29	60.18	1.02	61.50	66.94
3,760	1240	43.41	42.65	0.84	59.30	60.64	57.58	1.02	58.90	64.53
3,640	1360	42.45	41.69	0.83	56.70	58.05	55.03	1.02	56.35	62.18
3,520	1480	41.49	40.73	0.83	54.17	55.52	52.54	1.03	53.87	59.92
3,400	1600	40.53	39.77	0.82	51.69	53.05	50.11	1.03	51.45	57.73
3,280	1720	39.57	38.81	0.82	49.27	50.64	47.74	1.03	49.09	55.63
3,160	1840	38.61	37.85	0.81	46.91	48.29	45.43	1.03	46.78	53.62
3,040	1960	37.65	36.89	0.80	44.61	46.00	43.17	1.03	44.54	51.70
2,920	2080	36.69	35.93	0.80	42.36	43.77	40.97	1.03	42.36	49.87
2,800	2200	35.73	34.97	0.79	40.17	41.60	38.83	1.04	40.24	48.15
2,680	2320	34.77	34.01	0.78	38.04	39.49	36.75	1.04	38.17	46.54
2,560	2440	33.81	33.05	0.78	35.97	37.44	34.73	1.04	36.17	45.06
2,440	2560	32.85	32.09	0.77	33.96	35.46	32.76	1.04	34.24	43.70
2,320	2680	31.89	31.13	0.76	32.00	33.53	30.86	1.05	32.36	42.49
2,200	2800	30.93	30.17	0.75	30.10	31.67	29.01	1.05	30.55	41.44
2080	2920	29.97	29.21	0.74	28.26	29.87	27.22	1.06	28.80	40.58
1,960	3040	29.01	28.25	0.73	26.48	28.14	25.48	1.06	27.11	39.94
1,840	3160	28.05	27.29	0.71	24.76	26.47	23.81	1.07	25.49	39.55
1,720	3280	27.09	26.33	0.70	23.09	24.87	22.20	1.08	23.94	39.46
1600	3400	26.13	25.37	0.68	21.48	23.34	20.64	1.09	22.46	39.73
1480	3520	25.17	24.41	0.67	19.94	21.88	19.14	1.10	21.04	40.46
1360	3640	24.21	23.45	0.65	18.44	20.49	17.70	1.11	19.70	41.77
1240	3760	23.25	22.49	0.63	17.01	19.18	16.32	1.13	18.44	43.82
1120	3880	22.29	21.53	0.60	15.63	17.95	15.00	1.15	17.27	46.88
1000	4000	21.33	20.57	0.57	14.32	16.82	13.74	1.18	16.19	51.33
880	4120	20.37	19.61	0.54	13.06	15.80	12.53	1.21	15.22	57.79
760	4240	19.41	18.65	0.51	11.86	14.90	11.39	1.26	14.38	67.28
640	4360	18.45	17.69	0.46	10.71	14.18	10.31	1.33	13.71	81.65
520	4480	17.49	16.73	0.41	9.63	13.82	9.28	1.45	13.43	104.66
400	4600	16.53	15.77	0.35	8.60	14.32	8.32	1.68	13.98	144.70
280	4720	15.57	14.81	0.27	7.63	16.06	7.43	2.12	15.76	224.14

160	4840	14.61	13.85	0.18	6.72	21.71	6.59	3.26	21.46	434.52
40	4960	13.65	12.89	0.05	5.86	68.02	5.83	11.64	67.83	1975.09

Table C2 Calculation details of considering surface diffusion as the last step.

p, psi	μ_g, Pa·s	ρ_g, kg/m^3	$k_{\infty\ eff}$, nD	$f(Kn)_{eff}$	D_{s-d} = 1E-8 m^2/s		D_{s-d} = 1E-7 m^2/s		D_{s-d} = 1E-6 m^2/s		D_{s-d} = 1E-5 m^2/s	
					$f(Kn)_{tot}$	k_{atot}, nD	$f(Kn)_{tot}$	k_{atot}, nD	$f(Kn)_{tot}$	k_{atot}, nD	$f(Kn)_{tot}$	k_{atot}, nD
4,000	2.16E-5	174.41	62.84	1.02	1.02	64.21	1.03	64.69	1.10	69.44	1.86	116.94
3,880	2.12E-5	170.38	60.18	1.02	1.02	61.55	1.03	62.04	1.11	66.94	1.93	115.97
3,760	2.09E-5	166.23	57.58	1.02	1.02	58.95	1.03	59.46	1.12	64.53	2.00	115.20
3,640	2.05E-5	161.95	55.03	1.02	1.03	56.41	1.03	56.94	1.13	62.18	2.08	114.65
3,520	2.01E-5	157.55	52.54	1.03	1.03	53.93	1.04	54.48	1.14	59.92	2.18	114.34
3,400	1.97E-5	153.02	50.11	1.03	1.03	51.51	1.04	52.08	1.15	57.73	2.28	114.30
3,280	1.94E-5	148.37	47.74	1.03	1.03	49.15	1.04	49.74	1.17	55.63	2.40	114.56
3,160	1.90E-5	143.58	45.43	1.03	1.03	46.85	1.04	47.47	1.18	53.62	2.54	115.15
3,040	1.86E-5	138.67	43.17	1.03	1.03	44.61	1.05	45.26	1.20	51.70	2.69	116.13
2,920	1.82E-5	133.64	40.97	1.03	1.04	42.43	1.05	43.11	1.22	49.87	2.87	117.53
2,800	1.78E-5	128.49	38.83	1.04	1.04	40.31	1.06	41.03	1.24	48.15	3.08	119.41
2,680	1.75E-5	123.23	36.75	1.04	1.04	38.26	1.06	39.01	1.27	46.54	3.32	121.87
2,560	1.71E-5	117.86	34.73	1.04	1.04	36.26	1.07	37.06	1.30	45.06	3.60	124.98
2,440	1.68E-5	112.40	32.76	1.04	1.05	34.33	1.07	35.18	1.33	43.70	3.93	128.86
2,320	1.64E-5	106.85	30.86	1.05	1.05	32.46	1.08	33.37	1.38	42.49	4.33	133.64
2,200	1.61E-5	101.23	29.01	1.05	1.06	30.66	1.09	31.64	1.43	41.44	4.81	139.50
2,080	1.57E-5	95.54	27.22	1.06	1.06	28.92	1.10	29.98	1.49	40.58	5.39	146.65
1,960	1.54E-5	89.80	25.48	1.06	1.07	27.24	1.11	28.40	1.57	39.94	6.10	155.39
1,840	1.51E-5	84.03	23.81	1.07	1.08	25.63	1.13	26.90	1.66	39.55	6.97	166.05
1,720	1.48E-5	78.24	22.20	1.08	1.09	24.10	1.15	25.49	1.78	39.46	8.07	179.12
1,600	1.45E-5	72.44	20.64	1.09	1.10	22.63	1.17	24.18	1.93	39.73	9.46	195.23
1,480	1.42E-5	66.65	19.14	1.10	1.11	21.24	1.20	22.99	2.11	40.46	11.24	215.23
1,360	1.40E-5	60.88	17.70	1.11	1.13	19.93	1.24	21.91	2.36	41.77	13.58	240.33
1,240	1.37E-5	55.15	16.32	1.13	1.15	18.70	1.29	20.98	2.68	43.82	16.68	272.20
1,120	1.35E-5	49.46	15.00	1.15	1.17	17.57	1.35	20.23	3.13	46.88	20.89	313.36
1,000	1.33E-5	43.82	13.74	1.18	1.20	16.54	1.43	19.70	3.74	51.33	26.76	367.59
880	1.31E-5	38.26	12.53	1.21	1.25	15.64	1.55	19.47	4.61	57.79	35.18	440.91
760	1.29E-5	32.76	11.39	1.26	1.31	14.91	1.73	19.67	5.91	67.28	47.71	543.39
640	1.27E-5	27.35	10.31	1.33	1.40	14.39	1.99	20.51	7.92	81.65	67.25	693.10
520	1.26E-5	22.02	9.28	1.45	1.55	14.34	2.43	22.55	11.27	104.66	99.71	925.69
400	1.24E-5	16.78	8.32	1.68	1.84	15.29	3.25	27.05	17.39	144.70	158.74	1321.19
280	1.23E-5	11.63	7.43	2.12	2.40	17.85	4.93	36.60	30.18	224.14	282.74	2099.54
160	1.21E-5	6.58	6.59	3.26	3.88	25.59	9.52	62.77	65.90	434.52	629.74	4152.00
40	1.20E-5	1.63	5.83	11.64	14.91	86.90	44.35	258.56	338.80	1975.09	3283.30	19140.48

Appendix D. Experimental results of stress-dependent matrix and fractures permeability and fitting results in chapter 5

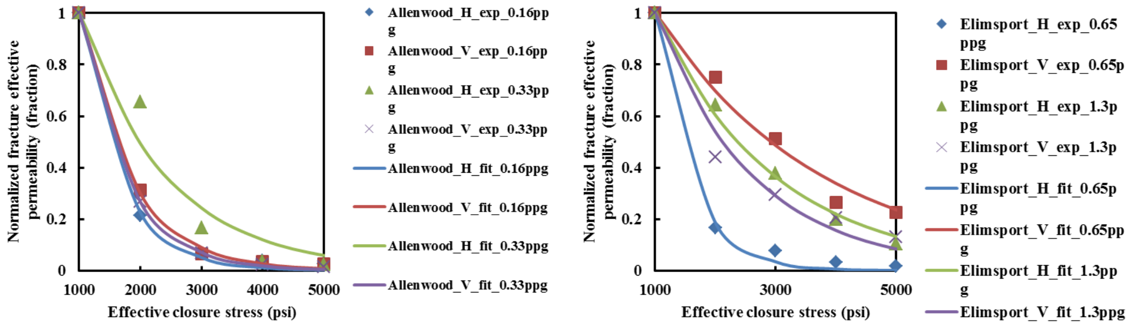

(a) (b)

Figure D1 Experimental and fitted propped fracture permeability as a function of effective stress in (a) Allenwood and (b) Elimsport of the Marcellus shale, experiment data from Mcginley (2015).[143]

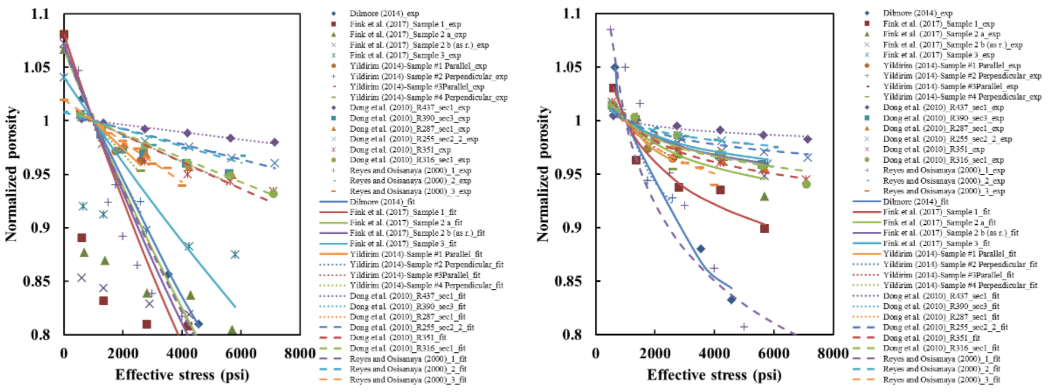

(a) (b)

Figure D2 Experimental and fitted shale matrix porosity as a function of effective stress with (a) exponential- and (b) power- law relationships.

Table D1 Fitting results of unpropped and propped fracture of the Marcellus shale, *b* is the fitting parameter in Eq. (5-1).[142, 143]

	Source	*b*
Unpropped_shear offset	Marcellus	1.03E-3
Allenwood_H_0.16ppg	Marcellus	1.49E-3
Allenwood_V_0.16ppg	Marcellus	1.20E-3
Allenwood_H_0.33ppg	Marcellus	7.06E-4
Allenwood_V_0.33ppg	Marcellus	1.32E-3
Elimsport_H _0.65ppg	Marcellus	1.68E-3
Elimsport_V _0.65ppg	Marcellus	3.60E-4
Elimsport_H _1.3ppg	Marcellus	5.04E-4
Elimsport_V _1.3ppg	Marcellus	6.18E-4

Table D2 Fitting results of matrix porosity using the power-law relationship, q is the fitting parameter in Eq. (5-4).[144, 146,150, 150]

	Source	q
Dilmore	Marcellus	1.12E-01
Fink et al. _Sample 1	Upper Jurassic Bossier	5.88E-02
Fink et al._Sample 2 a	Upper Jurassic Bossier	3.23E-02
Fink et al._Sample 2 b (as r.)	Upper Jurassic Bossier	2.35E-02
Fink et al._Sample 3	Upper Jurassic Bossier	2.12E-02
Yildirim -Sample #1 Parallel	Green River	4.07E-02
Yildirim -Sample #2 Perpendicular	Green River	8.57E-02
Yildirim -Sample #3 Parallel	Green River	4.07E-02
Yildirim -Sample #4 Perpendicular	Green River	4.76E-02
Dong et al._R437_sec1	TCDP Hole-A	7.68E-03
Dong et al._R390_sec3	TCDP Hole-A	2.39E-02
Dong et al._R287_sec1	TCDP Hole-A	2.43E-02
Dong et al._R255_sec2_2	TCDP Hole-A	1.63E-02
Dong et al._R351_sec2	TCDP Hole-A	2.86E-02
Dong et al._R316_sec1	TCDP Hole-A	2.47E-02
Reyes and Osisanaya_1	Wanpanuka	1.17E-01
Reyes and Osisanaya_2	Wilcox	1.35E-02
Reyes and Osisanaya_3	Atoka	3.67E-02